



TECHNISCHE  
UNIVERSITÄT  
WIEN

DISSERTATION

# Generalized application and time-reversal of the lasing principle

ausgeführt zum Zwecke der Erlangung des akademischen Grades

**Doktor der technischen Wissenschaften**

unter der Leitung von

Univ.Prof. Dipl.-Ing. Dr.techn. Stefan Rotter  
Institut für Theoretische Physik, E136

eingereicht an der  
Technischen Universität Wien  
Fakultät für Physik

von

**Dipl.-Ing. Kevin Pichler**



Wien, 11. Jänner 2023

Ort, Datum

Unterschrift



# Erklärung zur Verfassung der Arbeit

Dipl.-Ing. Kevin Pichler  
Hainburger Straße 66/22, 1030 Wien

Hiermit erkläre ich, dass ich diese Arbeit selbständig verfasst habe, dass ich die verwendeten Quellen und Hilfsmittel vollständig angegeben habe und dass ich die Stellen der Arbeit – einschließlich Tabellen, Karten und Abbildungen –, die anderen Werken oder dem Internet im Wortlaut oder dem Sinn nach entnommen sind, auf jeden Fall unter Angabe der Quelle als Entlehnung kenntlich gemacht habe.

Wien, 11. Jänner 2023

---

Ort, Datum

---

Unterschrift



# Contents

<b>Kurzfassung</b>	<b>v</b>
<b>Abstract</b>	<b>vii</b>
<b>1 Introduction</b>	<b>1</b>
<b>2 Lasers</b>	<b>5</b>
2.1 Laser basics . . . . .	5
2.2 Generalization of the lasing principle . . . . .	8
2.3 Phonon lasers . . . . .	9
2.3.1 Experimental realization . . . . .	10
2.3.2 Theoretical description . . . . .	12
<b>3 Phonon lasing near an exceptional point</b>	<b>17</b>
3.1 Exceptional points . . . . .	17
3.2 Laser linewidth . . . . .	19
3.3 Experimental and theoretical results . . . . .	20
3.3.1 Phonon laser threshold . . . . .	21
3.3.2 Phonon laser linewidth . . . . .	24
<b>4 Coherent perfect absorption</b>	<b>29</b>
4.1 Time-reversed lasing . . . . .	29
4.2 Random anti-lasing . . . . .	34
4.2.1 Experimental realization . . . . .	34
4.2.2 Experimental and numerical results . . . . .	38
<b>5 Coherent virtual absorption</b>	<b>53</b>
5.1 Basic realization . . . . .	54
5.2 Disordered media . . . . .	56
<b>6 Customized coherent perfect absorption</b>	<b>61</b>
6.1 Perfect absorption of specific states . . . . .	61
6.2 Degenerate cavity anti-laser . . . . .	64
6.3 Scattering suppression from imperfect absorbers . . . . .	68
6.4 Perfect absorption of electromagnetic pulses . . . . .	70
<b>7 Conclusion and Outlook</b>	<b>73</b>

<b>Appendix</b>	<b>75</b>
A Phonon laser analysis . . . . .	75
A.1 Quantum Langevin equations . . . . .	75
A.2 Derivation of the phonon laser threshold . . . . .	77
A.3 Linear stability analysis . . . . .	80
B Simulation of electromagnetic waves . . . . .	83
B.1 Wave equation . . . . .	83
B.2 Helmholtz equation . . . . .	85
B.3 Time-averaged Poynting vector . . . . .	87
<b>Acknowledgments</b>	<b>89</b>
<b>List of Figures and Tables</b>	<b>91</b>
<b>Bibliography</b>	<b>93</b>
<b>Curriculum vitae</b>	<b>105</b>

# Kurzfassung

Die Erfindung des Lasers hatte einen enormen Einfluss auf unsere Gesellschaft – kaum eine andere Technologie erstreckt sich auf so viele verschiedene Anwendungsbereiche. Die besonderen Eigenschaften des Laserlichts, welches sich durch hohe Intensität und Kohärenz auszeichnet, führten zu einem erheblichen technologischen Fortschritt. Wie sich herausgestellt hat, ist das zugrundeliegende Prinzip des Laserprozesses – die stimulierte Emission – jedoch nicht auf Licht und elektromagnetische Strahlung beschränkt, sondern kann in ähnlicher Art und Weise auch auf andere Signalformen, wie etwa mechanische Oszillationen, angewandt werden. Diese Erkenntnis lieferte die Grundlage für die Entwicklung von Phononenlasern, welche als das akustische Gegenstück zu optischen Lasern gesehen werden können. Mit Hilfe dieser neuartigen Laservorrichtungen eröffnen sich zahlreiche faszinierende Forschungsbereiche mit vielversprechenden Anwendungsmöglichkeiten.

Wie in dieser Arbeit gezeigt wird, verkörpern Phononenlaser eine geeignete Plattform, um den Einfluss eines sogenannten Ausnahmepunkts (engl. „exceptional point“, EP) auf die Eigenschaften eines Lasers zu untersuchen. EPs sind eine spezielle Art von nicht-hermitescher Entartung, bei der mehrere Eigenwerte und auch die dazugehörigen Eigenvektoren miteinander verschmelzen, wodurch wiederum andere interessante Effekte hervorgerufen werden können. Eine der ersten theoretischen Vorhersagen im Zusammenhang mit EPs war die extreme Verbreiterung der Laserlinienbreite auf Grund der nicht-Orthogonalität der Resonatormoden. Während dieser Effekt niemals direkt in einem optischen Laser beobachtet werden konnte, hat sich die Situation mit der Verfügbarkeit von Phononenlasern entsprechend geändert. Durch die Untersuchung des Verhaltens eines Phononenlasers in der Umgebung eines EPs, sowohl theoretisch als auch experimentell, konnte in der vorliegenden Arbeit diese EP-induzierte Linienverbreiterung erstmals explizit sichtbar gemacht werden.

Weiters beschäftigt sich diese Dissertation mit der Zeitumkehr des Laserprinzips. Vor einigen Jahren wurde gezeigt, dass ein bestimmtes monochromatisches Signal perfekt von einem Objekt absorbiert werden kann, wenn sowohl die exakte Signalform als auch die Absorptionsstärke genau aufeinander abgestimmt werden. Dieser Vorgang, der als „kohärente perfekte Absorption“ bezeichnet wird, kann als die zeitumgekehrte Version des Laserprozesses an der Laserschwelle verstanden werden, weshalb man in diesem Zusammenhang auch von einem Anti-Laser spricht. Während sich frühe Ausführungen von kohärenten perfekten Absorbern auf relativ einfache Systeme mit einem gewissen Grad an geometrischer Symmetrie beschränkt haben, konnte im Rahmen dieser Dissertation gezeigt werden, wie dieses Konzept auch auf ungeordnete Medien und komplexe Streusysteme verallgemeinert werden kann. Basierend auf dieser technischen Verbesserung wird hier die erste experimentelle Umsetzung eines Zufalls-Anti-Lasers vorgestellt.

In diesem Zusammenhang wird auch das Phänomen der „kohärenten virtuellen Absorption“ diskutiert, bei dem die Energie eines geeignet geformten einlaufenden Signals vorübergehend in einem verlustlosen System gespeichert wird und bei Bedarf wieder freigesetzt werden kann, wenn das einlaufende Signal geändert wird. Dieser Effekt kann unter anderem dafür genutzt werden, das gestreute Signal von einem unvollkommen absorbierenden System temporär zu unterdrücken, um die Resonanz eines idealen Anti-Lasers zu imitieren. Darüber hinaus werden Methoden zur weiteren Verbesserung der technischen Anwendbarkeit von Anti-Lasern vorgestellt. Einerseits wird gezeigt, wie ein System konstruiert werden kann, um ein vordefiniertes Signal mit beliebig gewählter Frequenz perfekt zu absorbieren, indem die innere Struktur des Systems optimiert wird. Andererseits wird die kohärente perfekte Absorption von Signalen mit beliebiger Wellenfront in einer entarteten Kavität besprochen. Letzteres wird dabei auch mit aktuellen experimentellen Ergebnissen verglichen, welche unsere theoretischen Vorhersagen bestätigen. Zuletzt wird noch ein Schema für die perfekte Absorption von elektromagnetischen Pulsen, also von äußerst breitbandigen Signalen, vorgeschlagen.



# Abstract

The invention of the laser had a tremendous impact on our society—hardly any other technology can be found in so many different fields of applications. The special properties of laser light, which is characterized by high intensity and coherence, enabled formidable technological advances. As it turned out, the underlying principle of the lasing process—stimulated emission—is not limited to light and electromagnetic radiation but can be similarly applied to other signal forms like, for example, mechanical oscillations. That insight provided the basis for the development of phonon lasers, which can be considered as the sonic equivalent to optical lasers. This novel type of laser device opens up many areas of fascinating new physics with promising applications.

As we show in this thesis, phonon lasers represent a suitable platform to study the influence of a so-called “exceptional point” (EP) on the lasing characteristics. EPs are a special type of non-Hermitian degeneracy at which some of the eigenvalues and also their corresponding eigenvectors coalesce, which can in turn induce several other interesting effects. An early theoretical prediction associated with EPs was the extreme broadening of the laser linewidth caused by the non-orthogonality of the resonator modes. While this effect could never be directly observed in an optical laser, the situation changed with the availability of phonon lasers. Our work demonstrates the first observation of this EP-induced linewidth broadening by investigating the behavior of a phonon laser in the vicinity of an EP, both theoretically and experimentally.

Furthermore, this thesis deals with the time-reversal of the lasing principle. Recently, it was shown that a specific monochromatic signal can be perfectly absorbed by an object if both the exact waveform and the absorption strength are precisely tuned. This process, which is called “coherent perfect absorption”, can be considered as the time-reverse of lasing at threshold and is therefore also referred to as anti-lasing. While early implementations of coherent perfect absorbers were limited to relatively simple systems with a certain degree of geometric symmetry, we demonstrate in the framework of this dissertation how the concept can be extended to the general case of disordered media and complex scattering systems. Based on this technical improvement, we present the first experimental realization of a random anti-laser.

In this context, we also discuss the phenomenon of “coherent virtual absorption”, where the energy of a suitably shaped incident signal is transiently stored inside a lossless structure and can be released on demand if the incoming waveform is changed. We further make use of this effect to suppress the scattered signal from an imperfectly absorbing system temporarily in order to mimic the response of an ideal anti-laser. Moreover, several methods to improve the versatility of coherent perfect absorbers for technical applications are presented. On the one hand, we show how specific input states with predefined frequency can be perfectly absorbed if the system structure is

accordingly engineered. On the other hand, the coherent perfect absorption of signals with arbitrary wavefront is discussed in the framework of a degenerate cavity anti-laser. The latter is also compared to recent experimental results which verify our theoretical predictions. Finally, we propose a protocol for the perfect absorption of electromagnetic pulses, i.e., highly polychromatic signals.

# Chapter 1

## Introduction

The history of physics is strongly characterized by certain milestones which paved the way for a significant improvement of our understanding of nature or opened up major opportunities for important technological advancements. One of the most essential scientific achievements of the past century was the development of the laser [1, 2].

Based on the phenomenon of *stimulated emission* [3, 4], the coherent amplification of electromagnetic waves has been first demonstrated in the microwave regime at *Columbia University* in 1953 [5, 6]. Only a few years later, the concept was already extended to infrared and optical wavelengths [1]. During the following decades, however, a large range of frequencies in the electromagnetic spectrum was covered by applications of the lasing principle [7]. Simultaneously, a comprehensive laser theory was developed [8–10] and the better the characteristics of laser light have been understood, the more relevant the lasing process became in industry and technology. Nowadays, the laser forms an integral part of our daily life, which is proven by countless applications [7, 11, 12] ranging from surgical and industrial cutting tools via laser pointers through to transmitters for optical communication—and probably there are many more to be invented in the future. Moreover, lasers are used in several scientific disciplines as standard laboratory equipment, e.g., for high-precision measurements on the nanoscale level, as a coherent source of electromagnetic signals, or for high harmonic or ultra-short pulse generation.

Over the years, it turned out that the principle of stimulated emission can be generalized in the sense that it is not limited to electromagnetic waves (i.e., *photons*) but can be similarly applied to other signal types like, for instance, mechanical oscillations (i.e., *phonons*) [13–17]. This insight gave rise to the development of several “exotic laser” devices such as *phonon lasers* [18–28], *plasmon lasers* [29–33], or *polariton lasers* [34–40]. Even the coherent amplification of matter waves has been reported—a concept which is commonly referred to as *atom laser* [41–47]. With the advent of these novel laser variants, a whole new field of research opened up with many interesting new insights and promising applications [48–50].

Within the scope of laser physics, also the influence of so-called *exceptional points* (EPs) is of enormous physical interest [51–55]. Exceptional points are peculiar features in the parameter space of non-Hermitian matrices where they represent spectral singularities at which not only some of the eigenvalues but also the corresponding eigenvectors of the system coalesce. This special type of degeneracy gives rise to a number of intriguing and often also counter-intuitive features such as the reversal of the pump-dependence of a

laser [56,57], loss-induced suppression and revival of lasing [58], directional lasing [59], or asymmetric mode switching [60].

An early theoretical prediction associated with EPs in lasers was the broadening of the laser linewidth [61,62] beyond the fundamental *Schawlow-Townes limit* [1]. This broadening is induced by the non-orthogonality of resonator modes, which leads to excess quantum noise, and is quantified by the *Petermann factor* [63–65]. While such a linewidth enhancement could already be measured in several experiments [66–68], only subsequent theoretical work associated this behavior to the presence of a nearby EP [62]. A direct observation of the laser linewidth broadening directly at an EP remained out of reach because experimentally it is neither straightforward to steer a laser to an EP nor to measure its extremely narrow linewidth. However, this situation changed with the availability of phonon lasers, whose linewidth can be measured more easily than in their optical counterparts. In fact, we could show recently that the linewidth of a phonon laser is indeed significantly broadened when the system is operated near an EP [24].

While the laser as a source of coherent signals is vital for myriads of scientific and industrial applications, there is also a large number of technologies which rely on the absorption of such a signal—for example, any type of signal receiver like mobile phone antennas or signal detectors. In order to optimize the efficiency of such devices, it is desirable to maximize their absorption strength for specific signals. The ultimate limit for this improvement is clearly that of complete (i.e., 100%) absorption, which implies that the entire incident energy is perfectly focused on the device without any backscattering. This idealized situation corresponds to the excitation of a zero of the system’s scattering matrix [69], which means that the incident signal represents an eigenstate of the scattering matrix with vanishing eigenvalue. In 2010, physicists from *Yale University* have shown in a theoretical analysis [70] that this process, which is called *coherent perfect absorption*, can indeed be realized if the amount of dissipation inside the system as well as the properties of the incoming monochromatic signal are precisely tuned. Already one year later, in 2011, the first experimental realization of such a *coherent perfect absorber* (CPA) was reported [71]. Since this effect corresponds to the time-reversed process of lasing at threshold, a CPA is also referred to as *anti-laser* [72,73].

Due to their promising ability of optimizing absorption processes with potential applications in sensing, radar cloaking, or signal transmission, CPAs have attracted considerable scientific interest [74]. Consequently, a remarkable number of theoretical and experimental realizations has been published during the last years [70,71,75–92]. In addition, it was demonstrated how the effects of lasing and anti-lasing can be combined [93–95] within the framework of  $\mathcal{PT}$ -symmetric optical systems [96–99]. Moreover, several fascinating CPA-related results have been presented in the context of ultrathin metamaterials [84], exceptional points [100–102], or sub-wavelength focusing [103–105]. Further, it turned out that even for lossless objects the entire reflection and transmission can be transiently suppressed by temporal modulation of the incident signal [106]. As long as the proper input waveform is maintained, the outgoing components destructively interfere with each other and the impinging energy is temporarily stored inside the object. This phenomenon is called *coherent virtual absorption* and opens up interesting new

---

lines of research and applications [106–109].

While early implementations of coherent perfect absorption have been realized in rather simple geometrical structures, this thesis aims to demonstrate how the concept can also be applied in disordered media and complex scattering environments. Because of the time-reversal analogy to a *random laser* [110, 111], this kind of device is also referred to as *random anti-laser* [91]. In order to make CPAs suitable for actual “real-world” uses apart from ideal laboratory conditions, however, further improvements of the versatility of such devices as well as of their theoretical understanding will be required, although first advances towards customizable applications have already been made [112–115].

This thesis is structured as follows: in [chapter 2](#), an overview of the laser basics is given and the lasing principle is generalized to signal forms other than electromagnetic waves. This generalization is discussed in detail by taking the example of a phonon laser. [Chapter 3](#) shows how a phonon laser can be used to study the influence of an exceptional point on the lasing characteristics. In particular, the phonon laser threshold and linewidth are investigated in the vicinity of an EP. The numerical analysis based on the dynamical system equations is compared to recent experiments performed by our collaborators at the *Micro/Nano Photonics Lab* of *Washington University in St. Louis*.

The time-reversal of the lasing process is introduced in [chapter 4](#), which leads to the concept of coherent perfect absorption. After a brief review of early implementations in rather simple geometries, we show how this effect can be generalized to disordered media and present the first implementation of a random anti-laser, which was realized in close collaboration with the *Institut de Physique de Nice* at the *Université Côte d’Azur*. [Chapter 5](#) deals with coherent virtual absorption, where we first introduce the concept in a simple one-dimensional system and then generalize the principle to one- and two-dimensional disordered media by numerical optimization of the input signal. Within [chapter 6](#), we present several techniques to improve the usability of coherent perfect absorption for technical applications. On the one hand, we discuss the absorption of specific input signals with predefined frequency and wavefront by customized engineering of the system structure, and on the other hand, we treat the universal absorption of arbitrary wavefronts in a degenerate cavity setup. The latter case is also compared to experimental results from a collaboration with the *Advanced Imaging Lab* from the *Hebrew University of Jerusalem*. Furthermore, we propose the possibility of annihilating the outgoing waves from a detuned CPA by temporal modulation of the incoming signal amplitude, as well as a concept for the perfect absorption of electromagnetic pulses.

The thesis ends with a conclusion and outlook in [chapter 7](#), and additional information about technical details can be found in the [Appendix](#).



# Chapter 2

## Lasers

### 2.1 Laser basics

The acronym *LASER* was introduced by Gordon Gould [2] and stands for *light amplification by stimulated emission of radiation*. However, the fundamental principle of the laser was first demonstrated for microwaves [5, 6] and was thus referred to as *MASER*<sup>1</sup>. Although there exist several other “-ASER” acronyms—such as *RASER* for radio frequencies, *UVASER* for ultraviolet, or *XASER* for X-rays—the term *laser* has become a generic expression for all devices which are based on the laser principle.

As already comprised by the acronym, the essential process behind the laser is *stimulated emission*, which is one of the fundamental quantum processes in the interaction between electromagnetic fields and matter. Other important types of interaction in this scope are *spontaneous emission* or *absorption* of a photon. The occurrence of these phenomena is closely related to the quantized nature of the energy levels in atoms or molecules, which is illustrated schematically in fig. 2.1. For the sake of simplicity, we consider a two-level system in order to capture the essence of the aforementioned light-matter interactions. In the case that the system is originally prepared in the lower energy level  $E_1$  (*ground state*), an incident photon can be absorbed by the system if the photon energy  $\hbar\omega$  is approximately equal to the energy difference between the upper and the lower level, i.e.,  $\hbar\omega \approx \Delta E := E_2 - E_1$ . After this process, which is called *absorption*, the system ends up in the upper energy level  $E_2$  (*excited state*) as the photon energy is transformed into internal energy of the system. The excited state is generally unstable which causes the system to decay into the ground state at a characteristic rate. The excess energy is thereby spontaneously emitted into the environment in the form of a photon with frequency  $\omega = \Delta E/\hbar$  (*transition frequency*). Such a *spontaneous emission* produces a photon which travels in a random direction, with random phase and polarization. However, the decay of the excited state into the ground state can also be triggered by the interaction with an additional photon with the transition frequency  $\omega = \Delta E/\hbar$ . In this case, which is referred to as *stimulated emission*, the emitted photon is an exact copy of the incident photon that induced the emission, i.e., it features the same frequency, phase, polarization, and direction of travel. In a subsequent step, these two photons could interact with other equivalent two-level systems (prepared in the excited state) and so on and so forth, thus producing more and more identical photons.

<sup>1</sup> Microwave amplification by stimulated emission of radiation

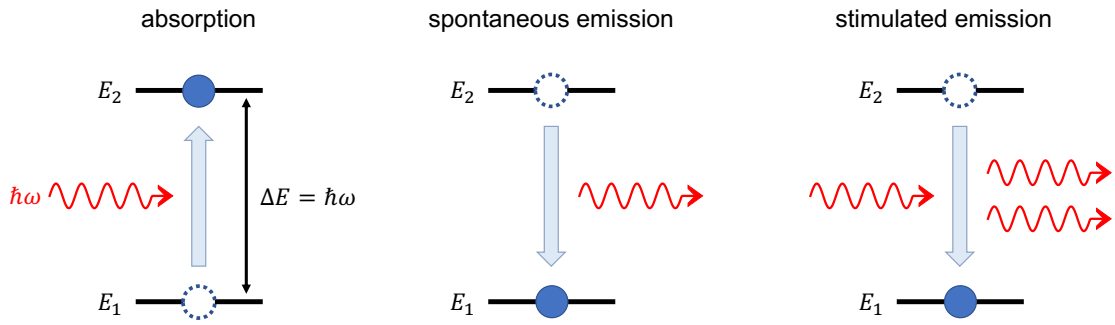


**Figure 2.1:** Schematic visualization of fundamental light-matter interactions: absorption, spontaneous emission, stimulated emission.

Therefore, the effect of stimulated emission can be exploited for a coherent amplification of an electromagnetic wave and hence provides the physical basis for a laser.

For building an actual laser in its simplest form, three major components are essential: an active medium (gain medium), an energy pump mechanism, and a resonator. The gain medium usually consists of an ensemble of atoms or molecules featuring different discrete energy levels, two of which are involved in the stimulated emission process. Since the effects of stimulated emission and absorption are competing with each other, it is necessary that the population of the upper energy level exceeds the population of the lower energy level in order to achieve a net amplification. Due to the fact that excited states are decaying over time, such a *population inversion* can be maintained only if a suitable pump mechanism is implemented, which continuously populates the upper energy level of the laser transition. The pump energy can be provided by, e.g., an arc or flash lamp, gas discharge, or another laser. In a two-level system, a population inversion cannot be achieved because at some point the rates of absorption and emission would become equal. Consequently, there must be at least three energy levels involved in the pumping scheme, as shown in [fig. 2.2a](#). In practice, many laser systems are based on a four-level pumping scheme with energies  $E_G < E_L < E_M < E_P$  (see [fig. 2.2b](#)). In such a system, electrons are pumped from the ground state  $E_G$  into the pump band  $E_P$ , which has a fast, radiationless decay into the metastable energy level  $E_M$ . The laser action (stimulated emission) takes place between the levels  $E_M$  and  $E_L$ , where the lower level  $E_L$  decays rapidly into the ground state  $E_G$ . Because of the relatively long lifetime of the upper energy level  $E_M$  and the fast depletion of the lower energy level  $E_L$ , a population inversion can be achieved more easily than in a three-level pumping scheme. The magnitude of the population inversion and hence the achievable laser amplification is determined by the power which is supplied by the pump mechanism. The minimum pump power at which the gain exceeds all losses due to absorption or energy leakage out of the system is called the *lasing threshold*. Pumping above the laser threshold results in exponential amplification of the laser light as it passes through the active medium, while the achievable laser intensity is limited, however, due to nonlinear saturation effects stemming from the depletion of the population inversion with increasing field strength.



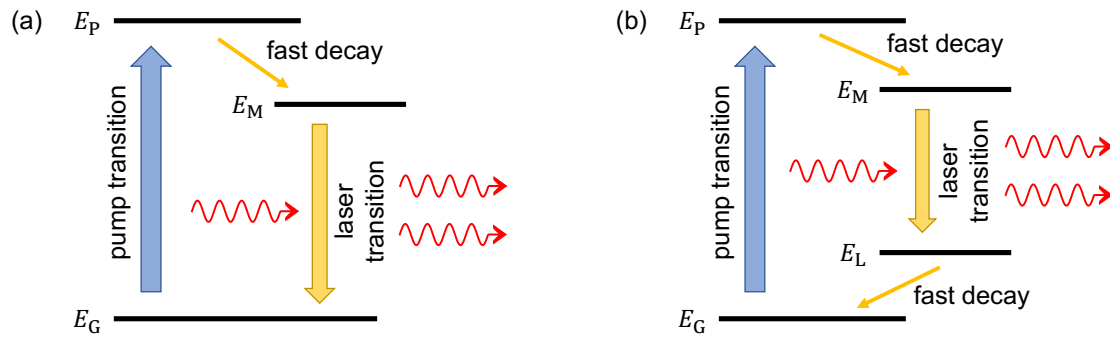


**Figure 2.2:** Typical laser pumping schemes. Three-level laser pumping (a): electrons are pumped from the ground state  $E_G$  into the pump band  $E_P$ , which decays rapidly into the metastable energy level  $E_M$ . If the pumping is strong enough, a population inversion between  $E_M$  and  $E_G$  can be achieved. Four-level laser pumping (b): as compared to the three-level pumping in (a), there is an additional energy level  $E_L$  between  $E_M$  and  $E_G$ , which now forms the lower energy level of the laser transition instead of  $E_G$ . Since the energy level  $E_L$  decays rapidly into the ground state  $E_G$ , a population inversion between  $E_M$  and  $E_L$  can be achieved more easily as the lower level  $E_L$  is almost empty at all times.

In order to maximize the amplification while keeping the system size reasonably small, the gain medium is usually embedded in a resonator, which provides feedback of the laser light. In the simplest case, such a resonator could be a *Fabry-Pérot*-like cavity as depicted in [fig. 2.3a](#). Within such a setup, the light is reflected back and forth between two mirrors, thus dramatically increasing the effective path length that it travels through the gain medium inside. If the mirrors are partially transparent (at least one of them), part of the light can be coupled out as a coherent laser beam, given that the system is pumped above threshold. However, the optical feedback can also be provided in a different way: if the gain medium is placed inside a disordered medium (see [fig. 2.3b](#)), multiple reflections can trap the light within the gain medium sufficiently long to reach the lasing threshold. Due to the chaotic character of the scattering inside the disordered medium, this type of device is called *random laser* [110, 111]. Laser light which is emitted from such a random laser typically features a highly complex spatial field pattern.

For pumping below threshold, the laser output is non-vanishing because of (amplified) spontaneous emission and increases slightly with increasing pump power. Above threshold, where the laser light is dominated by contributions from stimulated emission rather than from spontaneous emission, the slope of the power dependence is orders of magnitude greater than it is below. Furthermore, due to the characteristics of stimulated emission, the spectral width, i.e., the *laser linewidth*, is dramatically decreased above threshold. These properties make laser light—which is characterized by high intensity, narrow linewidth, and a high degree of coherence—an indispensable component of modern technology.

More detailed information on laser theory or technical realizations can be found in numerous relevant textbooks [7–10].

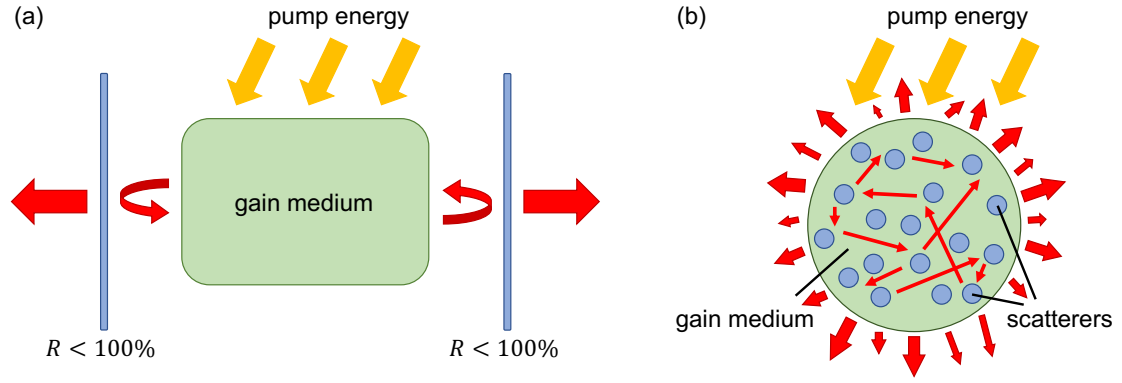


**Figure 2.3:** Different types of optical feedback in lasers. In its simplest form, a laser consists of a gain medium embedded in a resonator (a), where the optical feedback comes from multiple reflections between the two mirrors. Laser light can be coupled out of the system if the end mirrors are partially transparent ( $R < 1$ ). Alternatively, the optical feedback can be provided by chaotic scattering in a disordered medium (b), which results in a highly complex wavefront of the emitted laser signal. In any case, the gain medium must be supplied with energy by an external pump mechanism in order to maintain the population inversion.

## 2.2 Generalization of the lasing principle

As explained in [section 2.1](#), the underlying mechanism of the lasing principle is the effect of stimulated emission. However, this process is not limited to electromagnetic waves (i.e., *photons*) but can also occur in a similar manner for certain bosonic quasiparticles such as *phonons* or *plasmons*. This becomes clear if we consider the structure of a typical laser Hamiltonian [9],

$$\hat{H} = \hat{H}_F + \hat{H}_A + \hat{H}_{A-F} + \hat{H}_{B_1} + \hat{H}_{B_1-F} + \hat{H}_{B_2} + \hat{H}_{B_2-A}, \quad (2.1)$$

in which  $\hat{H}_F$  denotes the Hamilton operator of the laser field,  $\hat{H}_A$  corresponds to the active medium, and  $\hat{H}_{A-F}$  describes the interaction between the active medium and the field. The operators  $\hat{H}_{B_1}$  and  $\hat{H}_{B_2}$  stand for heat baths which are coupled to the field and to the active medium, respectively. The corresponding interaction terms are denoted by  $\hat{H}_{B_1-F}$  and  $\hat{H}_{B_2-A}$ .

Particularly, however, we are interested in the interaction term  $\hat{H}_{A-F}$ . We assume that the active medium consists of an ensemble of suitable atoms. Under certain approximations (e.g., *rotating wave approximation*) and assuming that only two atomic energy levels are involved in the laser transition, the interaction between a single atom and the field can be written as [9, 116]

$$\hat{H}_{a-F} = \hbar g (\hat{a}_2^\dagger \hat{a}_1 \hat{b} + \hat{b}^\dagger \hat{a}_1^\dagger \hat{a}_2), \quad (2.2)$$

where  $\hat{a}_1$  and  $\hat{a}_2$  ( $\hat{a}_1^\dagger$  and  $\hat{a}_2^\dagger$ ) denote the annihilation (creation) operators of an electron in the lower ( $E_1$ ) and upper ( $E_2$ ) atomic energy levels,  $\hat{b}$  ( $\hat{b}^\dagger$ ) describes the annihilation (creation) of a photon in the field mode, and  $g$  is a coupling constant. The structure of

eq. (2.2) reveals two possible atom-field interactions: the first term in the parentheses represents the absorption of a photon while an electron is excited from the lower energy level  $E_1$  into the upper energy level  $E_2$ , whereas the second term describes the emission of a photon while an electron drops from the upper energy level  $E_2$  into the lower energy level  $E_1$ . Since the active medium consists of a large number of atoms, which are distinguished by the index  $\mu$ , the total interaction term  $\hat{H}_{A-F}$  is given by the sum over all individual contributions  $\hat{H}_{a\mu-F}$ , i.e.,

$$\hat{H}_{A-F} = \sum_{\mu} \hat{H}_{a\mu-F} = \hbar g \sum_{\mu} \left( \hat{a}_{2,\mu}^{\dagger} \hat{a}_{1,\mu} \hat{b} + \hat{b}^{\dagger} \hat{a}_{1,\mu}^{\dagger} \hat{a}_{2,\mu} \right). \quad (2.3)$$

Under the premise of a population inversion, laser action becomes possible by stimulated emission due to photon-mediated atomic transitions from the upper energy level to the lower energy level. As already explained in section 2.1, the frequency and hence also the wavelength of the laser mode is determined by the energy difference  $\Delta E = E_2 - E_1$  between the upper and lower level of the laser transition. Theoretically, this opens up the whole electromagnetic spectrum for potential laser applications, provided that a suitable active medium and a corresponding resonator are available. However, this concept is not limited to photons interacting with atoms. In fact, it could be shown that the principle of stimulated emission can be similarly applied to other signal types besides electromagnetic waves, e.g., phonons [13, 14, 16]. Moreover, the two-level (sub-) system that is involved in the laser transition can also be realized differently, i.e., other than in ensembles of atoms or molecules. For example, the two-level system can be represented by two optical (photon) modes whose transitions are mediated by a mechanical (phonon) mode, as it is the case in the phonon laser system considered in this thesis [24], which is explicitly discussed in sections 2.3.1 and 2.3.2.

This insight forms the basis for various “exotic lasing” concepts such as *phonon lasers* [18–28], *plasmon lasers* [29–33], or *polariton lasers* [34–40]. Similarly, the principle can even be applied to matter waves in so-called *atom lasers* [41–47], where a coherent beam is created out of a *Bose-Einstein condensate* of atoms.

## 2.3 Phonon lasers<sup>2</sup>

As a specific example for the generalization of the lasing principle to signal forms apart from electromagnetic waves, we want to consider the case of a phonon laser. A phonon laser can be understood as the sonic equivalent to a conventional photon laser and is thus also referred to as *SASER*, which is the acronym for *sound amplification by stimulated emission of radiation*. During the last years, phonon lasers have been theoretically discussed or even experimentally realized in the framework of many different approaches.

One of the earliest theoretical suggestions for a phonon laser scheme is a resonator filled with a dielectric liquid with gas bubbles as the active medium [15, 16]. In a different approach, phonon-assisted electron hopping between neighboring quantum wells takes

<sup>2</sup> Part of the text in this section is based on a preliminary study in the course of my diploma thesis [117].

place in a doped semiconductor superlattice with an electrical bias applied to it [17], which is the basis for the coherent phonon amplification in the system presented by Beardsley *et al.* [20]. In contrast, the system presented by Vahala *et al.* consists of a single trapped ion that is driven by a blue-detuned laser beam [18]. Another possibility to realize a phonon laser was demonstrated by Grudinin *et al.*, who implemented a system of two coupled microresonators [19]. Their experiment, which is very similar to the phonon laser treated in this thesis (see section 2.3.1), makes use of the optomechanical interaction between two optical modes and one mechanical mode. Kabuss *et al.* have suggested a phonon-lasing scheme with an optically driven semiconductor quantum dot coupled to an acoustic nanocavity [21, 22]. Beyond that, many other approaches have been reported [23, 25–28, 118], while, in fact, any multi-state system where transitions between the energy levels are phonon-mediated represents a conceivable platform for the realization of a phonon laser, as already mentioned in section 2.2.

Especially because of the high frequencies available (up to the THz range) and due to potential applications in, e.g., sensing, probing and manipulating electronic devices at nanoscale level, or as high precision imaging or measurement instruments, phonon lasers might play an important role in future technological developments.

### 2.3.1 Experimental realization

The phonon laser system considered in this thesis was implemented by our collaborators at the *Micro/Nano Photonics Lab of Washington University in St. Louis* [24]. It consists of two coupled silica whispering-gallery-mode resonators (WGMRs)<sup>3</sup> of equal size, one of which also supports mechanical oscillations. Therefore, the system supports two optical modes, as well as a mechanical mode. Particularly, the first resonator (which also supports the mechanical mode) supports a high-Q optical mode, whereas the second resonator supports a low-Q optical mode. The coupling between the two WGMRs results from the evanescent overlap of the optical modes and hence the coupling strength can be tuned by varying the distance between the two resonator disks. Besides the intrinsic optical resonator decay rates, additional loss can be introduced to the second resonator through a chromium-coated silica nanofiber tip. Light from a tunable external cavity diode laser in the 1550 nm band is coupled into the system via a tapered fiber which is evanescently coupled to the first resonator. Through the same fiber, the output field is sent to a photodetector whose signal is fed into an oscilloscope and an electrical spectrum analyzer. A sketch of the experimental setup is depicted in fig. 2.4.

The uncoupled resonators exhibit the same resonance frequency, which is ensured by thermal control of the two microtoroids. Due to the coupling, however, the eigenmodes of the system are split into two *supermodes*, which are superpositions of the two cavity modes (see section 2.3.2 for more details). In the strong coupling regime, i.e., when the coupling strength is large compared to the optical decay rates, both supermodes are

<sup>3</sup> WGMRs consist of miniaturized dielectric structures having circular symmetry, which sustain electromagnetic waves that circulate within the structure. They are ideally suited for studying optomechanics as they combine ultra high finesse and Q-factors (corresponding to giant photon storage times) with microscale mode volume [119, 120].

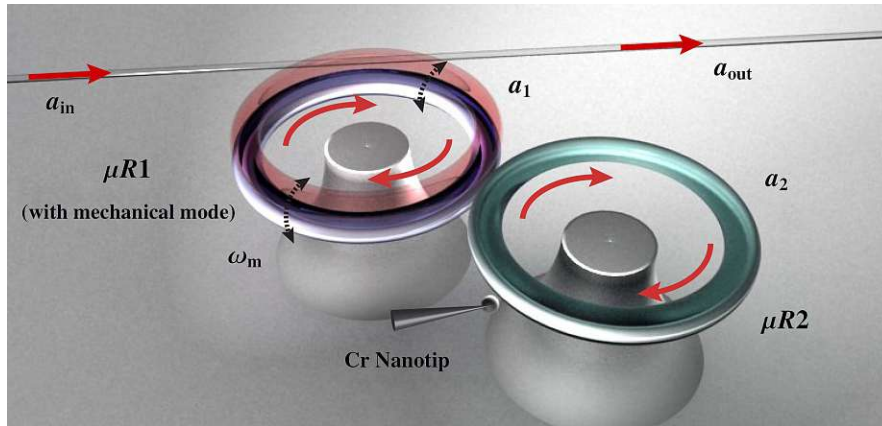


**Figure 2.4:** Experimental setup of the phonon laser from the *Micro/Nano Photonics Lab* at *Washington University in St. Louis*. Two coupled microtoroid resonators  $\mu R1$  and  $\mu R2$  contain the optical modes  $a_1$  and  $a_2$ , where the first resonator  $\mu R1$  also supports mechanical oscillations with resonance frequency  $\omega_m$ . The coupling between the two optical modes can be tuned by changing the distance between the two resonators and additional loss can be introduced to the second resonator with the help of a chromium-coated nanotip. The system is driven by a tunable infrared laser in the 1550 nm band that is evanescently coupled to the first resonator via a tapered fiber.

spatially distributed over both resonator disks and a frequency splitting can be observed (cf. [section 3.1](#)). On the contrary, in the weak coupling regime, they are localized in the individual resonators such that a high-Q supermode exists in the first resonator and a low-Q supermode exists in the second resonator. In this case, the supermode spectra have the same central frequency but different spectral widths corresponding to the respective resonator decay rates.

The basis for the excitation of the phonon mode is the optomechanical interaction between the electromagnetic field and the micromechanical motion in the first resonator. The origin of this interaction, which is the central element in the field of *cavity optomechanics* [121], lies in the radiation pressure forces induced through the momentum carried by light. In this context, the possibility of *Raman scattering* [122, 123] plays an important role, where one can distinguish between *Stokes* and *anti-Stokes scattering*. In a Stokes scattering event, a photon loses part of its energy which is transferred into the mechanical mode by creating a phonon. Similar as in the effect of stimulated emission, this process can be triggered by already existing phonons, such that the vibrational field is coherently amplified (*stimulated Raman scattering*). In contrast, anti-Stokes scattering means that a photon gains energy which is taken from the vibrational field by annihilation of a phonon. This effect can be used for cavity optomechanical cooling [124].

With our compound microcavity system, phonon lasing can be realized in two different ways. One possibility is to tune the system parameters—in particular the inter-cavity coupling strength as well as the additional loss in the second resonator—in such a way that the supermode splitting matches the resonance frequency of the mechanical mode. In this case, the optical supermodes form an effective two-level system similar to the atomic

or molecular energy levels in a conventional optical laser. A corresponding population inversion can be achieved by resonantly pumping the supermode with the higher frequency. The optomechanical interaction in the first resonator enables phonon-mediated transitions between the two optical modes, which leads to a coherent amplification of the mechanical oscillations. If the pump strength is high enough, i.e., above threshold, the mechanical gain exceeds the loss and phonon lasing can be observed. Another possibility to realize a phonon laser with this system is to pump one of the supermodes non-resonantly, where the frequency difference between the blue-detuned pump laser and the respective supermode frequency must match the mechanical resonance. When the system is operated in this way, which is similar to the case of a *Raman laser* [125, 126], the respective supermode serves as the Stokes mode in a stimulated Raman scattering process. Analogously to the other mode of operation, phonon lasing occurs when the pump power is high enough to ensure that the mechanical gain outweighs the cavity losses.

### 2.3.2 Theoretical description

In order to gain a deeper understanding of the functionality of the experimental setup from section 2.3.1 and also to compare the experimental results with numerical simulations, we need to construct a theoretical framework that captures the essence of the relevant physics behind our phonon laser system (cf. [117]). Basically, the system dynamics are governed by the two optical modes  $a_1$  and  $a_2$ , as well as the mechanical mode  $b$ . We can describe these fields in second quantization as harmonic oscillator modes [121] by means of the corresponding creation ( $\hat{a}_{1,2}^\dagger$  and  $\hat{b}^\dagger$ ) and annihilation operators ( $\hat{a}_{1,2}$  and  $\hat{b}$ ). The Hamiltonian of the free (i.e., uncoupled) field modes is then given by

$$\hat{H}_{\text{free}} = \hbar\omega_c \hat{a}_1^\dagger \hat{a}_1 + \hbar\omega_c \hat{a}_2^\dagger \hat{a}_2 + \hbar\omega_m \hat{b}^\dagger \hat{b}, \quad (2.4)$$

where  $\omega_c$  denotes the optical resonance frequency of the uncoupled WGMRs and  $\omega_m$  represents the mechanical resonance frequency. Since both photons and phonons are *bosons*, the operators  $\hat{a}_{1,2}$  and  $\hat{b}$  satisfy the usual bosonic commutator relations

$$[\hat{m}, \hat{n}^\dagger] \equiv \hat{m}\hat{n}^\dagger - \hat{n}^\dagger\hat{m} = \delta_{mn}, \quad (2.5)$$

$$[\hat{m}, \hat{n}] = [\hat{m}^\dagger, \hat{n}^\dagger] = 0, \quad (2.6)$$

where  $\delta_{mn}$  is the *Kronecker delta* and  $\hat{m}$  and  $\hat{n}$  can be replaced by any of the operators  $\hat{a}_1$ ,  $\hat{a}_2$ , or  $\hat{b}$ .

The evanescent overlap in the gap between the two resonators leads to an energy exchange between the optical modes, i.e., transitions from  $a_1$  to  $a_2$  and vice versa. Correspondingly, the optical interaction part of the Hamiltonian depends on the inter-resonator coupling strength  $\kappa$  and is given by

$$\hat{H}_{\text{int}}^{(\text{opt})} = \hbar\kappa (\hat{a}_1^\dagger \hat{a}_2 + \hat{a}_2^\dagger \hat{a}_1). \quad (2.7)$$

Besides this pure optical interaction, there is also the optomechanical interaction in the first resonator, which induces a coupling between the first optical mode  $a_1$  and the mechanical mode  $b$ . The resonance frequency of the optical mode is modulated by the mechanical vibrations and hence is a function of the mechanical displacement  $x$ , which is given by the expectation value of the mechanical displacement operator  $\hat{x} = x_0 (\hat{b} + \hat{b}^\dagger)$ , where  $x_0 = \sqrt{\hbar/(2m\omega_m)}$  is the zero-point fluctuation amplitude of a mechanical oscillator with effective mass  $m$ . Performing a first order *Taylor series expansion* yields

$$\omega_c(x) = \omega_c + x \frac{\partial \omega_c}{\partial x} + \mathcal{O}(x^2) \approx \omega_c - gx, \quad (2.8)$$

in which we have defined the optical frequency shift per displacement [121]

$$g := -\frac{\partial \omega_c}{\partial x}. \quad (2.9)$$

Replacing  $\omega_c$  for the first optical mode in eq. (2.4) by eq. (2.8) directly leads to the optomechanical interaction Hamiltonian

$$\hat{H}_{\text{int}}^{(\text{om})} = -\hbar g x_0 \hat{a}_1^\dagger \hat{a}_1 (\hat{b} + \hat{b}^\dagger), \quad (2.10)$$

for which a more detailed derivation can be found in ref. [127]. The total interaction Hamiltonian then reads

$$\hat{H}_{\text{int}} = \hbar \kappa (\hat{a}_1^\dagger \hat{a}_2 + \hat{a}_2^\dagger \hat{a}_1) - \hbar g x_0 \hat{a}_1^\dagger \hat{a}_1 (\hat{b} + \hat{b}^\dagger). \quad (2.11)$$

The external driving of the system is realized by a continuous-wave laser, which is assumed to be perfectly coherent, such that the driving Hamiltonian can be written as

$$\hat{H}_d = i\hbar (\Omega e^{-i\omega_d t} \hat{a}_1^\dagger - \text{H.c.}), \quad (2.12)$$

where  $\Omega$  is the driving strength,  $\omega_d$  is the driving frequency, and H.c. denotes the Hermitian conjugate. Note that eq. (2.12) represents a semi-classical approximation in which the driving laser is described as a classical field.

The complete system Hamiltonian can be obtained by combining the results of eqs. (2.4), (2.11) and (2.12):

$$\begin{aligned} \hat{H}_{\text{sys}} &= \hat{H}_{\text{free}} + \hat{H}_{\text{int}} + \hat{H}_d \\ &= \hbar \omega_c (\hat{a}_1^\dagger \hat{a}_1 + \hat{a}_2^\dagger \hat{a}_2) + \hbar \omega_m \hat{b}^\dagger \hat{b} + \hbar \kappa (\hat{a}_1^\dagger \hat{a}_2 + \hat{a}_2^\dagger \hat{a}_1) \\ &\quad - \hbar g x_0 \hat{a}_1^\dagger \hat{a}_1 (\hat{b} + \hat{b}^\dagger) + i\hbar (\Omega e^{-i\omega_d t} \hat{a}_1^\dagger - \text{H.c.}). \end{aligned} \quad (2.13)$$

For our further analysis, we are mainly interested in the comparatively slow dynamics of the phonon mode rather than the rapidly oscillating optical modes. It is thus convenient to transform the optical modes to a reference frame rotating at the driving frequency  $\omega_d$ ,

i.e.,  $\hat{a}_{1,2}^{(\text{old})} \rightarrow e^{-i\omega_d t} \hat{a}_{1,2}^{(\text{new})}$ . To this end, we apply the unitary transformation

$$\hat{U} = e^{i\omega_d t (\hat{a}_1^\dagger \hat{a}_1 + \hat{a}_2^\dagger \hat{a}_2)}, \quad (2.14)$$

which generates a new Hamiltonian with time-independent driving of the form

$$\begin{aligned} \hat{H} &= \hat{U} \hat{H}_{\text{sys}} \hat{U}^\dagger - i\hbar \hat{U} \frac{\partial \hat{U}^\dagger}{\partial t} \\ &= -\hbar \Delta (\hat{a}_1^\dagger \hat{a}_1 + \hat{a}_2^\dagger \hat{a}_2) + \hbar \omega_m \hat{b}^\dagger \hat{b} + \hbar \kappa (\hat{a}_1^\dagger \hat{a}_2 + \hat{a}_2^\dagger \hat{a}_1) \\ &\quad - \hbar g x_0 \hat{a}_1^\dagger \hat{a}_1 (\hat{b} + \hat{b}^\dagger) + i\hbar (\Omega \hat{a}_1^\dagger - \text{H.c.}), \end{aligned} \quad (2.15)$$

where  $\Delta = \omega_d - \omega_c$  is the detuning between the driving laser frequency and the optical cavity resonance frequency. With the help of the Hamiltonian eq. (2.15) we are now in the position to derive the *Heisenberg equations of motion* for our system, which can be written for an arbitrary operator  $\hat{o}$  according to

$$\frac{d}{dt} \hat{o} = \frac{i}{\hbar} [\hat{H}, \hat{o}]. \quad (2.16)$$

Up to now, however, we have not taken any fluctuation or dissipation effects into account. These influences stem from the interaction of the system with heat baths and are treated within the framework of input-output theory [128, 129] (see appendix A.1 for more details). As a result, eq. (2.16) needs to be extended by adding terms representing loss and quantum noise,

$$\frac{d}{dt} \hat{o} = \frac{i}{\hbar} [\hat{H}, \hat{o}] - \gamma \hat{o} + \hat{\Gamma}, \quad (2.17)$$

where  $\gamma$  is the decay rate of the operator  $\hat{o}$  and  $\hat{\Gamma}$  is a statistical noise operator. The complete Heisenberg equations of motion for our system are then given by

$$\dot{\hat{a}}_1(t) = (i\Delta - \gamma_1) \hat{a}_1(t) - i\kappa \hat{a}_2(t) + i g x_0 \hat{a}_1(t) (\hat{b}(t) + \hat{b}^\dagger(t)) + \Omega + \hat{\Gamma}_1(t), \quad (2.18)$$

$$\dot{\hat{a}}_2(t) = (i\Delta - \gamma_2) \hat{a}_2(t) - i\kappa \hat{a}_1(t) + \hat{\Gamma}_2(t), \quad (2.19)$$

$$\dot{\hat{b}}(t) = (-i\omega_m - \gamma_m) \hat{b}(t) + i g x_0 \hat{a}_1^\dagger(t) \hat{a}_1(t) + \hat{\Gamma}_b(t), \quad (2.20)$$

in which  $\gamma_{1,2}$  are the optical decay rates,  $\gamma_m$  is the mechanical decay rate, and  $\hat{\Gamma}_{1,2}$  and  $\hat{\Gamma}_b$  are the optical and mechanical noise operators. The fluctuations are assumed to represent a *Markovian*<sup>4</sup> white noise with zero mean and finite variance. Therefore, the statistical averages<sup>5</sup> of the noise operators in eqs. (2.18) to (2.20) are all equal to zero,

$$\langle \hat{\Gamma}_1(t) \rangle = \langle \hat{\Gamma}_2(t) \rangle = \langle \hat{\Gamma}_b(t) \rangle = 0, \quad (2.21)$$

<sup>4</sup> A *Markov process* is *memoryless*, i.e., the probability distribution of a future state does not depend on previous events but only on the current state.

<sup>5</sup> Average over many different realizations, denoted by angle brackets.



and the individual operators are delta-correlated, i.e., satisfying the correlation relations

$$\langle \hat{\Gamma}_1(t) \hat{\Gamma}_1^\dagger(t') \rangle = 2\gamma_1 (\bar{n}_{\text{th}}^{(\text{opt})} + 1) \delta(t - t'), \quad (2.22)$$

$$\langle \hat{\Gamma}_1^\dagger(t) \hat{\Gamma}_1(t') \rangle = 2\gamma_1 \bar{n}_{\text{th}}^{(\text{opt})} \delta(t - t'), \quad (2.23)$$

$$\langle \hat{\Gamma}_2(t) \hat{\Gamma}_2^\dagger(t') \rangle = 2\gamma_2 (\bar{n}_{\text{th}}^{(\text{opt})} + 1) \delta(t - t'), \quad (2.24)$$

$$\langle \hat{\Gamma}_2^\dagger(t) \hat{\Gamma}_2(t') \rangle = 2\gamma_2 \bar{n}_{\text{th}}^{(\text{opt})} \delta(t - t'), \quad (2.25)$$

$$\langle \hat{\Gamma}_b(t) \hat{\Gamma}_b^\dagger(t') \rangle = 2\gamma_m (\bar{n}_{\text{th}}^{(\text{mech})} + 1) \delta(t - t'), \quad (2.26)$$

$$\langle \hat{\Gamma}_b^\dagger(t) \hat{\Gamma}_b(t') \rangle = 2\gamma_m \bar{n}_{\text{th}}^{(\text{mech})} \delta(t - t'), \quad (2.27)$$

with the average number of thermally excited photons  $\bar{n}_{\text{th}}^{(\text{opt})} \approx (e^{\hbar\omega_c/k_B T} - 1)^{-1}$  and the average number of thermally excited phonons  $\bar{n}_{\text{th}}^{(\text{mech})} \approx (e^{\hbar\omega_m/k_B T} - 1)^{-1}$ , where  $T$  is the environmental temperature and  $k_B$  is the Boltzmann constant. For all other combinations of the noise operators, the correlation functions vanish [129].

In order to perform numerical simulations of our phonon laser system, the operator equations eqs. (2.18) to (2.20) as well as the noise operator correlations eqs. (2.22) to (2.27) need to be transformed to corresponding c-number equations, which is elaborated in ref. [117]. In addition, technical details about the numerical solution of the resulting equations can be found there.

Under the assumption that the optomechanical interaction is small as compared to the optical coupling and decay rates—which is satisfied in good approximation for the system under consideration (see table 3.1), at least below or only slightly above threshold—the characteristics of the optical modes are hardly influenced by the mechanical mode. For this case, it is justified to neglect the optomechanical coupling and consider the two optical modes alone. The isolated system consisting only of the two optical modes is then described by the equations

$$\dot{\hat{a}}_1(t) = (i\Delta - \gamma_1) \hat{a}_1(t) - i\kappa \hat{a}_2(t) + \Omega + \hat{\Gamma}_1(t), \quad (2.28)$$

$$\dot{\hat{a}}_2(t) = (i\Delta - \gamma_2) \hat{a}_2(t) - i\kappa \hat{a}_1(t) + \hat{\Gamma}_2(t), \quad (2.29)$$

which can be compactly written as a matrix equation,

$$\frac{d}{dt} \begin{pmatrix} \hat{a}_1(t) \\ \hat{a}_2(t) \end{pmatrix} = -i \underbrace{\begin{pmatrix} -\Delta - i\gamma_1 & \kappa \\ \kappa & -\Delta - i\gamma_2 \end{pmatrix}}_M \begin{pmatrix} \hat{a}_1(t) \\ \hat{a}_2(t) \end{pmatrix} + \begin{pmatrix} \Omega + \hat{\Gamma}_1(t) \\ \hat{\Gamma}_2(t) \end{pmatrix}. \quad (2.30)$$

As already mentioned in section 2.3.1, the coupling of the two cavity modes induces the formation of two new eigenmodes (*supermodes*). Solving the characteristic equation

$$|M - \lambda \mathbb{1}| = \begin{vmatrix} -\Delta - i\gamma_1 - \lambda & \kappa \\ \kappa & -\Delta - i\gamma_2 - \lambda \end{vmatrix} = 0 \quad (2.31)$$

yields the solutions for the eigenvalues of the system matrix  $M$ ,

$$\lambda_{\pm} = -\Delta - i\frac{\gamma_1 + \gamma_2}{2} \pm \sqrt{\kappa^2 - \frac{(\gamma_2 - \gamma_1)^2}{4}}, \quad (2.32)$$

where the real parts of the complex supermode frequencies represent the new supermode resonant frequencies  $\omega_{\pm} = \text{Re}(\lambda_{\pm})$  and the negative imaginary parts give the associated dissipation rates  $\gamma_{\pm} = -\text{Im}(\lambda_{\pm})$ . Analogously, the corresponding eigenvectors (supermodes) are defined by the equation

$$(M - \lambda_{\pm}\mathbb{1})\mathbf{v}_{\pm} = \mathbf{0} \quad (2.33)$$

and the solutions read

$$\mathbf{v}_{\pm} = \frac{1}{N_{\pm}} \left( i(\gamma_2 - \gamma_1) \pm \sqrt{4\kappa^2 - (\gamma_2 - \gamma_1)^2} \right), \quad (2.34)$$

with the normalization constants

$$N_{\pm} = \begin{cases} \sqrt{8}\kappa & \text{if } 4\kappa^2 \geq (\gamma_2 - \gamma_1)^2 \\ \sqrt{4\kappa^2 + \left(\gamma_2 - \gamma_1 \pm \sqrt{(\gamma_2 - \gamma_1)^2 - 4\kappa^2}\right)^2} & \text{if } 4\kappa^2 < (\gamma_2 - \gamma_1)^2 \end{cases}. \quad (2.35)$$

In other words, the supermodes are linear combinations of the cavity modes  $\hat{a}_1$  and  $\hat{a}_2$ ,

$$\hat{a}_{\pm}(t) = \frac{1}{N_{\pm}} \left[ \left( i(\gamma_2 - \gamma_1) \pm \sqrt{4\kappa^2 - (\gamma_2 - \gamma_1)^2} \right) \hat{a}_1(t) + 2\kappa \hat{a}_2(t) \right]. \quad (2.36)$$

By rearranging eq. (2.36), the cavity modes can be expressed through the supermodes and substituting the resulting expressions into eq. (2.15) yields the system Hamiltonian on the supermode level, which contains terms proportional to  $\hat{a}_+^{\dagger} \hat{a}_- \hat{b}$  and  $\hat{b}^{\dagger} \hat{a}_+^{\dagger} \hat{a}_-$ , respectively. These terms feature the same structure as the corresponding terms in eq. (2.3) describing the interaction between the active medium and the field in a laser, where here the phonon mode  $\hat{b}$  plays the role of the laser mode and the two optical supermodes  $\hat{a}_+$  and  $\hat{a}_-$  represent the energy levels of the active medium. Consequently, the occurrence of phonon laser action in our system can be expected under suitable parameter settings, subject to a sufficiently high pump strength  $\Omega$ .

# Chapter 3

## Phonon lasing near an exceptional point

### 3.1 Exceptional points

An interesting feature of non-Hermitian systems is the possible occurrence of so-called exceptional points. The term *exceptional point* (EP) has been introduced by Kato [51] and it refers to a special type of spectral degeneracy at which not only some of the eigenvalues of a system but also the corresponding eigenvectors coalesce [52–54]. As a simple example, let us consider the following non-Hermitian  $2 \times 2$  matrix

$$M_0 = \begin{pmatrix} \delta - i\gamma_1 & g \\ g & -i\gamma_2 \end{pmatrix} \quad (3.1)$$

with real parameters  $\delta$ ,  $\gamma_1$ ,  $\gamma_2$ , and  $g$ . The matrix  $M_0$  could describe a system of two modes (in a rotating frame) with intrinsic loss rates  $\gamma_1$  and  $\gamma_2$ , which are coupled with coupling strength  $g$ . The parameter  $\delta$  corresponds to the difference between the resonance frequencies of the two modes. By tuning these parameters in a proper way, an EP can be induced in the matrix  $M_0$ . Figure 3.1 illustrates the topology of the two eigenvalues as a function of the parameters  $\delta$  and  $g$ , while the values of  $\gamma_1$  and  $\gamma_2$  are kept constant. As one can see, the eigenvalues form two intersecting Riemann sheets and the point where both the real and the imaginary parts of the two eigenvalues are equal represents the EP.

In many cases, the appearance of an EP leads to interesting and often also counter-intuitive phenomena [55]. For instance, the above-threshold behavior of lasers can be drastically influenced by EPs, where a counter-intuitive laser turn-off occurs although the overall pump power deposited in the system is increased [56, 57]. Similarly, the opposite effect can be observed when a laser switches on although the total loss of the system is increased [58]. Furthermore, the strong asymmetric backscattering in the vicinity of an EP can lead to chiral behavior and unidirectional emission such that by transiting from one EP to another one the direction of emission can be completely reversed [59]. Similarly, it is possible to switch between different states in a system of coupled oscillator modes by an adiabatic encircling of an EP [60, 130]. Next to many other possible applications, the physics of EPs is also of special interest in the context of *parity-time-symmetric* ( $\mathcal{PT}$ -symmetric) systems. While it was shown that also a non-Hermitian Hamiltonian can have an entirely real spectrum if the system satisfies the condition of  $\mathcal{PT}$ -symmetry [96], a symmetry-breaking, where the eigenvalues become complex, is

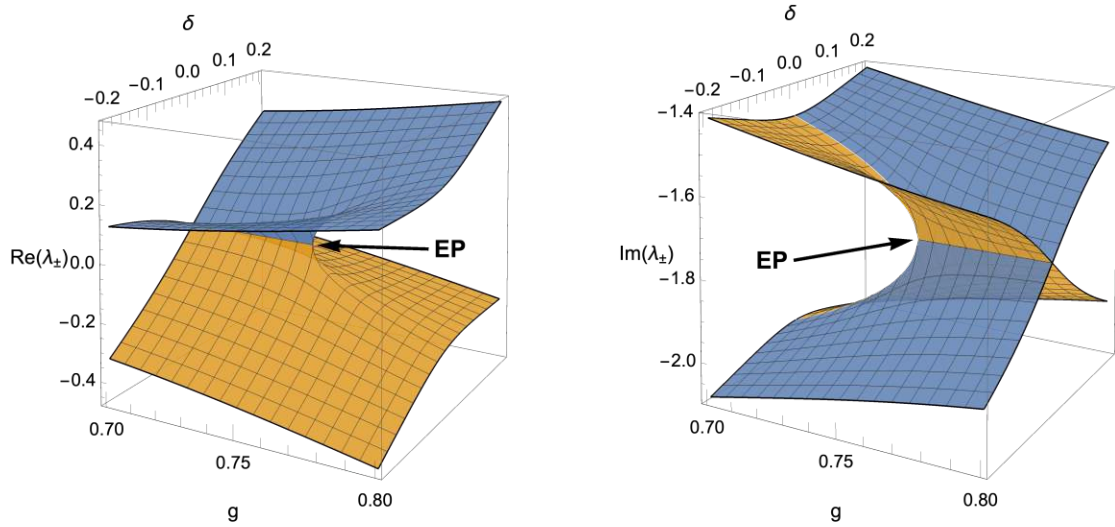


**Figure 3.1:** Eigenvalues of the non-Hermitian matrix  $M_0$  from eq. (3.1) as a function of  $\delta$  and  $g$  for constant parameters  $\gamma_1 = 1$  and  $\gamma_2 = 2.5$ . The left picture shows the real part and the right picture shows the imaginary part of the two eigenvalues  $\lambda_{\pm}$ .

always connected with the occurrence of an EP in the system [98, 99, 131, 132].

Since our phonon laser supports only one phonon mode, it is not possible to induce an EP in the mechanical part of the system. Instead, the optical supermodes, which represent the energy levels of the gain medium, can be brought to an EP. Actually, the matrix

$$M = \begin{pmatrix} -\Delta - i\gamma_1 & \kappa \\ \kappa & -\Delta - i\gamma_2 \end{pmatrix} \quad (3.2)$$

from eq. (2.30) that describes the isolated optical modes (i.e., without optomechanical interaction) looks very similar to the matrix  $M_0$  in eq. (3.1). Having a closer look on its eigenvalues eq. (2.32) and eigenvectors eq. (2.34), one can immediately see that an EP occurs if the condition

$$4\kappa^2 = (\gamma_2 - \gamma_1)^2 \quad (3.3)$$

is satisfied, which can be achieved if either the optical coupling strength  $\kappa$  or one of the optical loss rates  $\gamma_1$  or  $\gamma_2$  can be adequately controlled. In our experimental setup, the loss in the first resonator as well as the distance between the two WGMRs and hence also the optical coupling are fixed. However, the loss in the second resonator can be tuned with the help of the nanotip (see section 2.3.1), which allows us to steer the system through an EP by varying the distance between the nanotip and the second resonator. This behavior is presented in fig. 3.2, which shows the dependence of the complex eigenvalues eq. (2.32) on the additional loss introduced by the tip ( $\gamma_{\text{tip}}$ ).

Due to these properties, our system can be used to study the influence of an EP on the lasing characteristics. In particular, an interesting effect on the laser linewidth can be expected, as outlined in section 3.2.

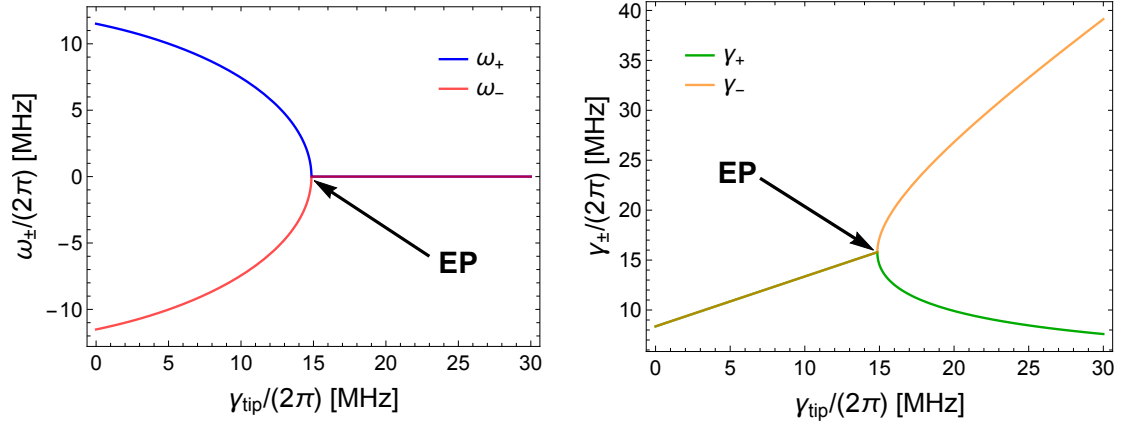


**Figure 3.2:** Frequencies  $\omega_{\pm} = \text{Re}(\lambda_{\pm})$  (left) and dissipation rates  $\gamma_{\pm} = -\text{Im}(\lambda_{\pm})$  (right) of the supermodes  $\hat{a}_{\pm}$  as a function of  $\gamma_{\text{tip}}$ . The other parameters are taken from table 3.1.

## 3.2 Laser linewidth

Although lasers are characterized by a high degree of coherence, an important property of laser radiation is the intrinsic linewidth, which arises because of quantum and thermal fluctuations. Even before the first laser was experimentally realized, Schawlow and Townes have found a fundamental limit for the laser linewidth which is given by the famous Schawlow-Townes formula [1]

$$\Delta\omega_{\text{ST}} = \frac{\hbar\omega_0\gamma_0^2}{2P}, \quad (3.4)$$

where  $\omega_0$  is the laser frequency,  $\gamma_0$  is the passive cavity resonance width, and  $P$  is the output power of the laser. During the following decades, several multiplicative correction factors to the Schawlow-Townes formula have been introduced. One of these corrections is the *bad cavity factor*  $\tilde{\gamma}$  [133], which arises if the gain linewidth  $\gamma_{\perp}$  is on the order of or smaller than the passive cavity resonance width  $\gamma_0$  and causes the substitution of  $\gamma_0$  in eq. (3.4) with  $\tilde{\gamma} = \frac{2\gamma_{\perp}\gamma_0}{2\gamma_{\perp} + \gamma_0}$ . Another correction results from the incomplete inversion of the gain medium and is referred to as *spontaneous emission factor*  $n_{\text{sp}} = \frac{N_2}{N_2 - N_1}$  [134], where  $N_2$  and  $N_1$  are the spatially averaged populations in the upper and lower states of the lasing transition. Furthermore, the laser linewidth is modified by the *Henry  $\alpha$  factor* [135], which is caused by the nonlinear coupling between the amplitude and phase fluctuations of the laser field. Finally, the laser linewidth is enhanced by the *Petermann factor*  $K$  [63]. Due to the presence of the gain medium as well as the openness of the laser cavity, the modes are not power-orthogonal, which results in an enhancement of the noise power [64, 65, 136]. While such behavior has already been experimentally verified [66, 137], it was only subsequently associated with the presence of a nearby EP [62]. Directly at an EP, two or more resonator modes become completely non-orthogonal (i.e., parallel), which should thus lead to a significant linewidth broadening.

Altogether, these correction factors lead to an improved linewidth formula of the form

$$\Delta\omega = \frac{\hbar\omega_0\tilde{\gamma}^2}{2P} \cdot n_{\text{sp}} \cdot (1 + \alpha^2) \cdot K. \quad (3.5)$$

It should be noted, however, that the correction factors in eq. (3.5) have been derived under certain approximations and do not fully consider the spatial dependence of the electric field or nonlinear effects like *spatial hole-burning*. In recent years, a linewidth theory which also takes such effects into account has been proposed [138–140]. This theory is based on the *steady-state ab initio laser theory* (SALT) [141, 142]. However, the equations of our phonon laser system eqs. (2.18) to (2.20) have a different structure as the conventional laser equations treated in the framework of SALT. Therefore, SALT is not directly applicable and the phonon laser linewidth has to be calculated numerically as described in ref. [117].

### 3.3 Experimental and theoretical results<sup>6</sup>

Our phonon laser system described in sections 2.3.1 and 2.3.2 provides an ideal platform to study the effects of an exceptional point on the behavior of a laser. In particular, the effect of such a spectral singularity on the laser linewidth is of enormous interest to provide insights into the long-debated issue of how a laser is affected when being operated at an EP. Indeed, we find a significant broadening of the phonon laser linewidth but also a significant reduction of the lasing threshold in the vicinity of the EP, as presented in sections 3.3.1 and 3.3.2.

The system parameters as determined from the experiment are given in table 3.1. These parameter values were also used in the theoretical analysis presented in this chapter. As opposed to the other parameters, the value for the optomechanical coupling  $gx_0$  was not directly measured but rather estimated from a comparison between the measured and the numerically determined threshold pump power.

As explained in section 3.1, an EP can be induced in the optical part of the system by tuning the additional loss introduced by the nanotip, i.e., the loss rate in the second

<sup>6</sup> The experimental results presented in this section were generated by the *Micro/Nano Photonics Lab* at *Washington University in St. Louis*. Part of the results and figures are taken from our joint publication [24] or have been provided by Şahin Özdemir in private communication. The theoretical analysis is partially based on a preliminary study in the course of my diploma thesis [117].

**Table 3.1:** Experimentally determined phonon laser system parameters, which were also used in the theoretical calculations.

$\omega_c$ :	$2\pi \cdot 1.93 \cdot 10^{14}$ Hz	$\omega_m$ :	$2\pi \cdot 17.38$ MHz
$\kappa$ :	$2\pi \cdot 12.63$ MHz	$gx_0$ :	$2\pi \cdot 160$ Hz
$\gamma_1$ :	$2\pi \cdot 3.16$ MHz	$\gamma_m$ :	$2\pi \cdot 40$ kHz
$\gamma_2$ :	$2\pi \cdot 13.56$ MHz		

resonator is changed according to  $\gamma_2 \rightarrow \gamma_{2,0} + \gamma_{\text{tip}}$ , where  $\gamma_{2,0}$  is the intrinsic loss of the second WGMR as given in table 3.1 and  $\gamma_{\text{tip}}$  is the loss induced by the tip. With the help of eq. (3.3), we can calculate the value of  $\gamma_{\text{tip}}$  where the EP arises, which evaluates to  $\gamma_{\text{tip}}^{\text{EP}} = 2\pi \cdot 14.86 \text{ MHz}$ . In the following, the situation with  $\gamma_{\text{tip}} < \gamma_{\text{tip}}^{\text{EP}}$  will be referred to as the regime *before* the EP or the *strong coupling regime* and analogously for  $\gamma_{\text{tip}} > \gamma_{\text{tip}}^{\text{EP}}$  the regime *after* the EP or the *weak coupling regime*.

### 3.3.1 Phonon laser threshold

As a first example of the influence of an EP on the properties of our phonon laser, we investigate the behavior of the lasing threshold. Just like for any other type of laser, the output power of our phonon laser features a clear threshold behavior as a function of the pump power, which was measured for different values of  $\gamma_{\text{tip}}$  (see fig. 3.3a). For increasing pump power, the phonon laser output power remains close to zero until a certain threshold value is reached above which the laser amplification sets in and the output power increases rapidly. This behavior can also be observed in numerical simulations [117]. Below threshold, the output power is not exactly zero but rises slowly with increasing driving strength. The value of the threshold pump power, at which the slope of the curve increases by several orders of magnitude, strongly depends on the additional loss  $\gamma_{\text{tip}}$ . As it turns out, the threshold first slightly increases with growing  $\gamma_{\text{tip}}$  but then experiences a sudden drop as the system approaches the EP. Remarkably, the threshold remains low even if the additional loss through the tip is further increased in the regime after the EP. This behavior is illustrated in fig. 3.3b.

In order to gain a better understanding of the relevant physics, we have derived an analytical approximation of the phonon laser threshold. As discussed in appendix A.2,

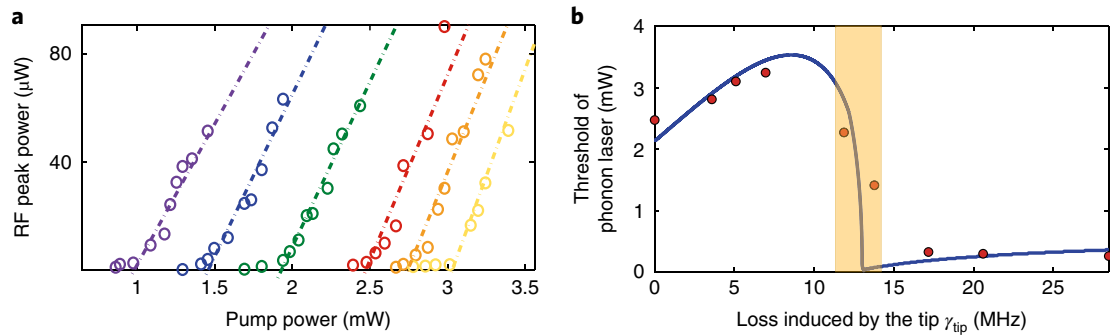


**Figure 3.3:** Experimental results for the phonon laser threshold behavior. The left plot (a) shows the phonon laser output power as a function of the optical pump power, which is measured for different values of  $\gamma_{\text{tip}}/(2\pi)$ : 0 MHz (red), 3.8 MHz (orange), 6.9 MHz (yellow), 11.9 MHz (green), 13.8 MHz (blue), and 17.2 MHz (purple). The right plot (b) depicts the dependence of the threshold pump power on the value of  $\gamma_{\text{tip}}$ , where the circles denote the experimental data points and the solid curve serves as a guide to the eye. The orange shaded area represents the vicinity of the EP.

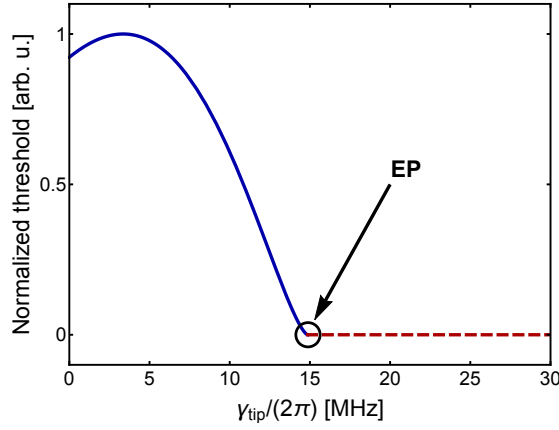


**Figure 3.4:** Analytical approximation for the phonon laser threshold behavior. The plot illustrates the dependence of the threshold pump power on the value of  $\gamma_{\text{tip}}$  based on an analytical approximation. The blue solid curve represents the result in the regime before the EP, whereas the red dashed curve corresponds to the regime after the EP.

the threshold pump power in the regime before the EP can be approximated by

$$P_{\text{thr}} = \frac{4\chi\hbar\omega_c\gamma_m\beta^3 [4\chi^2 + (2\beta - \omega_m)^2]}{(gx_0)^2\kappa^2 [2\beta\chi + \gamma(2\beta - \omega_m)]}, \quad (3.6)$$

whereas in the regime after the EP the approximation yields a vanishing threshold pump power, i.e.,

$$P_{\text{thr}} \equiv 0. \quad (3.7)$$

This result is displayed in [fig. 3.4](#). While the analytical approximation features a certain similarity to the experimental data, it is conspicuous that the value of the threshold pump power drops to zero at the EP and in the regime after the EP. The reason for this observation is a divergence of the effective optomechanical coupling strength in the vicinity of the EP and a similar behavior in the regime after it, which occurs as a result of the simplifications that are necessary for an analytical treatment (see [appendix A.2](#) for more details). Such an unphysical divergence is clearly an artifact due to the approximations made and implies that a more complete model would be required to describe this parameter regime correctly.

Representing a more realistic theoretical result, we have also performed numerical simulations to calculate the threshold pump power. For any given set of input parameters we can numerically determine whether the system is below or above threshold by means of a linear stability analysis as described in [appendix A.3](#). Thus, it is possible to find the laser threshold by systematically varying the pump power while keeping all other parameters constant and simultaneously evaluating the stability of the linearized system equations. With this method, it is possible to calculate the threshold pump power  $P_{\text{thr}}$  as a function of the additional loss  $\gamma_{\text{tip}}$ , which is presented in [fig. 3.5](#). The numerical results reveal that the threshold dependence of the variable loss parameter  $\gamma_{\text{tip}}$  strongly



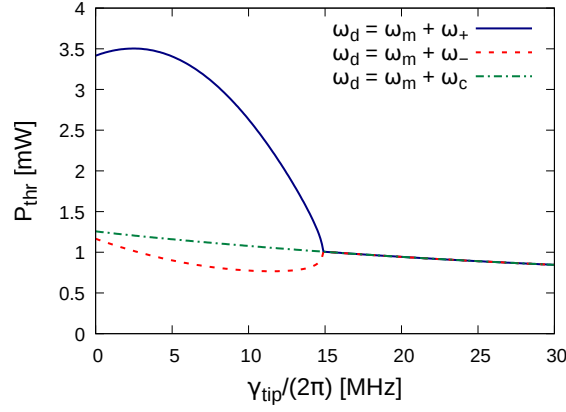


**Figure 3.5:** Numerical results for the phonon laser threshold behavior. The plot illustrates the dependence of the threshold pump power on the value of  $\gamma_{\text{tip}}$  for three different driving frequencies  $\omega_d$ .

depends on the driving frequency  $\omega_d$ . In the first case, we pump the supermode  $\hat{a}_+$  non-resonantly with a frequency offset that corresponds to the mechanical resonance frequency, i.e.,  $\omega_d = \omega_+ + \omega_m$ . Therefore, the Stokes sideband lies within the resonance of the supermode  $\hat{a}_+$  such that phonons can be efficiently created in a stimulated Raman scattering process. This driving frequency corresponds to the assumptions included in the analytical treatment leading to eqs. (3.6) and (3.7), and also to the experimental procedure. Similar to the measured results, the threshold first slightly increases, drops significantly when the system is steered to the EP, and remains low as  $\gamma_{\text{tip}}$  is further increased. Unlike the analytical approximation, however, the numerical result is always greater than zero. In the second case, we investigate the situation with  $\omega_d = \omega_- + \omega_m$ , i.e., we pump the supermode  $\hat{a}_-$  non-resonantly with a frequency offset of  $\omega_m$ . Since the frequency splitting between the two supermodes in the regime before the EP is on the order of the mechanical resonance frequency ( $\omega_+ - \omega_- \approx 2\pi \cdot 23$  MHz for  $\gamma_{\text{tip}} = 0$ ), the pump mode lies within the frequency band of the upper supermode level with the Stokes sideband being on resonance with the lower supermode level such that coherent phonons can be created through stimulated Raman scattering into the lower supermode level as well as through photon transitions from the upper to the lower supermode level. In this way, the phonon generation is highly efficient such that the threshold pump power becomes significantly lower as compared to the first case. In the regime after the EP, both supermode frequencies and hence also the corresponding threshold curves are identical. The kink in the curves directly at the EP is not a special feature of the EP but stems from the fact that already the driving frequency  $\omega_d = \omega_{\pm} + \omega_m$  features a kink at the EP in both cases (cf. fig. 3.2). For comparison, we also present the case with constant driving frequency  $\omega_d = \omega_c + \omega_m$  (the same value as in the regime after the EP from the previous cases), where the threshold decreases monotonously with increasing  $\gamma_{\text{tip}}$  (in the investigated parameter range).

The generation of phonons in our system is a result of the optomechanical interaction. Therefore, the shape of the threshold curves from fig. 3.5 is closely related to the intra-

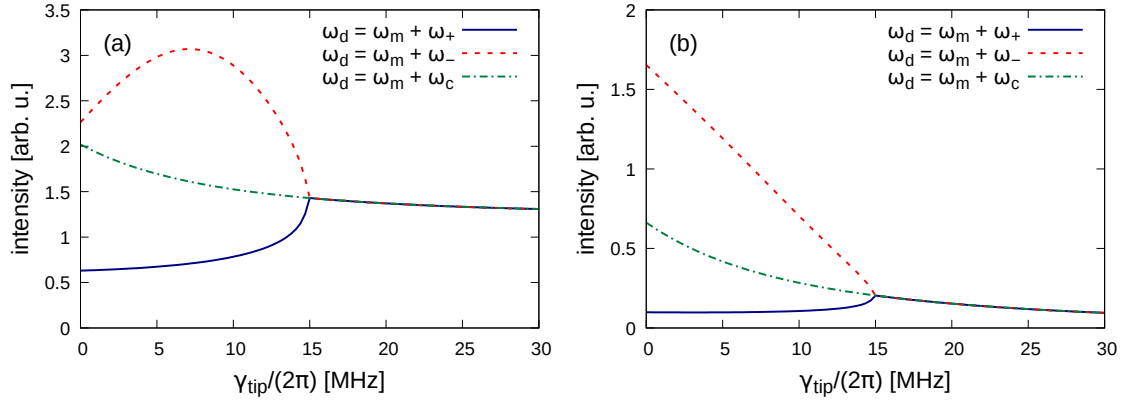


**Figure 3.6:** Intra-cavity field intensity of the optical modes in our phonon laser system below threshold. The left plot (a) shows the intensity of the optical mode  $\hat{a}_1$  in the first resonator, whereas the right plot (b) depicts the intensity of the second optical mode  $\hat{a}_2$ . In both cases, the intensity is evaluated for three different driving frequencies  $\omega_d$  with constant driving strength  $\Omega$ .

cavity field intensity of the cavity mode  $\hat{a}_1$  in the first resonator, which is displayed as a function of  $\gamma_{\text{tip}}$  in [fig. 3.6a](#). For completeness, we also present the intensity of the cavity mode  $\hat{a}_2$  from the second resonator in [fig. 3.6b](#). In accordance with the threshold behavior in the regime before the EP, we find that for  $\omega_d = \omega_+ + \omega_m$  the intensity of the optical field in the first resonator is much lower than for the case with  $\omega_d = \omega_- + \omega_m$ . Since the mechanical mode is located in the first resonator, a lower field intensity of the corresponding cavity mode  $\hat{a}_1$  means that for fixed input power less energy can be transferred from the optical modes to the phonon mode such that the threshold of the phonon laser is increased. Apart from other influences like the ratio between the supermode frequency splitting and the mechanical resonance frequency, the phonon laser threshold is therefore strongly dependent on the spatial distribution of the supermodes. In the strong coupling regime (before the EP), each of the supermodes is distributed over both resonators, as can be directly seen from [eq. \(2.36\)](#). For the special case  $\gamma_1 = \gamma_2$ , the two supermodes would be equally distributed in the first and second resonator. Increasing the value of  $\gamma_{\text{tip}}$  beyond the EP into the weak coupling regime results in a strong localization of one supermode in the first resonator and the other one in the second resonator, where in the limit  $\gamma_{\text{tip}} \rightarrow \infty$  we have  $\hat{a}_+ \rightarrow \hat{a}_1$  and  $\hat{a}_- \rightarrow \hat{a}_2$ .

### 3.3.2 Phonon laser linewidth

While a direct measurement of the laser linewidth broadening at an EP remained out of reach during the last decades, this situation changed with the availability of phonon lasers. The reason for that is that the linewidth of mechanical oscillations with MHz to THz frequencies can be measured more precisely than for their optical counterparts at the relevant laser frequencies ( $\sim 10^{12} - 10^{15}$  Hz).

In [fig. 3.7a](#), we present measured phonon laser power spectra for various values of  $\gamma_{\text{tip}}$ , where the pump power was tuned in such a way that all curves have the same peak output

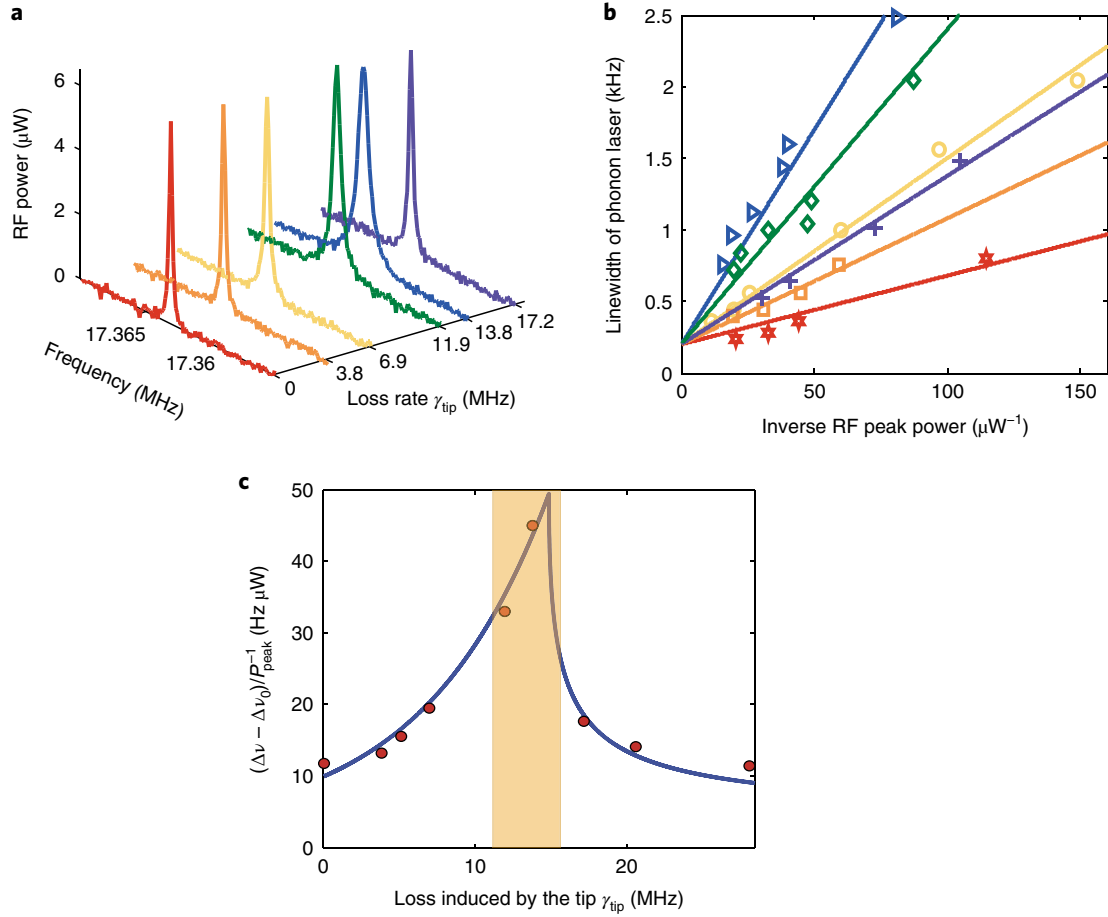


**Figure 3.7:** Experimental results for the phonon laser linewidth behavior. (a) Measured power spectra for different values of  $\gamma_{\text{tip}}$ . (b) Phonon laser linewidth as a function of the inverse output power. The different colors correspond to the different values of  $\gamma_{\text{tip}}$  in (a). (c) Linewidth enhancement as a function of  $\gamma_{\text{tip}}$ , where the circles denote the experimental data points and the solid curve serves as a guide to the eye. The orange shaded area represents the vicinity of the EP. All frequencies in this figure are divided by a factor of  $2\pi$ .

power. As one can see, the spectral width of the phonon signal first increases and then decreases when we tune  $\gamma_{\text{tip}}/(2\pi)$  from 0 to 17.2 MHz, i.e., steering the system through the EP that occurs at 14.86 MHz. Furthermore, we find that the phonon laser linewidth  $\Delta\nu$  is proportional to the inverse output power, except for a small phenomenological shift  $\Delta\nu_0$  which takes into account all power-independent noise sources that are not included in our model (see fig. 3.7b). The linear relationship between the linewidth and the inverse output power is also evident from numerical simulations [117] and represents the well-known behavior that was already predicted by the Schawlow-Townes formula eq. (3.4). The slopes of the different curves correspond to the spectral peak widths in fig. 3.7a. Finally, fig. 3.7c illustrates the normalized linewidth  $(\Delta\nu - \Delta\nu_0) \cdot P_{\text{peak}}^{-1}$  as a function of the loss introduced by the tip  $\gamma_{\text{tip}}$ . It can be clearly observed that the linewidth first increases in the regime before the EP but then decreases again when the loss is further augmented to steer the system into the regime after the EP.

In order to obtain a physical intuition of the mechanism behind the phonon laser linewidth broadening in the vicinity of the EP, we investigate the behavior of the optical modes in this parameter regime. In a very simplified approach, the two coupled optical modes present in our setup can be modeled by a system of beam splitters [143], which is schematically illustrated in the left part of fig. 3.8. In this picture, the coupling (without coupling losses) between the optical modes  $\hat{a}_1$  and  $\hat{a}_2$  is quantified by the reflection and transmission coefficients  $r$  and  $t$ . Noise and decay are modeled by coupling each of the two optical modes to a corresponding loss mode ( $\hat{c}_1$  and  $\hat{c}_2$ ) via beam splitters with reflection and transmission coefficients  $r_{1,2}$  and  $t_{1,2}$ , respectively. All reflection and transmission coefficients are assumed to be real and satisfy the relation  $|r_i|^2 + |t_i|^2 = 1$ . The influence of the optomechanical interaction is neglected for simplicity. One round trip in this cavity is then described by the following four-mode unitary scattering matrix:

$$S = \begin{pmatrix} t t_1 & r t_1 & r_1 & 0 \\ -r t_2 & t t_2 & 0 & r_2 \\ -t r_1 & -r r_1 & t_1 & 0 \\ r r_2 & -t r_2 & 0 & t_2 \end{pmatrix}. \quad (3.8)$$

Since we are not explicitly interested in the loss modes, we can reduce our considerations to the truncated scattering matrix for the cavity modes  $\hat{a}_1$  and  $\hat{a}_2$ ,

$$\sigma = \begin{pmatrix} t t_1 & r t_1 \\ -r t_2 & t t_2 \end{pmatrix}, \quad (3.9)$$

which is sub-unitary and in general has non-orthogonal eigenvectors. Following from eq. (3.9), the input-output relations for the cavity round trip can be derived as

$$\hat{a}_{1,\text{out}} = t t_1 \hat{a}_{1,\text{in}} + r t_1 \hat{a}_{2,\text{in}} + r_1 \hat{a}_{1,s}, \quad (3.10)$$

$$\hat{a}_{2,\text{out}} = t t_2 \hat{a}_{2,\text{in}} - r t_2 \hat{a}_{1,\text{in}} + r_2 \hat{a}_{2,s}, \quad (3.11)$$

where we have introduced the spontaneous emission noise contributions  $\hat{a}_{1,s}$  and  $\hat{a}_{2,s}$  to preserve unitarity. Under the assumption that after one round trip  $\hat{a}_2$  is completely fed back onto itself (i.e.,  $\hat{a}_{2,\text{out}} \rightarrow \hat{a}_{2,\text{in}}$ ), it is straightforward to calculate the factor by which the noise acting on  $\hat{a}_1$  is enhanced as compared to the noise present in eq. (3.10) alone, which is given by

$$K_1 = 1 + \frac{r^2 t_1^2 r_2^2}{r_1^2 (1 - t t_2)^2}. \quad (3.12)$$

This excess noise factor corresponds to the well-known Petermann factor [63] and results from the non-orthogonality of the eigenmodes of eq. (3.9). Analogously, the noise enhancement factor for  $\hat{a}_2$  is found to be

$$K_2 = 1 + \frac{r^2 r_1^2 t_2^2}{r_2^2 (1 - t t_1)^2}. \quad (3.13)$$

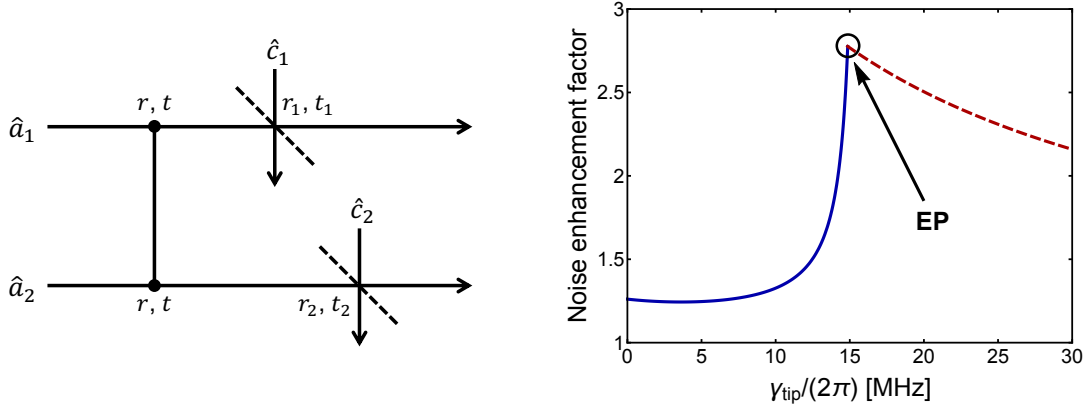


**Figure 3.8:** Simplified model for the linewidth enhancement due to the non-orthogonality of the optical modes. The two optical modes  $\hat{a}_1$  and  $\hat{a}_2$  are assumed to be perfectly coupled without coupling losses, which is characterized by the reflection and transmission coefficients  $r$  and  $t$ . Furthermore, each of the two modes is coupled to a corresponding loss mode denoted by  $\hat{c}_1$  and  $\hat{c}_2$ , respectively. This coupling is ensured via partially transparent mirrors (beam splitters) with reflection coefficients  $r_1$  and  $r_2$  and transmission coefficients  $t_1$  and  $t_2$ , respectively. As shown in the plot, this simplified setup gives rise to a significant linewidth broadening in the vicinity of the EP. The blue solid curve represents the result in the regime before the EP, whereas the red dashed curve corresponds to the regime after the EP.

By applying the above formalism to the isolated optical modes in our system—without optomechanical interaction as described by eqs. (2.28) and (2.29)—the optical noise enhancement factors can be written as

$$K_1 = 1 + \frac{\kappa^2 \gamma_2}{\gamma_1 (\Delta^2 + \gamma_2^2)}, \quad (3.14)$$

$$K_2 = 1 + \frac{\kappa^2 \gamma_1}{\gamma_2 (\Delta^2 + \gamma_1^2)}. \quad (3.15)$$

As implied by eq. (2.36), the excess noise of the cavity modes directly affects the noise in the supermodes. The effective optical noise enhancement factor for our system parameters from table 3.1 is shown in the right part of fig. 3.8, where a maximum can be observed at the EP, at which the eigenmodes of the system are identical. Therefore, the optical noise is clearly enhanced due to the non-orthogonality of the optical modes that is inherent with the occurrence of an EP. Since, in turn, the mechanical mode in our phonon laser is driven by these noisy optical supermodes, this increase of the optical noise power is then transferred to the phonon mode through the optomechanical interaction mechanism. Together with an EP-enhanced optomechanical coupling strength (see appendix A.2), this phenomenon leads to a significant phonon laser linewidth broadening in the vicinity of the EP, in good agreement with the experimental observations (cf. fig. 3.7c).



# Chapter 4

## Coherent perfect absorption

### 4.1 Time-reversed lasing

The invention of the laser laid the foundation for an overwhelming technological advancement during the past decades. Nowadays, countless applications rely on the generation of highly coherent signals. However, in many cases, the opposite effect is desired, namely the absorption of such a signal. While loss and absorption are often considered to be detrimental, several technologies are based on efficient absorption of electromagnetic waves such as mobile phone antennas, signal detectors, or microwave ovens. Obviously, the ultimate limit for the absorption efficiency is complete absorption (i.e., 100%), which is, however, unattainable in most cases because usually a certain part of the impinging energy flux is reflected or transmitted instead of being absorbed. In 2010, a team of scientists from *Yale University* could show that a coherent signal can be completely absorbed by a suitable system if both the frequency and the wavefront of the incoming radiation are precisely tuned [70]. This effect is referred to as *coherent perfect absorption*. The operating principle of such a *coherent perfect absorber* (CPA) is based on a combination of absorption and interference, which is schematically illustrated in [fig. 4.1](#). In this simplified picture, a CPA consists of a cavity of two partially reflective mirrors with an absorbing medium in between. A coherent signal is impinging on this system from both sides, where part of the incoming radiation is reflected from the mirrors while another part is transmitted after traveling back and forth through the lossy material inside the cavity. Under certain conditions, it can be achieved that the reflected and transmitted contributions of the outgoing waves are canceled out by each other through destructive interference such that the entire incoming energy is dissipated in the absorbing medium, where it is converted into heat, electricity, or other forms of energy. A comparison of this mechanism with the simple laser resonator from [fig. 2.3a](#) indicates that coherent perfect absorption corresponds to the time-reversed process of lasing at threshold. Because of this analogy, a CPA is also known as *anti-laser*.

Mathematically, a CPA can be explained with the help of the scattering matrix (or *S*-matrix) [69], which describes the scattering properties of a linear system. In particular, the *S*-matrix contains all necessary information to calculate the output for any given input according to the relation

$$\mathbf{u}_{\text{out}} = S \mathbf{u}_{\text{in}} . \quad (4.1)$$

In Hermitian systems, the energy flux is conserved, which implies that the scattering

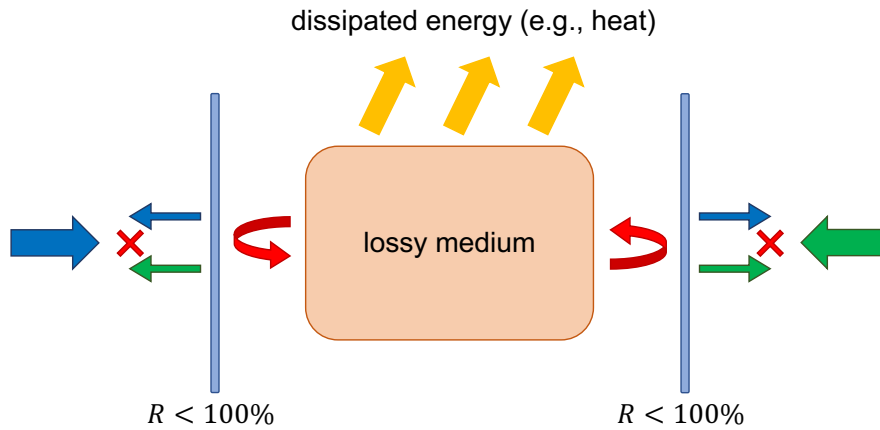


**Figure 4.1:** Basic realization of coherent perfect absorption. The frequency and the relative phase of the input waves from the left (blue) and from the right (green) are precisely tuned such that the reflected and transmitted parts are canceled out by destructive interference and all incoming energy is dissipated in the absorbing medium.

matrix is unitary, i.e.,  $S^\dagger S = \mathbb{1}$ . Consequently, the  $S$ -matrix eigenvalues are of the form  $\lambda = e^{i\phi}$  with  $\phi \in \mathbb{R}$  and thus  $|\lambda| = 1$ . Apart from the geometry and the material composition of the system, the  $S$ -matrix depends on the frequency of the incoming signal. While being a real quantity in the physical reality, the signal frequency can be extended into the complex domain in the context of a purely mathematical treatment. As it turns out, the scattering matrix of an arbitrary system features a set of poles and zeros in the complex plane of the frequency  $\nu$  or equivalently the complex wavenumber  $k = 2\pi\nu/c$ , where the poles are generally located in the lower half-plane ( $\text{Im}(\nu) < 0$ ) and the zeros are located in the upper half-plane ( $\text{Im}(\nu) > 0$ ). The poles correspond to diverging eigenvalues of the scattering matrix, whereas the zeros correspond to vanishing eigenvalues. In the absence of gain or loss, the poles and zeros are symmetrically distributed around the real axis in the complex  $\nu$ -plane and occur as complex conjugated pairs  $\nu_j^{(\pm)} = \nu_{R,j} \pm i\nu_{I,j}$ , as it is exemplarily shown in [fig. 4.2a](#). Introducing gain into the system shifts the poles and zeros upwards in the complex frequency plane. If the gain becomes large enough so that one of the poles reaches the real axis, the system starts lasing at the frequency where the pole hits the real axis (see [fig. 4.2b](#)). When the gain is further increased, the pole is kept at the real axis due to nonlinear saturation effects. However, it is possible that with increasing gain multiple poles reach the real axis at different points, which gives rise to a multimode laser. On the other hand, adding loss to the system lets the poles and zeros move downwards in the complex frequency plane. For specific amounts of introduced loss, it is possible that individual zeros can hit the real axis, which enables the system to act as a CPA or anti-laser (see [fig. 4.2c](#)). As opposed to a laser, a CPA remains always in the linear regime such that zeros can also cross the real axis and dip down into the lower half-plane when the loss is increased above the critical value.

Overall, [fig. 4.2](#) emphasizes again the time-reversal correspondence of a laser and an anti-laser. However, this analogy is valid only for a laser operating exactly at its



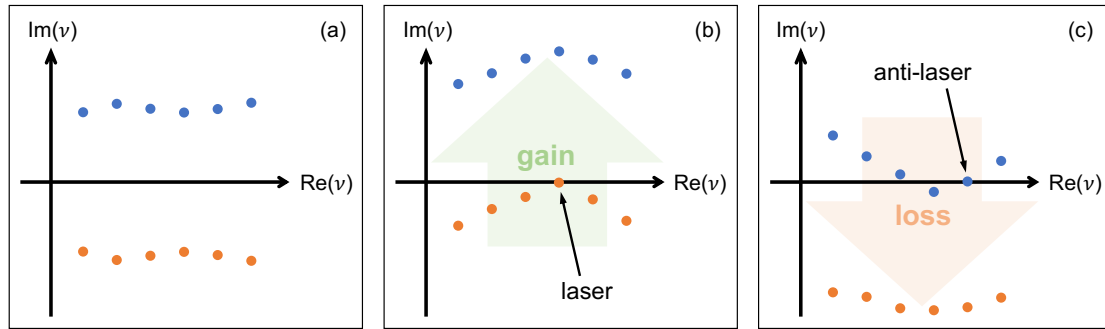


**Figure 4.2:**  $S$ -matrix poles and zeros for a Hermitian system (a), a laser (b), and an anti-laser (c). For a Hermitian system, the poles (orange) and zeros (blue) of the scattering matrix are located symmetrically around the real axis in the complex frequency plane. Adding gain to the system shifts the poles and zeros upwards in the complex  $\nu$ -plane, where lasing occurs as soon as one of the poles reaches the real axis. On the contrary, introducing loss to the system lets the poles and zeros move downwards in the complex  $\nu$ -plane, where anti-lasing or coherent perfect absorption can be realized when one of the zeros hits the real axis. While in the case of a laser nonlinear saturation effects keep the poles at the real axis when the pump power is increased above threshold, there are no such effects in an anti-laser such that zeros can also dip into the lower half-plane when the loss is increased beyond the critical value.

first threshold, where the system can still be described by the linear scattering matrix. Correspondingly, coherent perfect absorption works only if the exact right amount of loss is introduced into the system. Besides that, the proper signal frequency is defined by the position at which the  $S$ -matrix zero crosses the real frequency axis and the signal wavefront must match the eigenvector corresponding to the zero-eigenvalue in order to realize a CPA.

As described in the original publication on coherent perfect absorption [70], one possible realization of a CPA is given by a silicon wafer onto which two normally incident laser beams are directed on opposite sides. Indeed, a similar setup was experimentally demonstrated already in 2011 [71]. To illustrate the functionality of this approach, we want to perform a theoretical analysis of such a system. The propagation of electromagnetic waves is described by the wave equation (see [appendix B.1](#) for more details), which is a partial differential equation involving both spatial and temporal derivatives. Since coherent perfect absorption works only for signals with well-defined frequencies in the steady state, the relevant physics can be described with the Helmholtz equation, whose derivation can be found in [appendix B.2](#). For the simple case of a planar dielectric slab under normal incidence of a coherent laser beam, the problem can be reduced to one spatial dimension such that the Helmholtz equation for the scalar electric field  $E(x)$  can be written as

$$\left[ \frac{\partial^2}{\partial x^2} + n^2(x)k^2 \right] E(x) = 0, \quad (4.2)$$

where  $n(x)$  represents the spatially dependent refractive index and  $k = 2\pi/\lambda$  is the wavenumber. Under the assumption of a dielectric medium of width  $L$  surrounded

by vacuum, the refractive index can be considered as a piecewise constant function consisting of three different regions with  $n(x) \equiv n_1 = 1$  for  $x < -L/2$ ,  $n(x) \equiv n_2 := n$  for  $-L/2 \leq x \leq L/2$ , and  $n(x) \equiv n_3 = 1$  again for  $x > L/2$ . The absorption in the system can be modeled by a complex refractive index  $n = n_R + in_I$ , where the imaginary part  $n_I$  is also referred to as extinction coefficient. For constant refractive index, the Helmholtz equation can be solved analytically and the solution is given by a superposition of forward and backward traveling plane waves. For the three regions in the aforementioned system we therefore have

$$E_1(x) = A_1 e^{ikx} + B_1 e^{-ikx}, \quad (4.3)$$

$$E_2(x) = A_2 e^{inkx} + B_2 e^{-inkx}, \quad (4.4)$$

$$E_3(x) = A_3 e^{ikx} + B_3 e^{-ikx}, \quad (4.5)$$

where in our coordinate convention, terms proportional to  $e^{in(x)kx}$  correspond to wave contributions traveling from left to right, and vice versa, terms proportional to  $e^{-in(x)kx}$  represent waves traveling from right to left. By demanding that both the field and also its first derivative must be continuous at the region borders, the following boundary conditions can be derived:

$$E_1(-L/2) = E_2(-L/2), \quad (4.6)$$

$$E_1'(-L/2) = E_2'(-L/2), \quad (4.7)$$

$$E_2(L/2) = E_3(L/2), \quad (4.8)$$

$$E_2'(L/2) = E_3'(L/2). \quad (4.9)$$

Equations (4.6) to (4.9) represent a set of four linear equations for the field amplitudes  $A_i$  and  $B_i$ . If only two of them are given—for example the incoming components  $A_1$  and  $B_3$ —all other coefficients (in particular also the outgoing components  $A_3$  and  $B_1$ ) can be straightforwardly calculated. From that result, also the corresponding scattering matrix can be obtained. Because of the mirror symmetry of the system, the eigenmodes are parity eigenstates, which gives rise to a symmetric ( $A_1 = B_3$ ) and an anti-symmetric ( $A_1 = -B_3$ ) eigenmode. With the help of the corresponding eigenvalues

$$\lambda_{\pm} = \frac{[(1+n)e^{inkL} \pm (1-n)]e^{-ikL}}{(1-n)e^{inkL} \pm (1+n)}, \quad (4.10)$$

the positions of the zeros in the complex frequency plane can be determined and the results are shown in [fig. 4.3a](#). As a consequence of the intrinsic loss in the medium, the zeros (as well as the poles) are clearly shifted downwards in the complex frequency plane as compared to their original positions for the case of a lossless material with  $n = 3$ . For the case under consideration, we have chosen  $n = 3 + 0.0826i$ , which represents an optimized value in the sense that one of the zeros hits the real axis. Consequently, a CPA can be realized at this frequency, which is illustrated in [fig. 4.3b](#). As can be seen, the incoming signal is completely absorbed by the medium such that the outgoing signal vanishes.

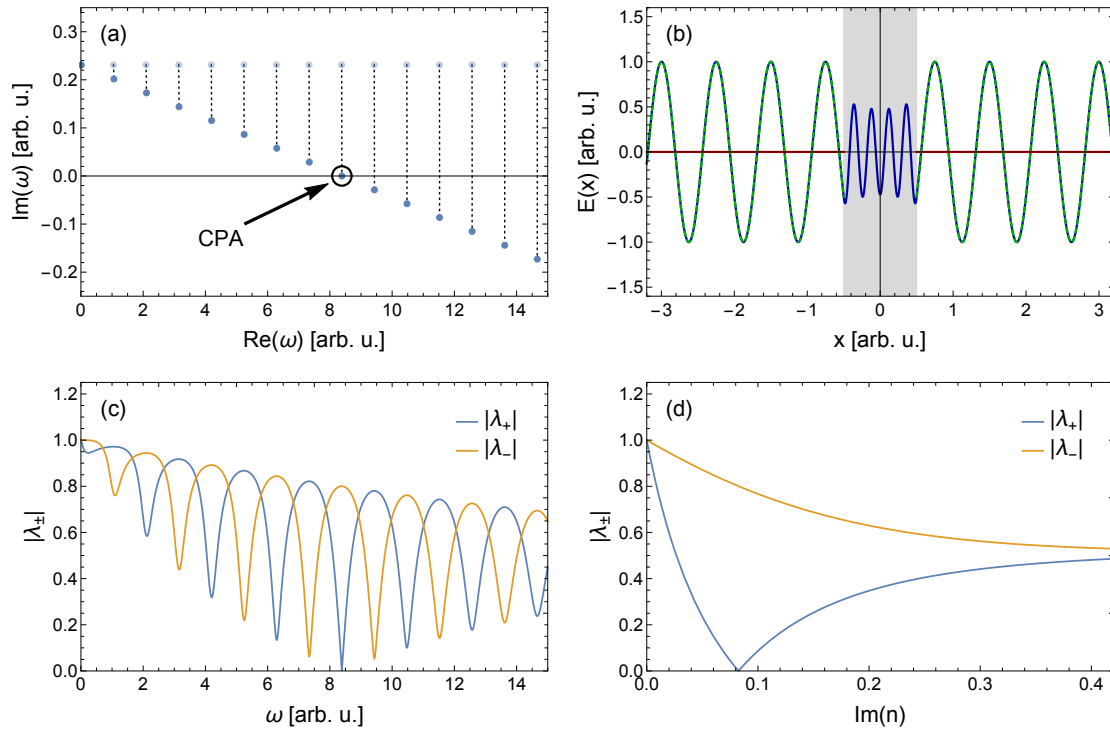


**Figure 4.3:** Coherent perfect absorption in a planar dielectric medium (refractive index  $n = 3 + 0.0826i$ ). (a)  $S$ -matrix zeros in the complex frequency plane. Due to the intrinsic absorption of the material, the zeros are shifted downwards in the complex frequency plane such that a CPA occurs at the real frequency  $\omega = 8.384$  (arbitrary units). The original positions of the zeros correspond to the case with  $n = 3$ . (b) Field of the corresponding CPA state: incoming field (green dashed), outgoing field (red), and total field (blue). The gray shaded area represents the absorbing medium. (c)  $S$ -matrix eigenvalues corresponding to the symmetric ( $\lambda_{+}$ ) and anti-symmetric ( $\lambda_{-}$ ) eigenvectors as a function of the signal frequency for optimized extinction coefficient  $n_I = 0.0826$ . (d)  $S$ -matrix eigenvalues as a function of the extinction coefficient  $n_I$  for optimized signal frequency  $\omega = 8.384$  (arbitrary units).

The absorption efficiency of a CPA strongly depends on the proper adjustment of the system parameters and can be quantified by the absolute value of the minimal  $S$ -matrix eigenvalue. In [fig. 4.3c](#), we present the dependence of the eigenvalues on the frequency of the incoming waves, whereas [fig. 4.3d](#) depicts the eigenvalues as a function of the imaginary part of the refractive index. A comparison with [fig. 4.3a](#) confirms that the absorption efficiency first increases when more loss is introduced into the system until a critical value is reached where the  $S$ -matrix zero crosses the real frequency axis and the corresponding eigenvalue vanishes. However, a further increase of the loss causes the zeros to dip down into the lower half-plane and the absorption efficiency decreases again. Additionally, it turns out that already slight deviations from the optimal frequency value lead to a significant reduction of the absorption efficiency. Furthermore, the relative phase between the left and right incoming waves must be precisely tuned in order to match the CPA eigenstate that belongs to the zero on the real frequency axis. If this

phase relation is changed, the CPA effect breaks down and a non-vanishing outgoing signal occurs.

## 4.2 Random anti-lasing<sup>7</sup>

Since the first theoretical discussion of coherent perfect absorption [70], various experimental CPA realizations have been reported [71, 74, 77, 81, 83–85, 87, 95, 112]. These setups have in common that they rely on a special geometric architecture or work only under very specific conditions. In order to achieve coherent perfect absorption in actual “real-life” applications, however, it is necessary to implement this effect also in complex environments. In this section, we consider the generalization of anti-lasing to the case of a disordered medium in which the incoming waves are subject to chaotic scattering before they are completely absorbed by an embedded antenna. Due to the fact that coherent perfect absorption in disordered media corresponds to the time-reversed process of random lasing (cf. fig. 2.3b), such a device can be called a *random anti-laser*.

### 4.2.1 Experimental realization

Due to complex scattering, the output field of a random laser usually features a complicated wave pattern. Consequently, the time-reversal of random lasing requires a very challenging level of control over all necessary degrees of freedom. Although considerable progress in the field of wavefront shaping has been made recently [69, 144, 145], the realization of a random anti-laser remained out of reach so far. This is because not only the phase and amplitude of all relevant pixels that determine the complex speckle pattern of such a random anti-laser mode must be properly adjusted, but also the radiation frequency and the absorption strength of the system have to be precisely tuned to match one of the discrete pairs of values at which a CPA can be realized. Away from these isolated CPA points, reaching perfect absorption is impossible in principle.

To tackle this problem, we designed a proof-of-principle experiment in the form of an innovative microwave setup which is based on an existing experimental platform [146]. Our system—as pictured in fig. 4.4—essentially consists of a rectangular aluminum waveguide with 10 cm inner width ( $y$ -direction), 8 mm inner height ( $z$ -direction), and a total length of 238 cm ( $x$ -direction). The waveguide supports a finite number of transverse modes, which in turn determines the required number of controllable degrees of freedom in the incoming radiation field. The central scattering region (length 60 cm) of the waveguide contains a disordered medium that consists of a set of randomly placed cylindrical Teflon scatterers (refractive index  $n = 1.44$ ). For our experiments, two different sizes with diameters 5.1 mm (small) and 22 mm (large) are used. All scatterers

<sup>7</sup> The idea for this project was conceived by Stefan Rotter and the experimental setup was designed by Julian Böhm and Ulrich Kuhl. Measurements and data evaluation were carried out by myself under the supervision of Ulrich Kuhl. The numerical simulations were performed by Matthias Kühmayer with theoretical input from Andre Brandstötter and Philipp Ambichl. Part of the results and figures are taken from our joint publication [91] or have been provided by Matthias Kühmayer in private communication.

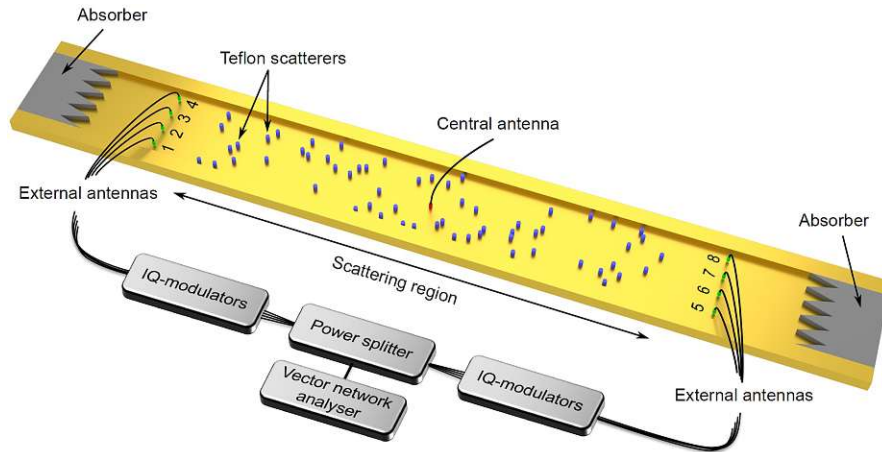


**Figure 4.4:** Experimental setup of the random anti-laser. Microwaves of a well-defined frequency are generated by a vector network analyzer and equally distributed through a power splitter to eight in-phase/quadrature (IQ) modulators, where the amplitudes and relative phases of the signals can be independently tuned. These signals are injected into an aluminium waveguide via eight external antennas (four on each side, numbered as indicated). Absorbers are placed at the waveguide ends to avoid back-reflection of the injected and transmitted waves. The central scattering region of the waveguide contains a disordered medium consisting of a set of randomly placed Teflon scatterers. Localized absorption is introduced to the system by placing a monopole antenna with a  $50\ \Omega$  terminating resistance in the middle of the disordered region (central antenna). The scattering matrix of the system is determined by measuring the field in the space between the scattering region and the external antennas using a movable antenna that can dip into the waveguide through a grid of holes in the top plate (not shown). The distances from the external antennas to the absorbers and to the scattering region are not to scale.

have a height of 8 mm and are thus filling the whole waveguide height. In the middle of the scattering region, localized loss can be introduced by inserting a monopole antenna with a  $50\ \Omega$  terminating resistance attached through the top plate of the waveguide. This absorbing antenna is placed at the center of the system regarding the  $x$ -direction and slightly out of the center ( $\pm 9$  mm) regarding the  $y$ -direction. The coupling of the central antenna and therefore its absorption strength can be varied *in situ* by changing the length that it ranges into the waveguide.

Both as a signal source and also for the measurements, a vector network analyzer (VNA) is used. At an operating frequency between 6 GHz and 7.5 GHz, the waveguide supports four transverse modes, requiring four antennas on each side (left and right) to fully control the wavefront of the injected signal. Therefore, the microwaves generated by the VNA are equally distributed by a power splitter to eight in-phase/quadrature (IQ) modulators, where the relative phases and amplitudes of the injected microwaves are controlled. These signals are then transferred to eight external antennas reaching about 3 mm into the waveguide (weak coupling), four on each side. Both ends of the waveguide are equipped with absorbers to avoid back-reflection of the injected and

transmitted signals. The field inside the waveguide can be measured with the help of a movable antenna that can dip into the waveguide through a grid of holes (spacing of 5 mm from center to center) in the top plate of the waveguide. Reaching about 4 mm into the waveguide, this probe antenna is also only weakly coupled to the system and thus has merely a minor influence on the field that it measures. Optionally, one port of the VNA can be connected to the central antenna to measure the transmission of an input state injected by the external antennas into the central antenna. In addition, this configuration can be used to inject microwaves at the central antenna.

In order to inject a specific input state into the system, the amplitudes and phases at each of the external antennas have to be properly adjusted by the IQ modulators, which requires the knowledge of the relation between the IQ modulator settings and the resulting incoming waves. For that purpose, one can assign to each IQ modulator a basis vector in the *IQ modulator basis*, which means that the respective IQ modulator is set to full transmission and relative phase zero while all other IQ modulators are set to maximum attenuation. By measuring the field in the space between the external antennas and the scattering region, the resulting composition of the incoming modes can be determined. Since the field is a linear superposition of the incoming and outgoing modes, the measured mode coefficients  $a_{\text{meas},j}$  satisfy the following relation with the coefficients for the incoming and outgoing modes ( $a_{\text{in},j}$  and  $a_{\text{out},j}$ )

$$a_{\text{meas},j}(x) = a_{\text{in},j} e^{-ik_{x,j}x} + a_{\text{out},j} e^{ik_{x,j}x}, \quad (4.11)$$

where  $j$  is the number of the respective mode and  $k_{x,j} = \sqrt{k^2 - k_{y,j}^2}$ , in which  $k = 2\pi\nu/c$ ,  $k_{y,j} = j\pi/d$ ,  $\nu$  is the frequency of the incoming waves,  $c$  is the speed of light, and  $d$  is the width of the waveguide. Using that the transverse modes in a rectangular waveguide feature a sinusoidal shape in  $y$ -direction which is given by [147]

$$\psi_j(y) = \sin \left[ k_{y,j} (y + d/2) \right], \quad (4.12)$$

the coefficients  $a_{\text{meas},j}(x)$  can be determined by means of a discrete sine transformation of the complex measured field. By evaluating eq. (4.11) on both sides of the waveguide for two adjacent  $x$ -positions and for all IQ modulator basis vectors, the coefficients  $a_{\text{in},j}$  of the incoming modes can be calculated. A basis transformation from the *IQ modulator basis* to the *mode basis* then yields the coefficients  $c_{mj}$  by which the signals at the IQ modulators (numbered by  $m$ ) have to be multiplied to get the desired mode  $j$ . As a test of this procedure, the four possible transverse modes were injected into the empty waveguide (i.e., without absorbing antenna or scatterers). The resulting microwave field has been measured along the waveguide width ( $y$ -direction) at a distance of about 20 cm away from the external antennas and the results are presented in fig. 4.5. Apart from small deviations stemming from unavoidable experimental imperfections, the curves clearly show the expected mode shapes (fig. 4.5a) with correlation values between 99.7% and 99.9%. Moreover, the analysis of the measured signals in the mode domain (fig. 4.5b) yields the expected mode composition and proves the functionality of our injection method.

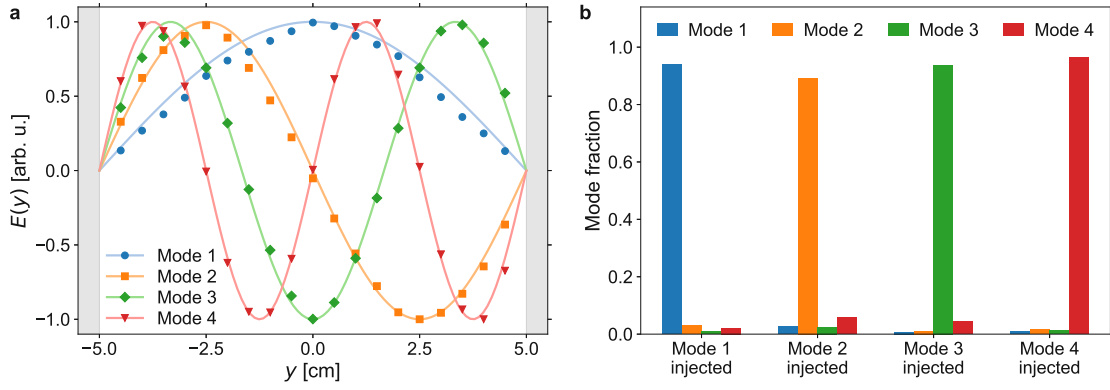


**Figure 4.5:** Injection accuracy analysis of specific states. (a) Field of the four possible transverse modes injected into the empty waveguide (without absorbing antenna or any other obstacle). The solid curves describe the expected mode shape, whereas the markers denote the normalized field values measured over the waveguide width ( $y$ -direction). The gray shaded areas represent the waveguide walls. (b) Analysis of the injected signals from (a) in the mode domain, where the bars illustrate the fraction of the respective mode in the incoming signal.

With the availability of the incoming and outgoing mode coefficients, we are further in the position to calculate the scattering matrix of the system, which satisfies the relation

$$\mathbf{a}_{\text{out}} = S \mathbf{a}_{\text{in}}. \quad (4.13)$$

Since eq. (4.13) comprises  $N$  linearly independent equations for the  $N^2$  elements of the  $S$ -matrix, where  $N$  is the total number of modes considered (eight in our experiment), one needs to have at least  $N$  linearly independent sets of the incoming and outgoing mode coefficients  $\mathbf{a}_{\text{in}}$  and  $\mathbf{a}_{\text{out}}$  to obtain  $N^2$  coupled equations for the  $S$ -matrix elements. In fact, the same measurement data that is used to calculate the IQ modulator settings can be taken to explicitly determine the  $S$ -matrix at a given signal frequency.

The ability to measure the scattering matrix in the far-field while both the signal frequency and the absorption strength can be precisely tuned makes our system an ideal platform to realize coherent perfect absorption in a disordered medium. A crucial property of a CPA is that the entire incoming signal is absorbed such that the outgoing signal vanishes, i.e.,  $\mathbf{a}_{\text{out}} = S \mathbf{a}_{\text{in}} = 0$ . This means that a CPA state  $\mathbf{a}_{\text{CPA}}$  is an eigenstate of the scattering matrix with an eigenvalue of zero ( $\lambda_{\text{CPA}} = 0$ ). Based on this analysis, we deduce the following expedient and robust approach to realize a random anti-laser with our experimental setup: the  $S$ -matrix of the system is measured in a frequency interval broad enough to contain many  $S$ -matrix zeros and for a number of loss values of the central antenna that are strong enough to drag some of the zeros down to the real frequency axis. Subsequently, the eigenvalues of these different scattering matrices are evaluated and those parameter configurations for which the absolute value of the smallest  $S$ -matrix eigenvalue approaches zero can be identified. The CPA eigenstate corresponding to this minimal  $S$ -matrix eigenvalue is then injected into the system in

order to determine its properties (in particular the degree of absorption associated with it). This approach is both scalable in terms of the number of pixels and readily transferable to other experimental platforms. Moreover, similar setups turn out to be very suitable for other applications, e.g., in the field of optical micromanipulation [148].

## 4.2.2 Experimental and numerical results

### Coherent perfect absorption in disordered media

To test the functionality of our method, we apply it to a disordered medium consisting of 60 small cylindrical Teflon scatterers (radius 2.55 mm) as shown in fig. 4.4, for which we measure the scattering matrix in the frequency range from 6 GHz to 7.5 GHz and for various lengths of the central antenna. Data close to the mode openings (at 6 GHz and 7.5 GHz) are, however, not taken into account to avoid the influence of evanescent waveguide modes, which restricts us to the spectral interval between 6.55 GHz and 7.35 GHz. An investigation of the minimal  $S$ -matrix eigenvalue  $\lambda_{\min}$  reveals a pronounced dip around the frequency of 7.1 GHz for an absorbing antenna that extends 7 mm into the waveguide (see fig. 4.6a). As expected, the outgoing power (divided by the incoming power) of the eigenstate corresponding to this eigenvalue minimum features a similar dip in the same frequency range, where we achieve more than 99.78% absorption of the injected power ( $P_{\text{out}}/P_{\text{in}} < 2.12 \times 10^{-3}$ ).

In fig. 4.6, we investigate the sensitivity of the CPA state with respect to deviations from optimal parameter values. Firstly, one can see (in accordance with the findings from section 4.1) that perfect absorption occurs only at the CPA frequency  $\nu_{\text{CPA}}$ , where the  $S$ -matrix zero crosses the real axis. The minima of the smallest  $S$ -matrix eigenvalue and of the ratio between the outgoing and incoming power of the injected CPA state are slightly shifted against each other. This effect is a result of experimental imperfections such as, e.g., the finite step size of the IQ modulator settings, which limits the injection accuracy of specific states. Secondly, our results confirm that also the exact right amount of loss must be introduced into the system. The loss in our system can be controlled by varying the coupling strength of the central antenna, which is done by changing the length that it extends into the waveguide. In fact, it turns out that not only for smaller but also for larger coupling strength (corresponding to more loss) the absorption efficiency is substantially diminished as compared to the optimal antenna length of 7 mm (see right panels in fig. 4.6a). Finally, we investigate the sensitivity of the absorption efficiency to deviations from the optimal wavefront of the injected CPA state in fig. 4.6b. For this purpose, we check what happens if either the amplitude or the phase of just one of the eight external antennas is detuned away from the configuration of the CPA state while all other parameters remain at the optimized values. In both cases, the minimum of the ratio between outgoing and incoming power is considerably increased by factors of up to approximately  $10^3$ , which emphasizes how strongly the absorption in the system is controlled interferometrically rather than by the mere presence of the absorbing antenna alone.



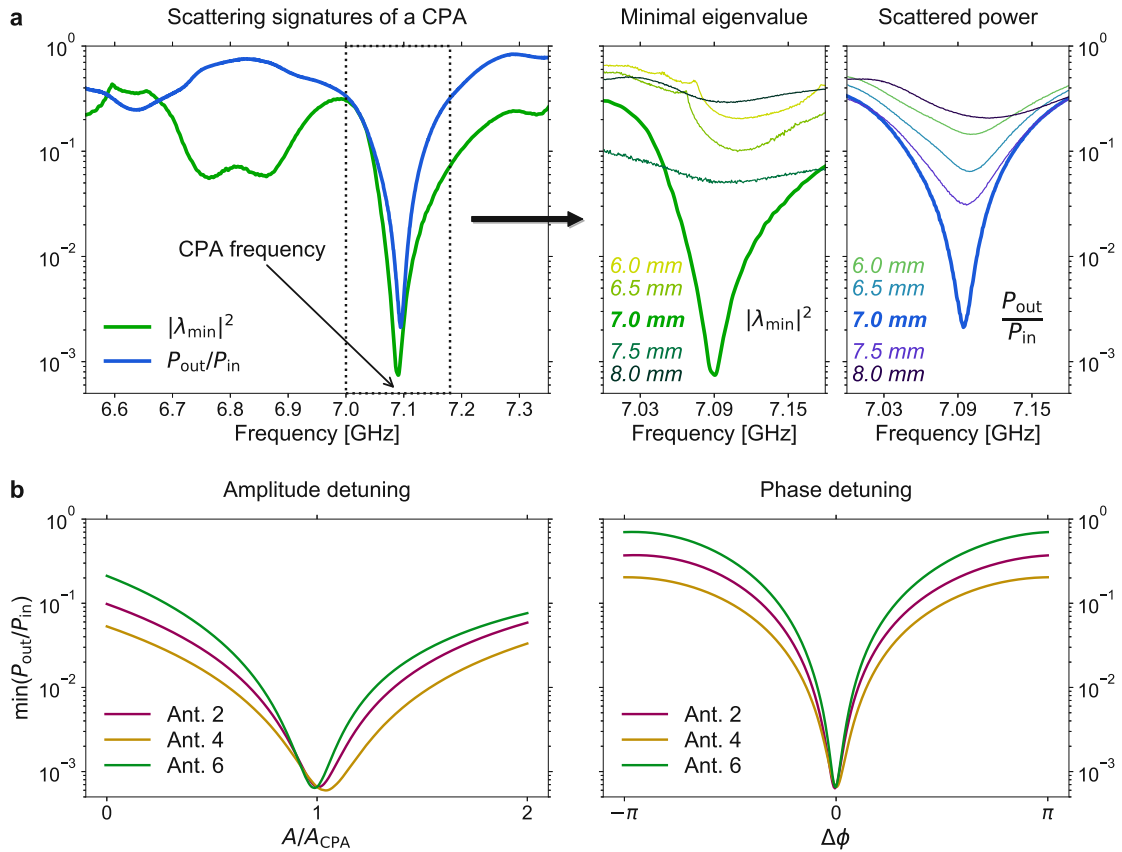


**Figure 4.6:** Absorption analysis of a CPA state for a disordered medium with 60 small scatterers. (a) Squared absolute value of the minimal  $S$ -matrix eigenvalue  $|\lambda_{\min}|^2$  together with the ratio between the outgoing and incoming power  $P_{\text{out}}/P_{\text{in}}$  for the CPA state corresponding to the eigenvalue minimum at the CPA frequency of about 7.1 GHz as a function of the signal frequency. The panels on the right provide a detailed view around the CPA frequency of the minimal  $S$ -matrix eigenvalue  $|\lambda_{\min}|^2$  as well as of the ratio  $P_{\text{out}}/P_{\text{in}}$  for the injected CPA state, each determined for different lengths of the central antenna. (b) Sensitivity of the CPA minimum to detunings in individual IQ modulators, where either the amplitude or the relative phase at an exemplary input antenna are changed while all other antennas remain as required for the CPA state (amplitude  $A_{\text{CPA}}$  and phase  $\phi_{\text{CPA}}$ ). The results presented in (b) were generated by linear superposition of the data from the  $S$ -matrix measurement, whereas the blue curve in (a) represents a direct measurement of the injected CPA state.

With a diameter of 5.1 mm, the small scatterers are much smaller than the operating wavelength of  $\lambda \approx 43$  mm. Therefore, the scattering strength of the small scatterers is relatively weak. To demonstrate that our approach is generally applicable also for more strongly scattering configurations, we implement a disordered medium consisting of a mixture of 28 small and 32 large dielectric disks with diameters of 5.1 mm and 22 mm, respectively. Also in this case, we can readily find a pronounced CPA state with a ratio between outgoing and incoming power of  $P_{\text{out}}/P_{\text{in}} < 2.13 \times 10^{-3}$  (i.e., again more than 99.78% absorption) at the CPA frequency of 6.9 GHz. The scattering characteristics are

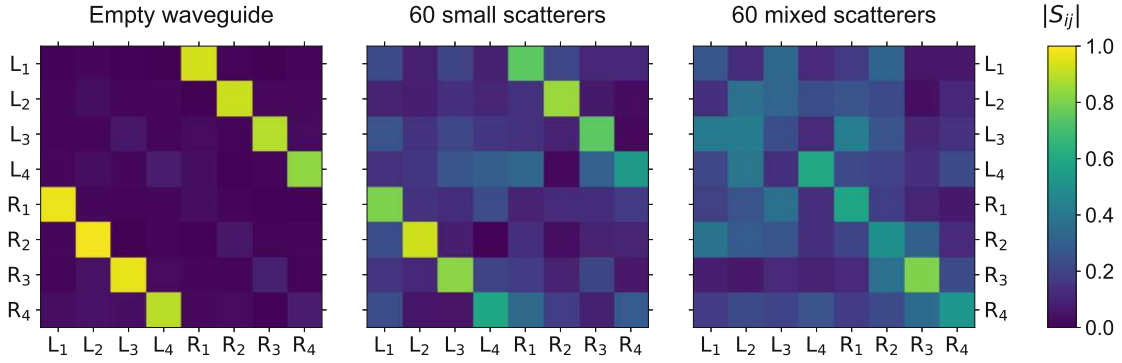


**Figure 4.7:** Typical scattering matrices for different scatterer configurations: empty waveguide (left panel), weakly scattering system of 60 small scatterers (middle panel), and strongly scattering system with 60 scatterers of mixed sizes (right panel). The labels denote the left ( $L_m$ ) and the right ( $R_m$ ) side of the waveguide, where the subscript represents the respective mode number.

described by the  $S$ -matrix, which can be written as

$$S = \begin{pmatrix} R_L & T_R \\ T_L & R_R \end{pmatrix}, \quad (4.14)$$

where  $T_L$  and  $T_R$  are the transmission sub-matrices and  $R_L$  and  $R_R$  are the reflection sub-matrices, respectively, with regard to the four modes on the left and right side of the waveguide, indicated by the subscripts L and R. To visualize the scattering strength of the configurations with only small scatterers and with mixed-size scatterers, respectively, we investigate the corresponding scattering matrices (measured at the respective CPA frequencies of 7.1 GHz and 6.9 GHz) and compare them to the  $S$ -matrix of the empty waveguide (measured at 7.1 GHz) in [fig. 4.7](#). For the empty waveguide, we find that the transmission sub-matrices are diagonal while all elements of the reflection sub-matrices are strongly reduced. This is the expected result for an empty waveguide featuring only a length-dependent scattering phase shift together with a small attenuation due to absorption in the metallic waveguide material. Minor deviations from this ideal picture can be attributed to experimental imperfections such as the backscattering at the weakly coupled external antennas. The situation changes when scattering objects are embedded into the system and with increasing scattering strength, which is influenced by the number and sizes of the scatterers, the transmission sub-matrices become more and more off-diagonal. For the configuration with 60 small scatterers, the  $S$ -matrix gets occupied all over its  $8 \times 8$  entries, albeit the diagonal transmission elements remain more pronounced than the other  $S$ -matrix elements. For the strong scattering configuration with 60 mixed-size scatterers, the  $S$ -matrix is more uniformly occupied.

The degree of the scattering strength also influences the interference pattern of the microwave field inside the scattering region. Since a measurement of the electric field over the whole waveguide is very time-consuming and the field in the direct vicinity of the central antenna is inaccessible in our experimental setup, we reconstruct the

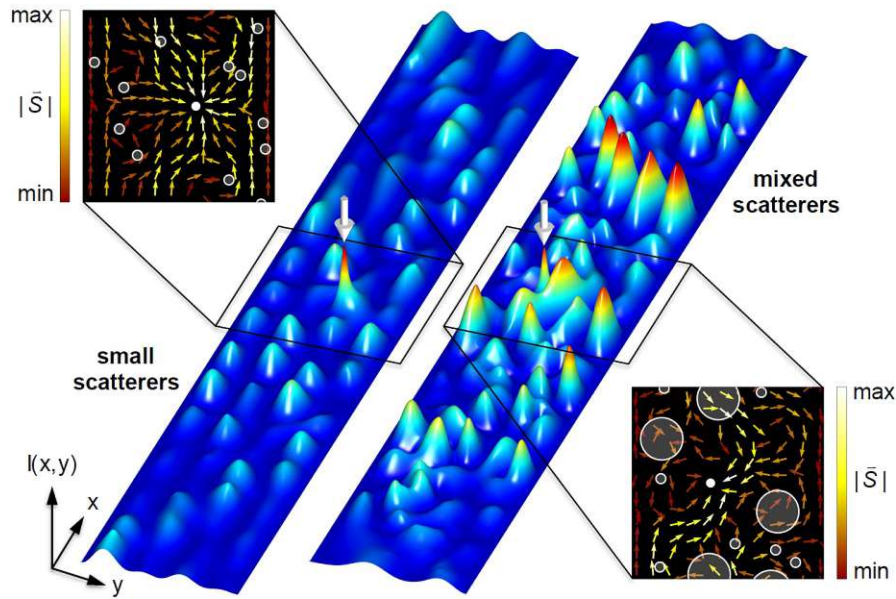


**Figure 4.8:** Numerical simulation of the field intensity of CPA states injected into a weakly disordered waveguide with 60 small scatterers (left) and a strongly disordered waveguide with 60 mixed-size scatterers (right). The linear color scale ranges from low (blue) to high (red) intensity and the position of the central absorbing antenna is marked by a white arrow. The insets show the Poynting vector  $\mathbf{S}$  in the vicinity of the absorbing antenna, where the scatterers are depicted as semi-transparent white circles and the antenna is represented by a filled white circle.

entire scattering geometry numerically and perform a numerical simulation of the microwave field by means of a finite element discretization on a two-dimensional mesh (see [appendix B.2](#) and ref. [149] for further information). The central antenna is modeled as an absorbing scatterer with a complex refractive index  $n_{\text{ant}} = n_{\text{R}} + in_{\text{I}}$ . To find a CPA state, we set the signal frequency to the experimentally determined CPA frequency and optimize the refractive index of the antenna scatterer such that the minimal  $S$ -matrix eigenvalue approaches zero. The results of these simulations for the weakly and strongly scattering systems that were experimentally implemented before are presented in [fig. 4.8](#). For the configuration with 60 small scatterers, we observe a relatively regular interference pattern in the microwave intensity with a pronounced intensity peak at the position of the central antenna. In the case of the configuration with 60 scatterers of mixed sizes, the interference pattern features a much more irregular character. However, there is still a sharp intensity maximum at the absorbing antenna. Obviously, a CPA state that is primarily absorbed by the central antenna features a pronounced focus spot at the central antenna to optimize the absorption efficiency. To visualize the directional energy flux, we calculate the Poynting vector in the area around the central antenna (see [appendix B.3](#) for technical details). As shown in the insets of [fig. 4.8](#), the Poynting vector has only inward-pointing components in the vicinity of the absorbing antenna.

As an experimental signature of this behavior, we measure the transmission of the

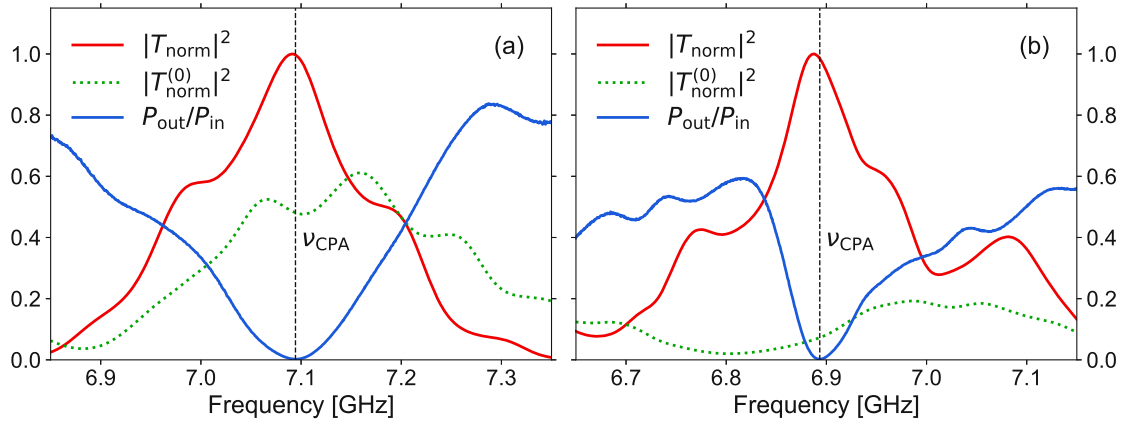


**Figure 4.9:** Transmission of the investigated CPA states from fig. 4.8 into the central antenna for configurations with 60 small scatterers (a) and 60 mixed-size scatterers (b), respectively. The plots compare the squared absolute value of the transmission  $T_{\text{norm}}$  into the absorbing antenna (normalized with respect to its maximum  $|T_{\text{max}}|$  within the measured interval) with the ratio between outgoing and incoming power  $P_{\text{out}}/P_{\text{in}}$ . As a reference, the plots also show the transmission  $T_{\text{norm}}^{(0)}$  of these CPA states into the absorbing antenna when all scatterers are removed from the waveguide, where the same normalization  $|T_{\text{max}}|$  as for  $T_{\text{norm}}$  is used. The vertical dashed line marks the CPA frequency  $\nu_{\text{CPA}}$ .

CPA states into the central antenna, which is shown in fig. 4.9. Both for the weak and for the strong scattering configuration, the transmission into the central antenna features a maximum at the CPA frequency, where the ratio between the outgoing and incoming power has its minimum. This confirms again that these CPA states are primarily absorbed by the central antenna and only weakly affected by the global loss inside the waveguide. For comparison, we also measure the transmission of the CPA states into the absorbing antenna for the case when all scatterers are removed from the waveguide (see green dotted curve in fig. 4.9). Because each CPA state is customized for the specific scatterer configuration, the removal of the disordered medium leads to a significant reduction of the transmission into the central antenna.

To study the influence of the absorbing antenna on the microwave field, we perform numerical simulations of the CPA states for both scatterer configurations with and without the absorbing scatterer in place. The results, which are depicted in fig. 4.10, show that the central antenna has a significant effect on the overall intensity and the interference pattern of the field. One can clearly observe that the removal of the absorbing scatterer causes considerably higher and differently distributed intensity maxima in the waveguide stemming from additional interference contributions of the waves that are no longer absorbed by the antenna.

Finally, to verify that the numerical simulations do in fact describe the actual experiment, we compare the simulated and measured results for the field intensity of the CPA states in the vicinity of the central antenna, which is shown in fig. 4.11. Experimentally, we measure the electric field on a grid with a spacing of 5 mm, where the close proximity around the central antenna and also the field inside the scatterers are inaccessible due

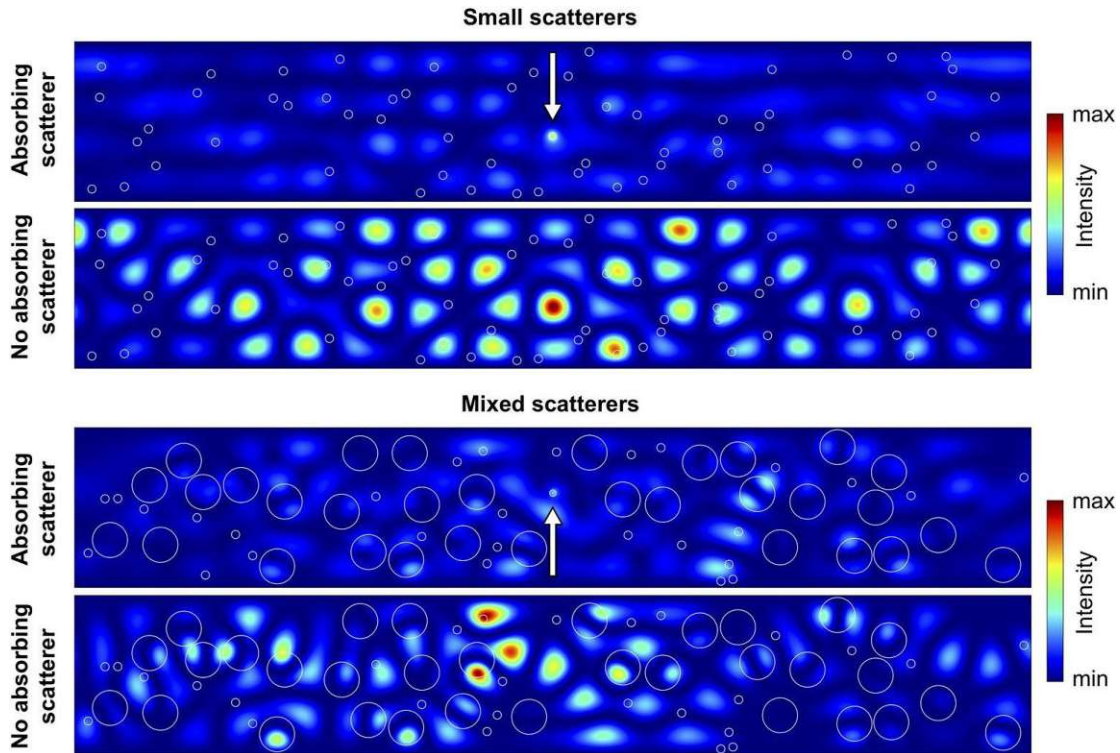


**Figure 4.10:** Simulated microwave field of the CPA states for the configurations with 60 small scatterers and 60 scatterers of mixed sizes, respectively. The plots compare the intensity distributions of the CPA states injected in the presence (top panels) or absence (bottom panels) of the absorbing scatterer (i.e., the absorbing antenna). All other parameters and the linear color scale remain unchanged. The position of the absorbing antenna is indicated by a white arrow and the white circles represent the scatterers.

to setup-specific restrictions. For a meaningful comparison, the numerical results are mapped to the same reduced  $5 \times 5 \text{ mm}^2$  grid as in the experiment. Indeed, we find a good agreement between numerical and experimental data, which is quantified by a correlation of 95.63% for the configuration with 60 small scatterers and 83.42% for the configuration with 60 scatterers of mixed sizes, respectively. Small deviations between simulated and measured data can be attributed to experimental imperfections such as a slight misplacement of the scatterers<sup>8</sup> or inevitable scattering at the external antennas as well as at the measuring antenna. Furthermore, the effect of global absorption (caused by the skin effect in the metallic waveguide and by escape through the small holes in the top plate) is neglected in our simulations. Taking also global absorption into account in the simulations (following ref. [147] based on material parameters for our aluminum waveguide), however, the intensity correlation values for the two CPA states from above

<sup>8</sup> We expect an uncertainty of about 1 mm in the experimentally realized scatterer positions as compared to the values used in the simulations. Since the strongly scattering system with mixed scatterers is more sensitive to such deviations, this also explains why the correlation value is lower here than for the case of weak scattering.

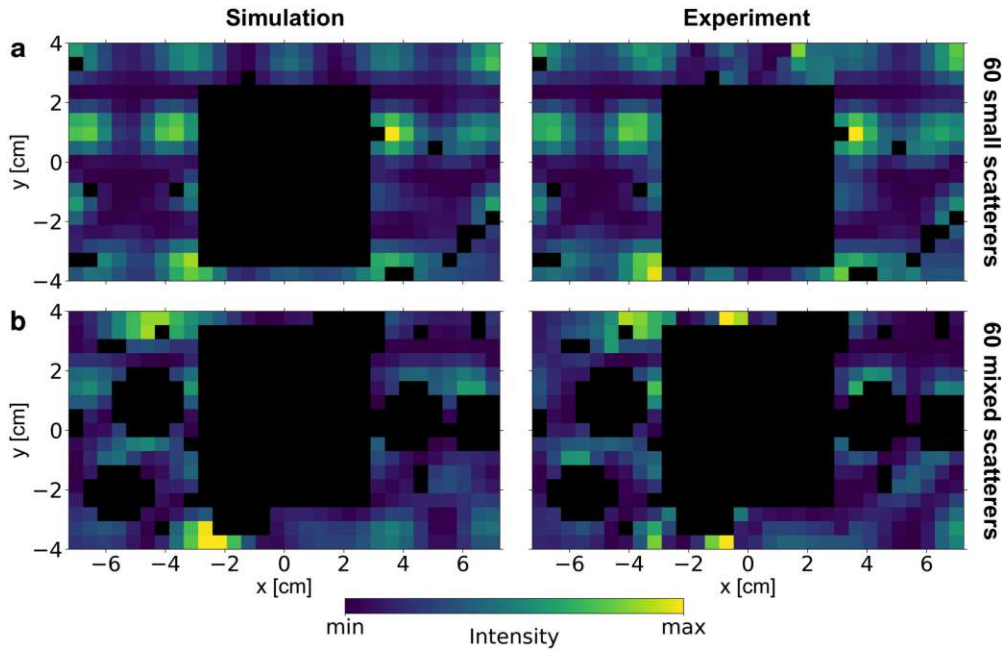


**Figure 4.11:** Comparison between the simulated and measured results for the field intensity around the central antenna of CPA states for configurations with 60 small scatterers (a) and 60 scatterers of mixed sizes (b). Since the electric field is experimentally inaccessible in the close proximity of the central antenna and inside the scatterers, these areas are colored black in the plots. While the numerical simulations have been performed on a much finer mesh, the simulated data is mapped on the same grid where also the experimental data points are available such that each pixel corresponds to an area of  $5 \times 5 \text{ mm}^2$  in the waveguide.

remain almost unchanged. Specifically, the correlation values for the configurations with 60 small and 60 mixed scatterers are then 95.57% and 83.44%, respectively. The reason why global absorption has a weak effect on the considered CPA states is because for these states the loss incurred at the central antenna is much more dominant than the weak dissipation in the waveguide.

### Time-reversal correspondence with lasing at threshold

Disregarding global absorption effects, a CPA state in our random anti-laser should be entirely absorbed by the central antenna. The time-reversed process of this mechanism would be a microwave signal that is injected at the central antenna and then leaves the waveguide through the leads without any back-reflection to its source. Therefore, it would be interesting to explore what happens if a signal is injected at the central antenna. As mentioned in [section 4.2.1](#), this can be easily realized with our setup if one port of the VNA is connected to the central antenna, which turns it from an absorber into a source. For example, in the case of the disordered medium consisting of 60 small scatterers, we would expect that at the CPA frequency of 7.1 GHz and for an antenna length of 7 mm the injected signal enters the disordered waveguide system without any back-reflection

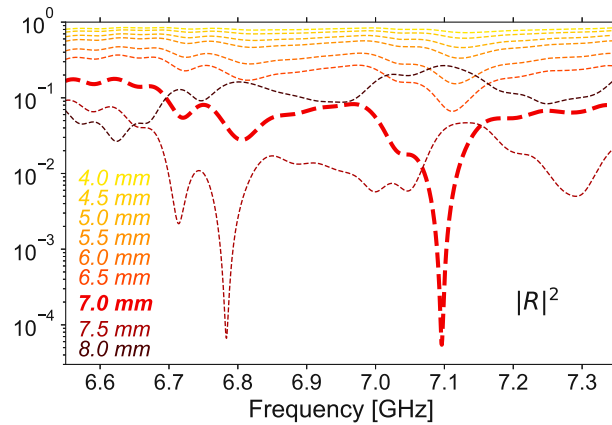


**Figure 4.12:** Reflection coefficient  $|R|^2$  for microwave injection at the central antenna as a function of the signal frequency for different antenna lengths in the disordered configuration with 60 small scatterers.

to the central antenna, corresponding to a critical coupling of the central antenna to the system. Indeed, we find a distinct minimum of the reflection coefficient  $|R|^2$  for microwave injection at the central antenna, which is demonstrated in [fig. 4.12](#). Starting from a very weakly coupled antenna with a length of 4 mm, one can clearly observe how the minimum of the reflected signal becomes more and more pronounced if the length of the central antenna is increased until it reaches the lowest value for an optimal antenna length of 7 mm and then, as the antenna length is further increased, the antenna coupling decreases again. This transition corresponds to the movement of an  $S$ -matrix zero from the upper half-plane into the lower half-plane of the complex frequency for the case of an absorbing antenna. Moreover, we can see that a different  $S$ -matrix zero crosses the real axis at a frequency close to 6.8 GHz for an antenna length of 7.5 mm. A vanishing reflection coefficient for injection at the central antenna means that the entire injected energy flux is either absorbed in the waveguide material or leaves the system through one of the two leads. Since the global absorption in our waveguide is relatively weak, we can expect that most of the injected signal leaves the system as an outgoing state that should correspond to the time-reversed CPA state which was perfectly absorbed by the central antenna.

In the next step, we want to investigate the properties of the resulting signal that leaves the scattering region when microwaves with the CPA frequency are injected at the central antenna and compare its time-reversed field with the CPA state that we have found independently by evaluating the minimal  $S$ -matrix eigenvalue. For that purpose, we measure the field along the waveguide width in the middle of the space between the scattering region and the external antennas. Featuring a correlation of about 99%, we find a remarkable coincidence of the time-reversed field from injection at the central antenna and the independently determined CPA state (see [fig. 4.13](#)). Small deviations are mainly caused by global absorption effects, which cannot be converted into the respective gain such that the CPA state is not exactly the time-reversed counterpart of the measured signal for injection at the central antenna. In addition, there is a minor influence from

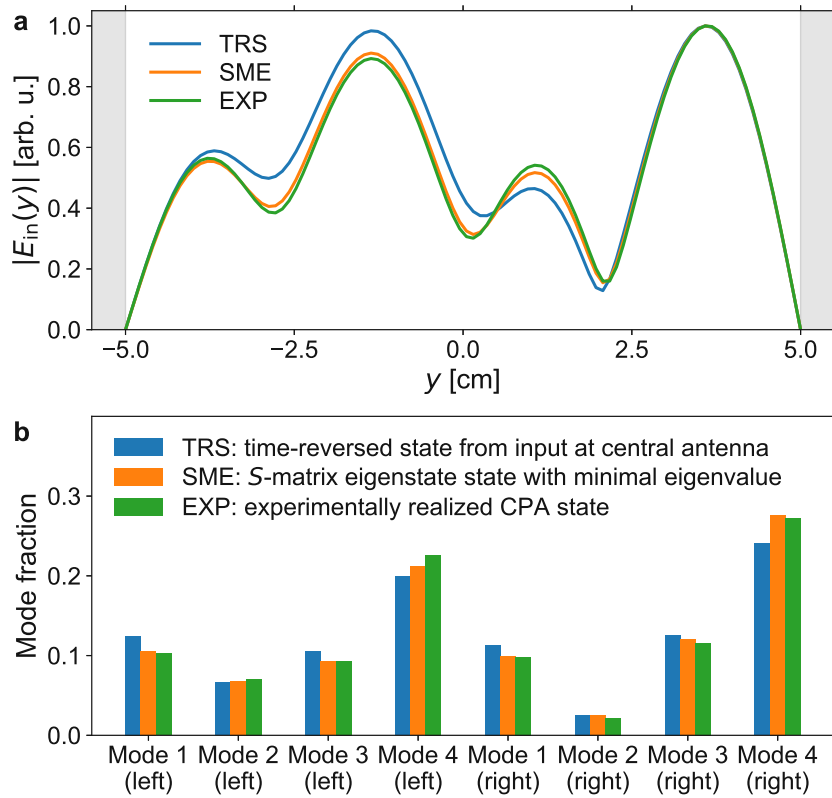


**Figure 4.13:** Time-reversal symmetry analysis of a CPA state. (a) Absolute value of the normalized incoming field along the waveguide width ( $y$ -direction) at one waveguide end compared for a time-reversed state (TRS) from injection at the central antenna and a CPA state for a system with 60 small scatterers. The  $S$ -matrix eigenstate (SME) is the calculated eigenstate corresponding to the minimal eigenvalue of the experimentally measured scattering matrix and the experimentally realized CPA state (EXP) is the actually injected SME (including all experimental imperfections in addition to those already present in the scattering matrix alone). The gray shaded areas represent the waveguide walls. (b) Mode composition of the three states from (a), where the bars show the fraction of the respective mode in the incoming signal.

experimental imperfections such as scattering effects at the external antennas or at the movable measurement antenna. Furthermore, the limited accuracy of the IQ modulators leads to a small error in the injected wavefront, although the correlation between the calculated CPA eigenstate and the actually injected one turns out to be 99.9%, which certifies again the injection accuracy for a specific state in our experimental setup.

In our numerical simulations, where global absorption is neglected, we can calculate the time-reversed CPA states by placing a point source in the middle of the scatterer that represents the central antenna and turn the scatterer's loss into the corresponding amount of gain. For this setting, the resulting correlation between the CPA state and the time-reversed state from input at the central antenna is unity up to  $10^{-14}$ , thus proving the time-reversal symmetry between a CPA and a laser operating at its first threshold.



## Global absorption effects

Our random anti-laser is characterized by two different absorption mechanisms: on the one hand we have a controllable localized absorptive element given by the central antenna, while on the other hand the injected signal is attenuated by the globally distributed loss induced, e.g., by absorption in the metallic waveguide walls or by escape through the small holes in the top plate. Although this global absorption cannot be controlled as efficiently as the loss introduced by the central antenna, it can still play a significant role for the total absorption of an injected signal. As an estimate for the attenuation of the bare waveguide (with the holes in the top plate but without absorbing antenna), we measured the mean transmission through it, where we found that 85.9% of the injected power was transmitted (averaged over all modes and frequencies in the range from 6.55 GHz to 7.35 GHz). In the presence of a disordered medium, however, the attenuation through global absorption can be much larger, in particular for strongly scattering configurations in which certain states are efficiently trapped.

The effect of global absorption compared to the impact of the localized absorbing antenna can be nicely seen in [fig. 4.14](#), where we compare the minimal  $S$ -matrix eigenvalue as a function of the signal frequency with or without the absorbing antenna in place for two different scattering configurations. To illustrate the frequency-dependent coupling strength of the central antenna, we also show the reflection coefficient  $|R|^2$  for injection at the central antenna. In the case of the weakly scattering configuration with 60 small scatterers, the squared absolute value of the minimal  $S$ -matrix eigenvalue without absorbing antenna is about  $|\lambda_{\min}|^2 \approx 0.74$  (averaged over the range from 6.55 GHz to 7.35 GHz). Only if the absorbing antenna is implemented, we can observe strongly reduced values of  $|\lambda_{\min}|^2$ , e.g., around 7.1 GHz in [fig. 4.14a](#). The shape of the curve for the minimal  $S$ -matrix eigenvalue is clearly influenced by the coupling strength of the

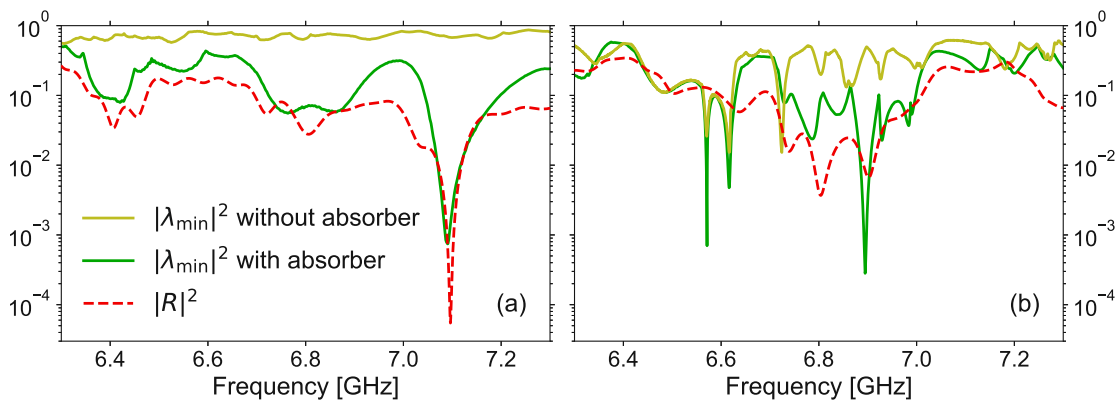


**Figure 4.14:** Influence of the localized absorbing antenna compared to global absorption effects. (a) Comparison of the minimal  $S$ -matrix eigenvalue  $|\lambda_{\min}|^2$  for a weakly scattering system with 60 small scatterers for the cases without and with the central absorbing antenna in place. As a reference, the reflection signal  $|R|^2$  for injection into the central antenna is plotted as well. (b) Corresponding measurements for a strongly scattering system with 60 scatterers of mixed sizes.

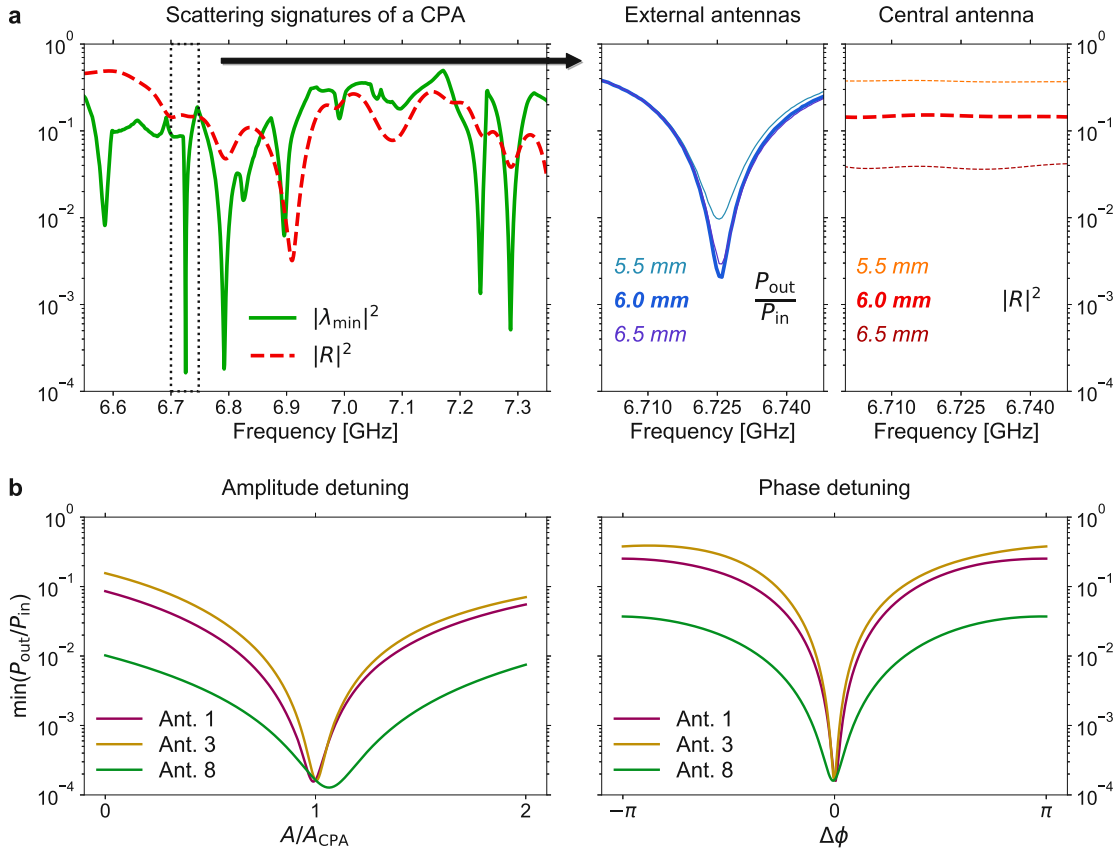


**Figure 4.15:** CPA induced by global absorption for a disordered medium consisting of 75 mixed-size scatterers. (a) Minimal  $S$ -matrix eigenvalue  $|\lambda_{\min}|^2$  compared to the reflection signal  $|R|^2$  as a function of the signal frequency. The panels on the right show the ratio between the outgoing and incoming power  $P_{\text{out}}/P_{\text{in}}$  for the CPA state corresponding to the eigenvalue minimum around 6.725 GHz, as well as the reflection coefficient  $|R|^2$  at the central antenna, each determined for different lengths of the central antenna. (b) Sensitivity of the CPA minimum to detunings in individual IQ modulators, where either the amplitude or the relative phase at an exemplary input antenna are changed while all other antennas remain as required for the CPA state (amplitude  $A_{\text{CPA}}$  and phase  $\phi_{\text{CPA}}$ ). The results presented in (b) were generated by linear superposition of the data from the  $S$ -matrix measurement, whereas the blue curve in (a) represents a direct measurement of the injected CPA state.

central antenna, which suggests that the major contribution for the absorption of the corresponding eigenstate comes from the localized absorbing antenna. In the other case, when we use 60 scatterers of mixed sizes, the minimal  $S$ -matrix eigenvalue can become very small even without absorbing antenna, as for example in the region around 6.6 GHz in fig. 4.14b. Nevertheless, the absorbing antenna improves the absorption efficiency also in this case, in particular at frequency ranges where the minimal  $S$ -matrix eigenvalue without absorbing antenna is rather large, as can be observed at about 6.9 GHz. For the configuration that also contains the large scatterers, scattering is more efficient and the longest achievable dwell times within the scattering region become much larger as

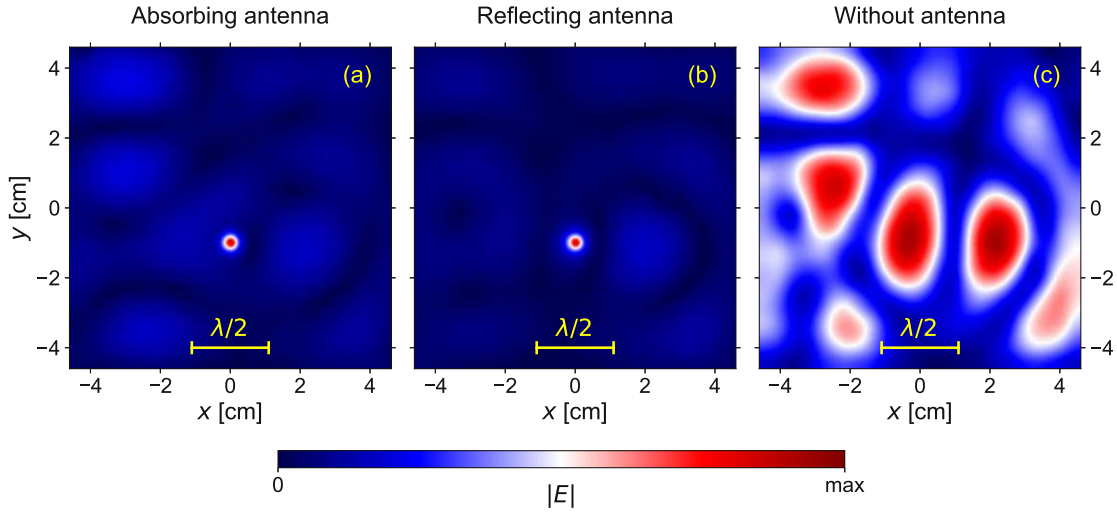
compared to the case where only small scatterers are used. As a result, global absorption delivers a more pronounced contribution to the total absorption, especially for those states that remain strongly trapped in a spatial region that has no overlap with the central antenna.

In strongly scattering systems, one can also find CPA states that are mainly induced by global absorption, as we demonstrate for a disordered medium consisting of 75 mixed-size scatterers. In the left panel of [fig. 4.15a](#), we display the corresponding minimal  $S$ -matrix eigenvalue together with the reflection signal for injection into the central antenna. As compared to the results for the system with 60 small scatterers (cf. [fig. 4.6](#)), we observe that the resonances of the minimal  $S$ -matrix eigenvalue are noticeably sharper when also the large scatterers are included in the disordered medium. In addition to a local minimum close to the position of the minimal reflection signal, we also find several other resonant eigenvalue minima at frequency values where the coupling of the central antenna to the system is much weaker and not resonant at all. This behavior implies the presence of CPA states in the system whose absorption is dominated by the global loss whereas the central antenna plays only a subordinate role. As an example, we inject the CPA state corresponding to the eigenvalue minimum around 6.725 GHz, where we find a minimum of the ratio between outgoing and incoming power below  $2.1 \times 10^{-3}$  (corresponding to more than 99.79% absorption of the injected power). As can be seen in the right panels of [fig. 4.15a](#), the optimal absorption is achieved with an antenna length of 6 mm. Even though the antenna with a length of 6.5 mm is better coupled to the system, the minimum of the ratio  $P_{\text{out}}/P_{\text{in}}$  is increased for both shorter and longer antenna lengths. Therefore, the central antenna can still be used to tune a CPA to and away from the point of maximal absorption, although it is not the dominant source of loss here. Moreover, the absorption efficiency of the CPA state is also very sensitive to detunings in the optimal IQ modulator settings (see [fig. 4.15b](#)).

### Sub-wavelength focusing

Another interesting feature related to coherent perfect absorption is the possibility of focusing waves beyond the diffraction limit. The radiation of a point source is described by the *causal Green's function*, while its counterpart, the *anti-causal Green's function* represents a spherically converging wave [105]. In free space, however, any converging wave is followed by a diverging one. Due to their interference, the smallest possible dimension for a wave's focal spot is half the wavelength ( $\lambda/2$ ) [150]. In the case of our random anti-laser, a CPA state is perfectly absorbed such that in the vicinity of the central absorbing antenna the magnitude of the diverging waves is strongly reduced, leaving only the converging contributions behind. Free from interference with the outgoing waves, the incoming signal can then be focused to much smaller spot sizes than the ordinary limit. This effect has already been experimentally demonstrated for both acoustic and electromagnetic waves [103–105]. While these experiments were not carried out in a disordered or otherwise complex medium, our system would allow to do that.

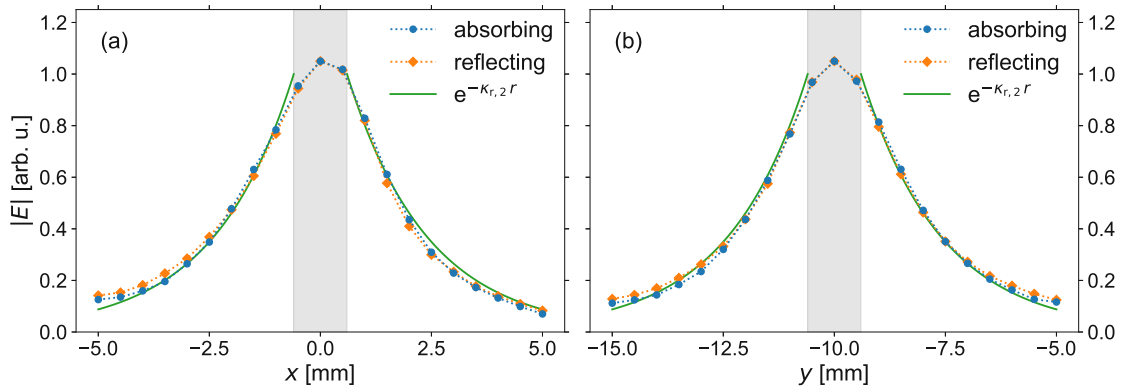
To visualize the sub-wavelength focusing property of a CPA, we have slightly modified the experimental setup to measure the microwave field around the central antenna with a



**Figure 4.16:** Focal spot size of a CPA state around the central antenna. The plots show the absolute value of the measured microwave field  $|E|$  of a CPA state for different configurations of the central antenna: absorbing antenna (a), reflecting antenna (b), and without antenna (c). For comparison, the size of a half wavelength  $\lambda/2 \approx 2.2$  cm is indicated by a scale bar. The field was measured on a grid with a spacing of 4 mm and interpolated between the grid points. For (a) and (b), the spacing between the measurement points was reduced to 1 mm within a square of side length 2 cm around the central antenna.

much finer spatial resolution. The result for a CPA state at a frequency of 6.806 GHz in a disordered medium consisting of 70 small and 4 large scatterers is presented in [fig. 4.16a](#). At first glance, the measurement confirms the expected behavior as we find a pronounced focal spot much smaller than  $\lambda/2$  at the position of the central antenna. To check whether the observed sub-wavelength spot size is indeed a feature of the CPA state, we have replaced the  $50 \Omega$  terminating resistance by a short circuit termination, which turns the central antenna from an absorber into a reflector. Surprisingly, when we inject the same CPA state into the system with the reflecting central antenna, we measure an equally small focal spot size as compared to the case with an absorbing central antenna (see [fig. 4.16b](#)). Only if the central antenna is completely removed from the waveguide, the sub-wavelength focusing feature disappears, which can be seen in [fig. 4.16c](#). The size of the other intensity maxima in the interference pattern is on the order of the half wavelength  $\lambda/2$ .

As a closer inspection reveals, the observed sub-wavelength focal spot in [figs. 4.16a](#) and [4.16b](#) is due to the emergence of evanescent modes at the edge of the central antenna. The spatial dependence of the transverse modes along the  $z$ -direction is given by  $\cos(k_{z,n} z)$  [147], where  $k_{z,n} = n\pi/h$ ,  $n \in \mathbb{N}_0$ , and  $h$  is the height of the waveguide. Due to the small height of the waveguide (8 mm), only the modes with  $n = 0$  are propagating modes. All other modes (in the following referred to as  $z$ -modes) with  $n > 0$  can only exist as evanescent modes which decay exponentially with the radial distance  $r$  from their origin ( $\propto e^{-\kappa_{r,n} r}$ ). The decay constant can be calculated as  $\kappa_{r,n} = \sqrt{k_{z,n}^2 - k^2}$ .



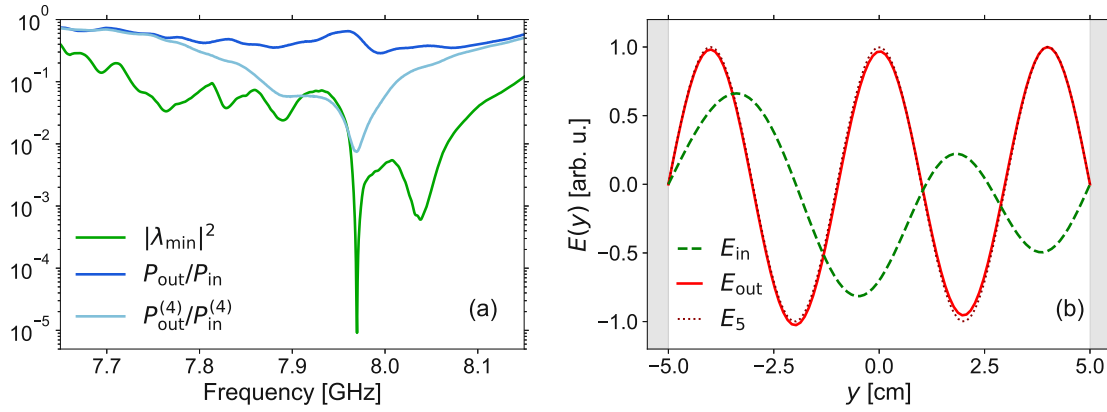
**Figure 4.17:** Evanescent modes at the central antenna. The plots show a cross section of the electric field through the central antenna along the  $x$ -direction (a) and the  $y$ -direction (b), measured both for an absorbing and for a reflecting configuration of the central antenna. The green curve depicts the exponential decay of the second transverse  $z$ -mode with extinction coefficient  $\kappa_{r,2}$ . The gray shaded area marks the position of the central antenna.

Figure 4.17 depicts a cross section of the microwave field through the position of the central antenna. Both for the absorbing and for the reflecting configuration of the central antenna, the measured data points lie clearly on the exponentially decaying curve that is associated with the second evanescent  $z$ -mode. The presence of these evanescent modes prevents us from measuring the sub-wavelength focus as a result of the CPA.

### Reflectionless scattering

For the injection of a CPA state into our system, it is necessary to be in control of all relevant degrees of freedom (i.e., the complex amplitudes of all transverse modes in the incoming signal). In principle, however, the parameters could also be optimized in such a way that only some of the transverse modes are suppressed in the outgoing signal or that, for instance, a superposition of the first and second mode as input is converted to an output containing only the third and fourth mode. This phenomenon is referred to as *reflectionless scattering* and was recently treated in literature [151].

In the frequency range between 6 GHz and 7.5 GHz, our waveguide supports four transverse modes, which makes a total of eight modes (four on each side) that have to be controlled in order to inject a specific state, e.g., a CPA state. With our eight external antennas, this requirement is fulfilled. In the frequency range between 7.5 GHz and 9 GHz, on the other hand, the waveguide supports five transverse modes such that two additional external antennas would be necessary to be in full control of the injected wavefront. Following the same procedure as in the case with four open transverse modes, one can determine a scattering matrix for up to eight modes (limited by the number of external antennas). For that purpose, it can be arbitrarily chosen which of the ten modes (five on each side) should be taken into account, for example modes one through four on each side. In this case, the  $S$ -matrix contains no information about the fifth transverse mode but only the scattering characteristics of the first four modes. Similar as for a



**Figure 4.18:** Reflectionless scattering in a random anti-laser with a disordered medium consisting of 60 small scatterers. (a) Minimal  $S$ -matrix eigenvalue  $|\lambda_{\min}|^2$  and ratio between outgoing and incoming power with respect to all modes ( $P_{\text{out}}/P_{\text{in}}$ ) and considering only the first four modes ( $P_{\text{out}}^{(4)}/P_{\text{in}}^{(4)}$ ), respectively. (b) Normalized incoming microwave field  $E_{\text{in}}$  compared to the resulting outgoing field  $E_{\text{out}}$  measured along the  $y$ -direction on one side of the waveguide. The shape of the fifth transverse mode  $E_5$  is given by the dotted curve. The gray shaded areas represent the waveguide walls.

CPA, one can identify parameter configurations where the minimal eigenvalue of this reduced  $S$ -matrix almost dips to zero. However, it should be kept in mind that a vanishing eigenvalue of this  $8 \times 8$   $S$ -matrix is not necessarily related to a vanishing outgoing signal. Instead, it means that the input from the first four modes is either absorbed by the system or scattered into the fifth mode such that the outgoing signal mainly consists of the fifth mode.

This behavior, which can be used to implement a mode filter, is illustrated in [fig. 4.18](#) for a disordered medium consisting of 60 small scatterers. The minimal eigenvalue of the reduced  $S$ -matrix features a pronounced dip at a frequency of 7.97 GHz (see [fig. 4.18a](#)). The corresponding eigenstate, however, is not perfectly absorbed by the system as can be seen from the measured ratio between outgoing and incoming power ( $P_{\text{out}}/P_{\text{in}}$ , taking all five transverse modes into account). At the same time, if only the first four transverse modes are considered, the ratio between outgoing and incoming power ( $P_{\text{out}}^{(4)}/P_{\text{in}}^{(4)}$ ) is significantly decreased in the frequency range around the eigenvalue minimum, corresponding to more than 99% absorption (or scattering into the fifth mode) of the power contribution from the first four modes. A measurement of the microwave field outside the scattering region confirms that indeed the signal contributions from the first four modes are filtered out of the incoming signal such that the outgoing signal contains only the fifth mode (see [fig. 4.18b](#)).

# Chapter 5

## Coherent virtual absorption

As discussed in [chapter 4](#), a CPA can be realized if a critical amount of loss is introduced into a suitable system such that one of the  $S$ -matrix zeros hits the real axis in the complex frequency plane. However, it could be shown that  $S$ -matrix zeros can also be directly addressed by an input signal with a complex frequency [106]. At first glance, a complex value for the signal frequency appears peculiar, but the meaning becomes clear if we consider a time-harmonic input with angular frequency  $\omega = 2\pi\nu$  and amplitude  $E_0$ , which is given by

$$E(\mathbf{r}, t) = E_0(\mathbf{r}) e^{-i\omega t}. \quad (5.1)$$

Inserting a complex-valued frequency  $\omega = \omega_R + i\omega_I$  into [eq. \(5.1\)](#) then yields

$$E(\mathbf{r}, t) = E_0(\mathbf{r}) e^{\omega_I t} e^{-i\omega_R t} =: \tilde{E}_0(\mathbf{r}, t) e^{-i\omega_R t}, \quad (5.2)$$

which represents an input signal oscillating with the real frequency  $\omega_R$  but with a temporally modulated amplitude  $\tilde{E}_0$  that increases or decreases exponentially in time, depending on the sign of the imaginary part  $\omega_I$ . Based on this insight, it is possible to inject a signal with exponentially increasing amplitude into a lossless object without any backscattering from it (corresponding to a vanishing  $S$ -matrix eigenvalue). The principle behind this behavior is that all backscattered contributions are annihilated by destructive interference such that only an incoming and no outgoing energy flux remains. This phenomenon is referred to as *coherent virtual absorption*, although the term *absorption* is somewhat misleading in this context since the incoming energy is not dissipated but only transiently stored inside the system, and will be released again once the exponentially growing input signal is stopped.

As shown in [appendix B.2](#), the propagation of electromagnetic waves in the cases considered in this thesis is described by the Helmholtz equation

$$\left[ \Delta + n^2(\mathbf{r})k^2 \right] \psi(\mathbf{r}) = 0, \quad (5.3)$$

in which  $\psi(\mathbf{r})$  represents the electromagnetic field. For the moment, let us assume a constant refractive index  $n(\mathbf{r}) \equiv n_R + in_I$ . For a CPA, the refractive index is complex and the wavenumber is real, whereas for a *coherent virtual absorber* (CVA), the refractive index is real and the wavenumber is complex. [Equation \(5.3\)](#) has the same solutions in

both cases if the product of the refractive index and the wavenumber satisfies the relation

$$\left(n_{\text{R}}^{(\text{CPA})} + in_{\text{I}}^{(\text{CPA})}\right)k^{(\text{CPA})} = n^{(\text{CVA})} \left(k_{\text{R}}^{(\text{CVA})} + ik_{\text{I}}^{(\text{CVA})}\right). \quad (5.4)$$

Therefore, the effect of coherent virtual absorption is closely related to the occurrence of a CPA in a system with uniform global loss because mathematically the two different variants lead to equivalent equations and hence also to equivalent solutions.

## 5.1 Basic realization

To illustrate the effect of coherent virtual absorption, we consider the same basic CPA system that was already analyzed in [fig. 4.3](#), with the difference that we now assume a real refractive index  $n = 3$ . Accordingly, all zeros of the scattering matrix are located in the upper half of the complex frequency plane (see [fig. 5.1a](#)). In fact, it turns out that the outgoing signal can be completely suppressed if the amplitude of the incoming signal is exponentially increased in time in such a way that the related complex frequency corresponds to one of the  $S$ -matrix zeros. This behavior is visualized in [fig. 5.1b](#).

Similar as for a CPA, also a coherent virtual absorber (CVA) relies on the precise tuning of the signal parameters. In contrast to the CPA case, however, it is much easier for a CVA to absorb multiple modes simultaneously because the zeros are not needed to be pulled down onto the real frequency axis by introducing the exact right amount of loss but can be addressed independently of each other<sup>9</sup>. This becomes clear if we take a look at [fig. 5.1c](#), where the behavior of the  $S$ -matrix eigenvalues as a function of the real part of the frequency  $\omega_{\text{R}}$  is investigated while the imaginary part is kept constant at the optimized value  $\omega_{\text{I}}^{(\text{CVA})}$  where the CVA occurs, which is the same for all zeros of the scattering matrix in this case. At each resonance frequency, one of the eigenvalues drops to zero such that the outgoing signal of the corresponding eigenstate vanishes. Finally, [fig. 5.1d](#) shows the dependence of the eigenvalues on the imaginary part of the frequency  $\omega_{\text{I}}$  for fixed real part  $\omega_{\text{R}} = \omega_{\text{R}}^{(\text{CVA})}$ . As expected, the outgoing signal of the CVA state vanishes only for the optimized value  $\omega_{\text{I}} = \omega_{\text{I}}^{(\text{CVA})}$ , whereas both smaller and larger values lead to a non-vanishing outgoing signal.

While theoretically in simulations coherent virtual absorption could be maintained for arbitrarily long times (if the field values are periodically rescaled to prevent numerical overflow), real experiments are limited when the system suffers damage due to the exponentially increasing field intensities or the signal source approaches its power limits. In such cases, the incident signal would be switched off or at least the exponential increase would be stopped. In order to explore the response of the system to a sudden change of the incoming waveform, we perform a full time-dependent simulation by solving the one-dimensional wave equation (see [appendix B.1](#) for technical details). The simulation is started in a stationary CVA state with frequency  $\omega = \omega_{\text{R}}^{(\text{CVA})} + i\omega_{\text{I}}^{(\text{CVA})}$  such

<sup>9</sup> This is possible as long as the propagation of electromagnetic waves remains linear such that multiple signals are simply superimposed. Due to the exponentially increasing field intensities inside the medium, however, the perfect virtual absorption would break down when nonlinear effects set in.



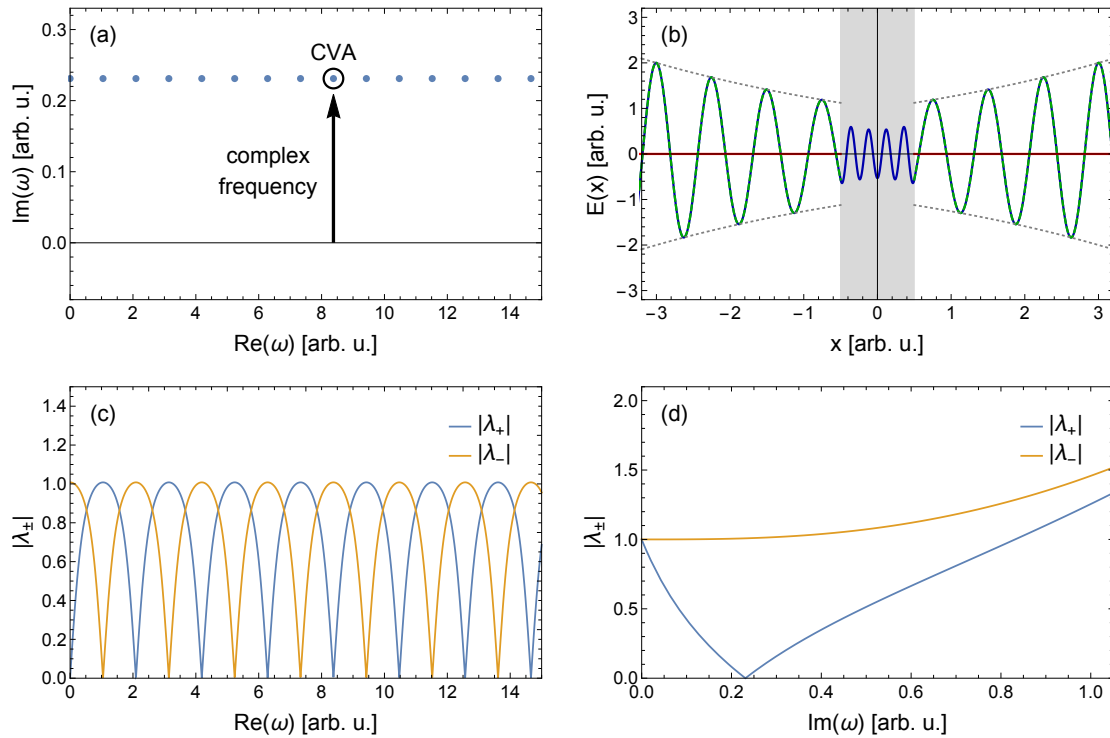


**Figure 5.1:** Coherent virtual absorption in a planar dielectric medium (refractive index  $n = 3$ ). (a)  $S$ -matrix zeros in the complex frequency plane. By injecting a signal whose amplitude increases exponentially in time (corresponding to a complex frequency), the zeros can be addressed even without introducing loss. (b) Field of a corresponding CVA state with complex frequency  $\omega = 8.378 + 0.231 i$  (arbitrary units): incoming field (green dashed), outgoing field (red), and total field (blue), with the exponential envelope given by the grey dotted curve. The gray shaded area represents the (lossless) medium. (c)  $S$ -matrix eigenvalues for the symmetric ( $\lambda_{+}$ ) and anti-symmetric ( $\lambda_{-}$ ) eigenvectors as a function of the real part of the signal frequency for optimized imaginary part  $\omega_{\text{I}} = 0.231$  (arbitrary units). (d)  $S$ -matrix eigenvalues as a function of the imaginary part of the signal frequency for optimized real part  $\omega_{\text{R}} = 8.378$  (arbitrary units).

that for negative times  $t < 0$  the input amplitude increases exponentially and the scattered field vanishes. During this phase, the entire incoming energy flux is stored inside the system such that the intra-cavity field intensity and hence the stored energy increase exponentially in time as well. At time  $t_0 = 0$ , the incoming signal is continuously turned off within half an oscillation period, which is done by multiplying the incoming field with the switch-off function  $f(t) = \frac{1}{2}[1 + \cos(\omega_{\text{R}}^{(\text{CVA})} t)]$  for  $0 \leq t \leq \pi/\omega_{\text{R}}^{(\text{CVA})}$ . After that, the input remains equal to zero. Due to the change of the optimized CVA waveform, the condition for destructive interference is violated and the output is not suppressed anymore. As a consequence, the stored energy is released from the system. This result is presented in [fig. 5.2](#).

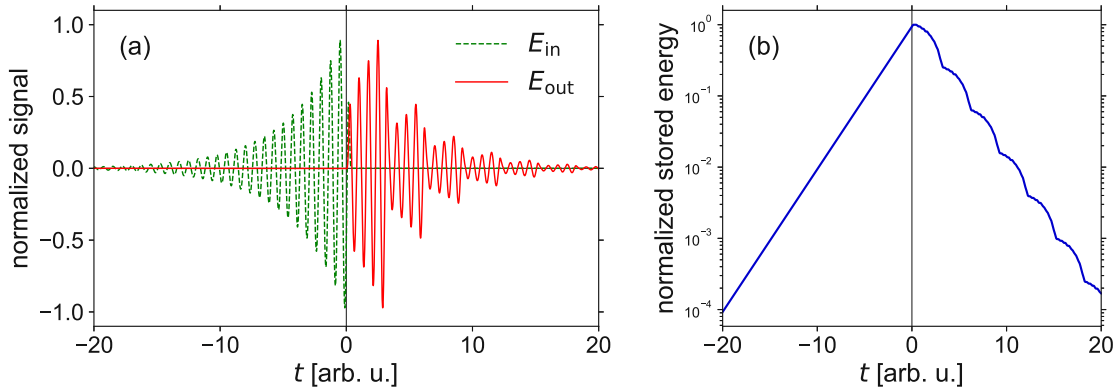


**Figure 5.2:** Temporal dependence of the field and stored energy from the CVA presented in fig. 5.1b. (a) Incoming (green dashed) and outgoing (red) field components normalized with respect to the maximum in the considered time interval. For  $t < 0$ , a CVA state with complex frequency  $\omega = 8.378 + 0.231 i$  (arbitrary units) is injected such that the outgoing field vanishes. At  $t = 0$ , the incoming field is switched off within half an oscillation period. (b) Stored energy within the system as a function of time. For  $t < 0$ , the stored energy increases exponentially. After  $t = 0$ , when the incoming field is switched off, the stored energy is released again.

## 5.2 Disordered media<sup>10</sup>

Analogously as for coherent perfect absorption, also the effect of coherent virtual absorption can be generalized to the case of complex scattering environments. To illustrate this effect, we start with a basic example of a disordered medium consisting of five randomly placed slices of a lossless dielectric material with refractive index  $n = 2$  and random thickness. This system can be reduced to a one-dimensional scattering problem which is described by eq. (4.2). Since the refractive index  $n(x)$  is a piecewise constant function for this case, the Helmholtz equation could in principle be solved analytically, as discussed in section 4.1. However, the optimization of the incoming signal to realize a CVA must be performed numerically because the requirement that the outgoing field components vanish leads to a set of transcendental equations for the complex frequency  $\omega$  and the field amplitudes  $A_L$  and  $A_R$  of the injected signals from left and right.

For simplicity, we also calculate the solution of the Helmholtz equation by means of a numerical simulation, which is explained in appendix B.2. The optimization of the input field is done with the help of the function `optimize.minimize` from the open-source Python library *SciPy*<sup>11</sup>, where we use the ratio between the outgoing and incoming field amplitudes  $|E_{\text{out}}| / |E_{\text{in}}|$  at the edge of the scattering region as objective function. In this way, we can readily find a CVA state with frequency  $\omega = 16.06 + 0.37 i$  (arbitrary units), which is shown in fig. 5.3a, where we display a steady-state snapshot of the

<sup>10</sup> The theoretical framework for the content of this section is based on the Bachelor theses [152, 153] of Andrea Pupić and Thomas Ranner, whose projects on this topics I supervised. Part of the numerical code for the simulations was provided by Matthias Kühmayer.

<sup>11</sup> <https://scipy.org/>

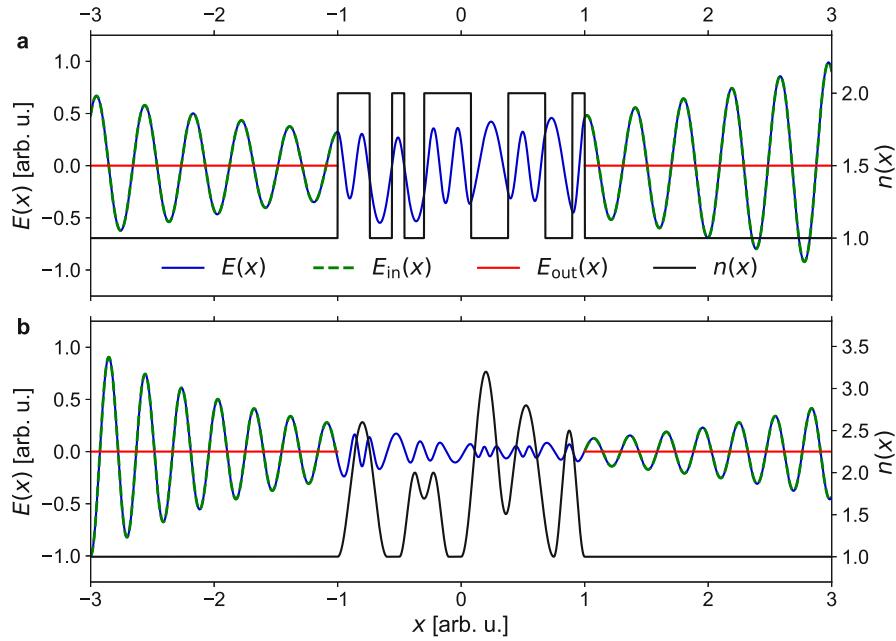


**Figure 5.3:** Coherent virtual absorption in one-dimensional disordered media. (a) Simulation of the electric field  $E(x)$  of a CVA state for a disordered medium consisting of five layers of random thickness, made out of a material with refractive index  $n = 2$ . Outside the structure, there is only an incoming signal ( $E_{in}$ ) while the outgoing signal ( $E_{out}$ ) vanishes. (b) Corresponding simulation for a disordered medium with a complex material composition.

electric field in the system at an arbitrary time  $t_0$ . The amplitude ratio between the left and the right input signal for this CVA state is given by  $|A_L| / |A_R| = 0.68$  and the relative phase is calculated as  $\Delta\phi = \phi_L - \phi_R = -0.34$ . Although the outgoing field vanishes for these parameter settings, it should be kept in mind that the incident energy is only temporarily stored inside the structure and will be released again as soon as the signal form is changed. To corroborate the robustness of our optimization approach, we apply it to a more complicated disordered structure with a spatial dependence of the refractive index  $n(x)$  that cannot be treated analytically anymore. Also in this case, we can immediately find a CVA state (see [fig. 5.3b](#)). This CVA state features a frequency of  $\omega = 21.36 + 0.67i$  (arbitrary units) with amplitude ratio  $|A_L| / |A_R| = 2.16$  and relative phase  $\Delta\phi = 0.33$ .

The CVA states presented in [fig. 5.3](#) represent only one of many possible realizations and the results depend on the initial values fed into the optimization algorithm. In fact, there are infinitely many zeros that could be individually addressed by tuning the input signal to the respective complex frequency with the corresponding amplitude and phase settings. To illustrate the distribution of the  $S$ -matrix poles and zeros in the complex frequency plane, we perform a parameter scan of the real and imaginary parts of the frequency and evaluate the determinant of the scattering matrix for each combination of these values. Due to the fact that the determinant of a matrix can be written as the product of its eigenvalues, a vanishing determinant corresponds to the presence of a zero

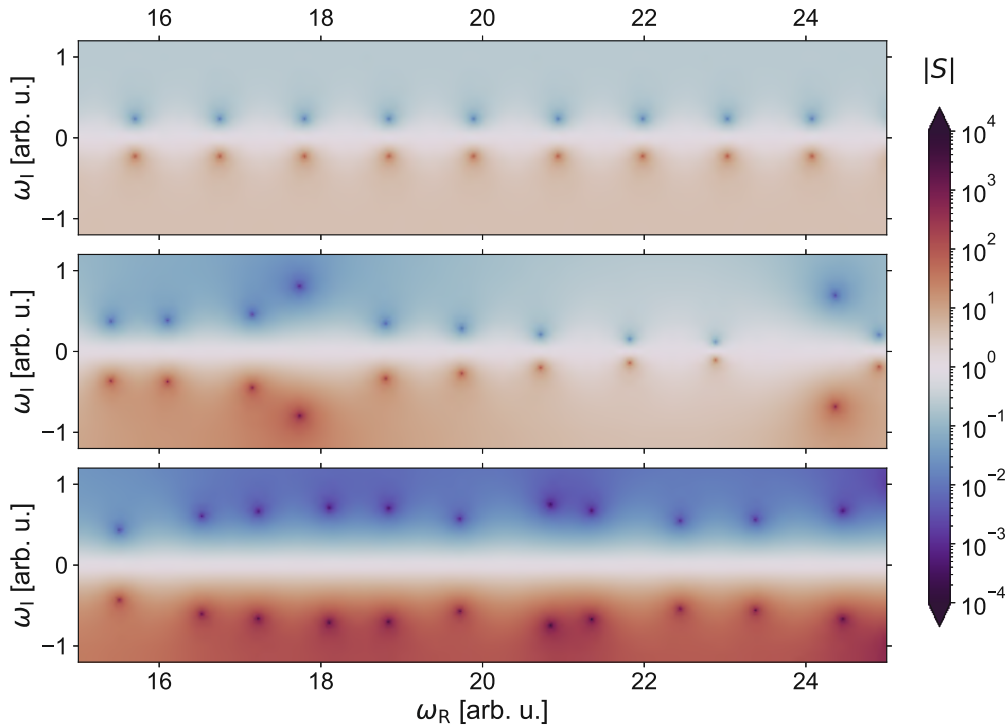


**Figure 5.4:** Poles and zeros of the scattering matrix in the complex frequency plane. The plots show the absolute value of the determinant of the  $S$ -matrix for the CVA systems from [fig. 5.1b](#) (top), [fig. 5.3a](#) (center), and [fig. 5.3b](#) (bottom). The pronounced dots at which the value of the determinant becomes particularly low (high) suggest the presence of a zero (pole) at these parameter values.

whereas a diverging determinant indicates a pole of the scattering matrix. The results for the planar dielectric medium from [fig. 5.1](#) as well as for the disordered systems from [fig. 5.3](#) are consolidated in [fig. 5.4](#). For the planar dielectric medium we find a set of equally spaced zeros in the upper half-plane of the complex frequency that was already presented in [fig. 5.1a](#). Because we are dealing with Hermitian systems, the corresponding set of  $S$ -matrix poles is symmetrically mirrored around the real frequency axis, as discussed in [section 4.1](#). For the disordered scattering systems, the poles and zeros are irregularly distributed but still symmetrically arranged around the real axis.

With a slight modification of the optimization procedure, it is possible to generate input states whose scattered field is suppressed only on one side of the system. In particular, we can realize one-dimensional reflectionless scattering modes [151] if we inject a signal only from one side and optimize its complex frequency in such a way that the outgoing field on the same side is suppressed while a non-vanishing outgoing field is allowed on the opposite side. This is demonstrated for the example of a disordered medium consisting of six random layers of different dielectric materials in [fig. 5.5](#). In the first case, we inject a signal from the left side and get an outgoing field only on the right side ([fig. 5.5a](#)), and vice versa in the second case ([fig. 5.5b](#)). Similar as discussed before for the CVA states, it is possible to realize this behavior with different frequencies.

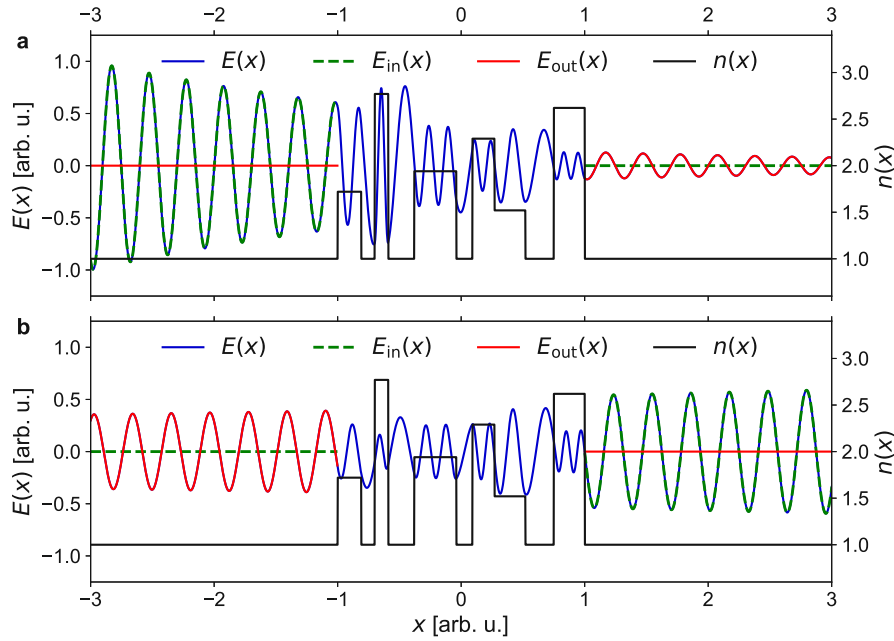


**Figure 5.5:** One-dimensional reflectionless scattering modes for a disordered medium consisting of six layers of various dielectric materials with different widths. (a) Simulation of a reflectionless scattering mode injected from the left side with frequency  $\omega = 20.82 + 0.25 i$  (arbitrary units). (b) Corresponding simulation for a reflectionless scattering state with frequency  $\omega = 20.11 + 0.05 i$  (arbitrary units) injected from the right side.

It should be noted, however, that the reflectionless scattering modes are not related to  $S$ -matrix zeros because they are neither eigenstates of the scattering matrix nor is their total outgoing field equal to zero.

Finally, we examine the realization of coherent virtual absorption in two-dimensional disordered media. For that purpose, we consider the weakly scattering system with 60 small scatterers as well as the strongly scattering system with 60 scatterers of mixed sizes from [section 4.2](#), with the difference that the central absorbing antenna has been removed to make the system lossless. Numerical simulations prove that the (complex) frequency of the input state can be optimized in such a way that the outgoing signal vanishes. For this optimization, we have chosen the respective CPA frequency (from the case where the central antenna is present) as a start value and varied the real and imaginary parts of the frequency until the minimal  $S$ -matrix eigenvalue became sufficiently small, i.e.,  $|\lambda_{\min}| < 10^{-6}$ . For the weakly scattering system, we find an optimized frequency of  $\nu = (7.191 + 0.145 i)$  GHz, and for the strongly scattering system we get  $\nu = (6.972 + 0.048 i)$  GHz. The intensity of the corresponding CVA states is imaged in [fig. 5.6](#). Additionally, the Poynting vector of the field is depicted, which is directed inwards into the scattering region but due to the absence of the central antenna there is no sink for the energy flux.

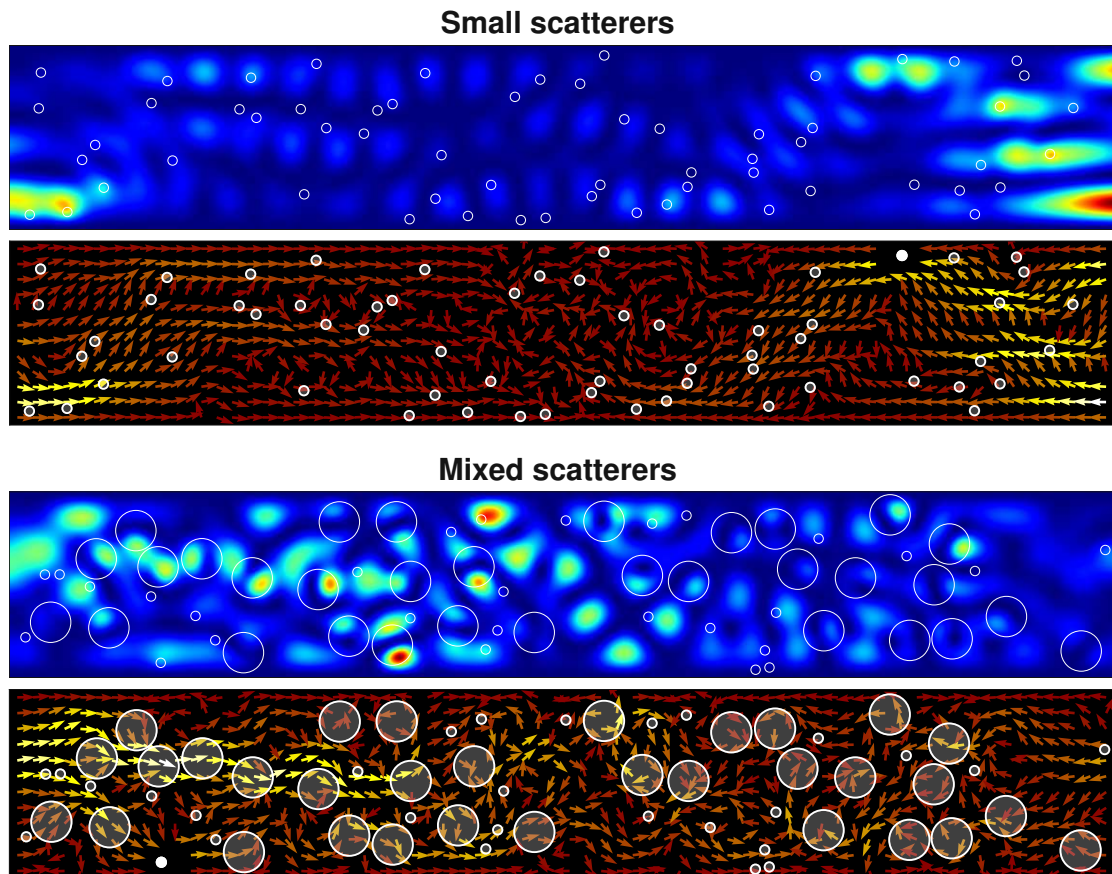


**Figure 5.6:** Coherent virtual absorption in two-dimensional disordered media for a weakly scattering configuration of 60 small scatterers and for a strongly scattering configuration with 60 scatterers of mixed sizes. The plots show the microwave intensity (top panels) as well as the Poynting vector (bottom panels) of the injected CVA states inside the scattering region. White circles represent the scatterers.

# Chapter 6

## Customized coherent perfect absorption

As discussed in [chapter 4](#), coherent perfect absorption works in a given system only for specific input states, namely for the eigenstates of the scattering matrix with vanishing eigenvalue. In order to improve the applicability of the anti-lasing effect for technological purposes, it would be desirable to construct a system in such a way that a predefined input signal will be perfectly absorbed. In this chapter we present several methods to realize perfect absorption for predefined frequencies or wavefronts—either by customized engineering of the system structure or by temporal modulation of the amplitude of the incoming signal.

### 6.1 Perfect absorption of specific states<sup>12</sup>

In a general system, the frequency as well as the specific wavefront of a possible CPA state is determined by the inner structure and material composition of the system. Under certain prerequisites, however, it can be possible to engineer a system in such a way that a predefined input signal gets perfectly absorbed. For that purpose, it is necessary to be in control of a sufficiently large number of adjustable degrees of freedom which can be varied in a suitable range of values compatible to the desired frequency and wavefront.

As a simple example, we investigate the construction of a CPA for a predefined input state in a one-dimensional system consisting of an absorbing element placed between two partially reflective mirrors (see [fig. 6.1](#)). In the simulations, which are executed according to [appendix B.2](#), the mirrors are modeled by thin layers of dielectric materials with real refractive indices  $n_1$  (left) and  $n_2$  (right). In the first step, we start with an arbitrary configuration of the system and try to find one of the possible CPA states. Similar as explained in [section 5.2](#), we perform an optimization of the incoming field and the loss in the absorbing element and find a CPA state at a frequency of 32.22 arb. u. with evenly balanced amplitudes from left and right (see [fig. 6.1a](#)). In the next step, we define an incoming state with frequency  $\omega = 40$  arb. u., amplitude ratio  $|A_L| / |A_R| = 0.8$ , and relative phase  $\Delta\phi = \pi/2$  between the left and the right signal source. To realize perfect absorption, we optimize the system parameters, where we choose the length and the loss of the absorbing element, as well as the position and the refractive index of the

<sup>12</sup> The theoretical framework for the content of this section is based on the Bachelor theses [154, 155] of Katharina Hauer and Felix Russo, whose projects on this topic I supervised. Part of the numerical code for the simulations was provided by Matthias Kühmayer.

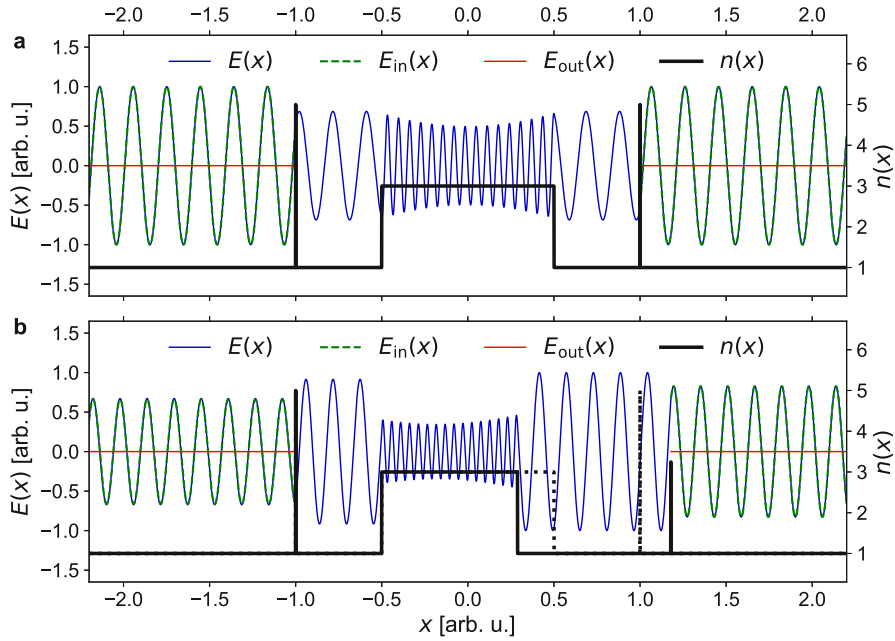


**Figure 6.1:** Coherent perfect absorption of a predefined input state in a one-dimensional system. (a) Original system consisting of two partially reflective mirrors ( $n_1 = n_2 = 5$ ) with an absorbing element ( $n_{\text{abs}} = 3 + 0.0406i$ ) in between. A CPA state can be found at a frequency of  $\omega = 32.22$  (arbitrary units). (b) Optimized system geometry for an arbitrarily chosen input state with frequency  $\omega = 40$  (arbitrary units), amplitude ratio  $|A_L| / |A_R| = 0.8$ , and relative phase  $\Delta\phi = \pi/2$ . For the refractive index profile, we find the following optimized values:  $n_1 = 5$ ,  $n_2 = 3.25$ , and  $n_{\text{abs}} = 3 + 0.0235i$ . The dotted black curve shows the original shape of the refractive index from (a).

right mirror as free parameters with reasonable bounds such that the absorber remains located between the mirrors and the material parameters stay within a realistic range of values. The optimized system together with the predefined CPA state is displayed in [fig. 6.1b](#). The final result of the parameter optimization strongly depends on the initial guess that is passed to the minimization routine. In fact, there are many different possible parameter configurations to realize perfect absorption for the given input state. For example, the position of the right mirror is determined only up to an integer multiple of the wavelength since it merely causes a phase shift.

For the customization of a multi-dimensional CPA, the utilization of a disordered medium proves to be very helpful. This can be demonstrated, for instance, with the help of our random anti-laser system from [section 4.2](#), where we consider the disordered medium consisting of 60 small scatterers. Due to the large number of scatterers, this system features a good degree of control if the scatterer positions can be varied deliberately. With the randomly implemented arrangement as displayed in [fig. 4.4](#), we found a CPA state at a frequency of about 7.1 GHz. Our goal for now is to change the scatterer configuration in such a way that a CPA occurs at the arbitrarily chosen frequency  $\nu = 6.7$  GHz. To this end, we implement a numerical gradient descent algorithm to optimize the scatterer positions for the desired input frequency. For each scatterer, we



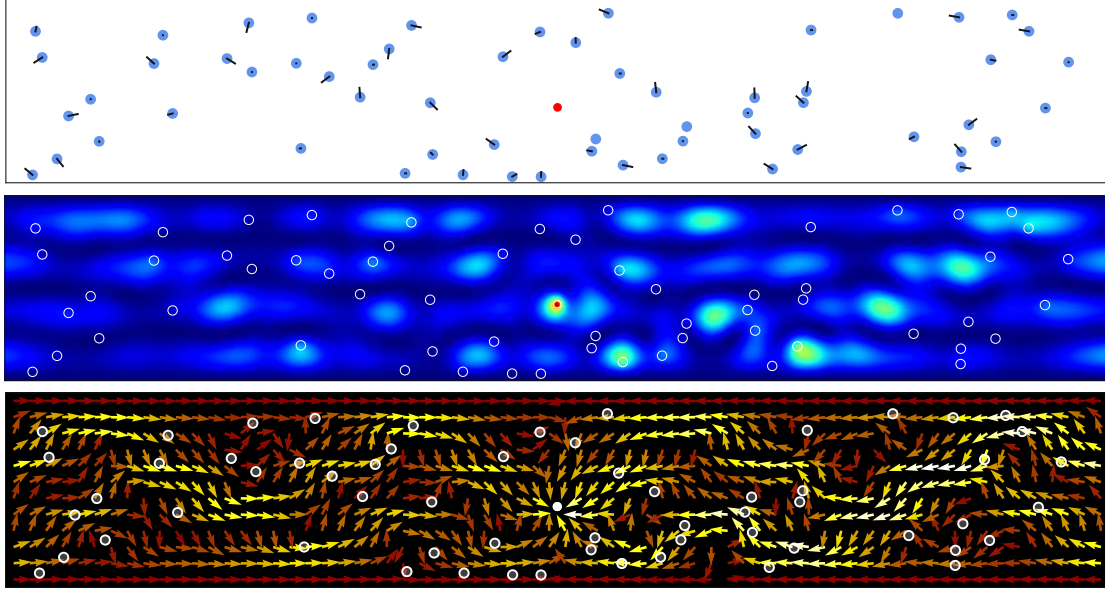


**Figure 6.2:** Customized two-dimensional coherent perfect absorber for a predefined signal frequency of 6.7 GHz. Top panel: optimization of the scatterer positions. Blue circles depict the scatterers, the red circle corresponds to the absorbing antenna, and the black lines show the paths along which the scatterers have been shifted during the iteration. Middle panel: microwave intensity of the injected CPA state, where the scatterers and the antenna are indicated as white circles. Bottom panel: Poynting vector of the injected CPA state.

determine the gradient of the absolute value of the minimal  $S$ -matrix eigenvalue  $|\lambda_{\min}|$  with respect to small shifts in  $x$ - and  $y$ -direction, and then shift the respective scatterer in the opposite direction. Specifically, we iterate the scatterer positions according to

$$\mathbf{r}_n^{(i+1)} = \mathbf{r}_n^{(i)} - \delta s \nabla |\lambda_{\min}(\mathbf{r}_n^{(i)})|, \quad (6.1)$$

where  $\mathbf{r}_n$  is the position vector of the  $n^{\text{th}}$  scatterer and  $\delta s$  is an adaptive step size. This is done until the break condition  $|\lambda_{\min}| < 10^{-6}$  is met. In this way, we are able to achieve coherent perfect absorption with relatively small adjustments in the scatterer configuration, which is illustrated in [fig. 6.2](#). As already observed in the simulations for the original configuration (cf. [fig. 4.8](#), left part), we find that the injected CPA state features a pronounced intensity maximum around the central antenna. Moreover, the energy flux is directed solely inwards close to the absorber.

In the next step, we go even further and demand that not only the frequency of the incoming signal is fixed to 6.7 GHz but also the wavefront can be arbitrarily chosen, e.g., only the fourth transverse mode is injected into the waveguide. Running the same optimization algorithm as before, it is also in this case possible to realize coherent perfect absorption by changing the disorder. As can be seen in [fig. 6.3](#), however, larger shifts than before are necessary because here we have imposed even stronger restrictions on the incoming signal. Both the field intensity and the Poynting vector now clearly exhibit the signature of the fourth transverse mode in the outer area of the scattering region, while

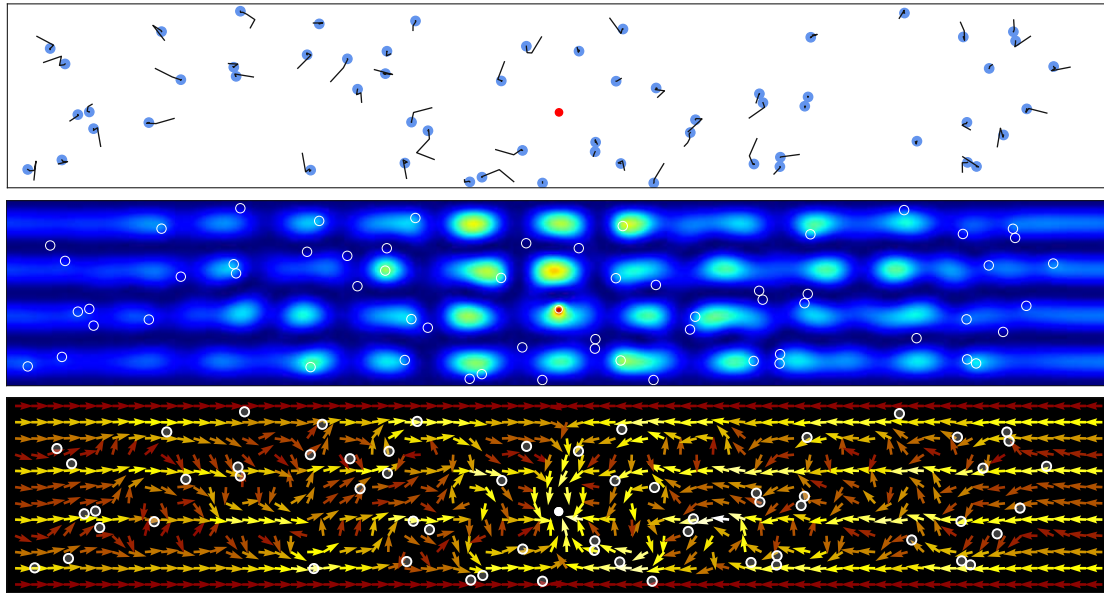


**Figure 6.3:** Customized two-dimensional coherent perfect absorber for a predefined input state with given signal frequency (6.7 GHz) and wavefront (only the fourth transverse mode is injected). Top panel: optimization of the scatterer positions. Blue circles depict the scatterers, the red circle corresponds to the absorbing antenna, and the black lines show the paths along which the scatterers have been shifted during the iteration. Middle panel: microwave intensity of the injected CPA state, where the scatterers and the antenna are indicated as white circles. Bottom panel: Poynting vector of the injected CPA state.

in the vicinity of the absorbing antenna, there is still a pronounced maximum of the field intensity and the energy flux has only inward-pointing components. Remarkably, the iteration procedure causes some of the scatterers to be grouped together. In this way, the effective scattering strength of the disordered medium can be enhanced, whereas the isolated small scatterers are relatively weakly scattering. Larger scattering objects would have more impact on the field such that the optimization could be completed with fewer iterations or smaller shifts. Additionally, the algorithm could be easily adjusted to allow a movement only for specific scatterers or to shift only those scatterers which have the highest impact on the minimal  $S$ -matrix eigenvalue.

## 6.2 Degenerate cavity anti-laser<sup>13</sup>

The CPA systems which have been considered so far can absorb only a very specific input state at a time. For actual applications, however, it would be highly desirable to have the ability of absorbing several input states simultaneously. While recent works

<sup>13</sup> The idea for this project was conceived by Ori Katz and Stefan Rotter. The experiments were carried out by Yevgeny Slobodkin and Gil Weinberg under the supervision of Ori Katz. The numerical simulations were performed by Helmut Hörner, who treated this topic in detail in the course of his diploma thesis [156], which I supervised. Results and figures are taken from our joint publication [157].

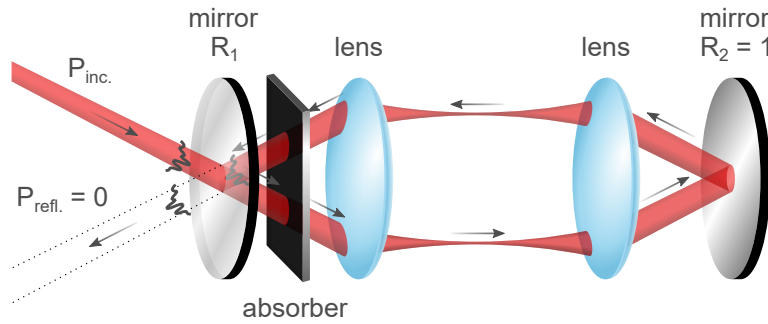


**Figure 6.4:** Concept of a degenerate cavity anti-laser. A weak absorber is located in a degenerate cavity consisting of two lenses placed between a partially reflective ( $R_1 < 1$ ) and a perfect mirror ( $R_2 = 1$ ). The lenses are arranged in an imaging telescope configuration such that after one round trip the field is imaged onto itself. At certain frequencies, input states with an arbitrary wavefront can be perfectly absorbed such that the reflected power of the incoming signal vanishes.

have managed to merge two perfectly absorbed modes at an exceptional point [100–102], all of the possibly many other modes would in such a case be only weakly absorbed because of the different interference patterns created by them. As we show in this section, it is possible to remove this limitation of the number of CPA modes entirely to absorb an incoming signal at a given frequency but with arbitrary wavefront if the system is built in the form of a degenerate cavity [158], which is a resonator with the property that an arbitrary ray retraces its own path after a full round trip. Therefore, this kind of cavity features a degenerate spectrum of resonance frequencies, meaning that a large number of modes can simultaneously satisfy the resonance condition. One possible realization of a degenerate cavity is shown in fig. 6.4. It consists of two identical converging lenses placed between two mirrors forming the resonator. The key property of this system is that the distance between the lenses is precisely twice the focal length  $f$  so that their focal points coincide in the center. Furthermore, the distance from the surrounding mirrors to the next lens is equal to one focal length, which makes a total system extent of four focal lengths. For that reason, this configuration is also referred to as  $4f$ -cavity. By placing a critically coupled absorber inside the cavity, it is feasible (at certain resonance frequencies) to achieve perfect absorption of an input state with arbitrary wavefront and incident angle to let the outgoing power vanish.

An experimental realization of such a massively degenerate coherent perfect absorber [157] is illustrated in fig. 6.5a. Light from a wavelength-stabilized helium-neon laser is directed onto a  $4f$ -cavity, where the incoming wavefront can be controlled with the help of a spatial light modulator, and the spatial intensity distribution of the reflected signal is measured by a camera. A piezo stage nanopositioner is used for a fine tuning of the cavity length. To demonstrate the versatile absorption capability of this system, a complex input field in the form of a speckled yin-yang symbol is injected. The intensity profile of the measured reflection signal when the cavity length is tuned to minimal absorption is depicted in fig. 6.5b. By adjusting the cavity length, the reflected power can

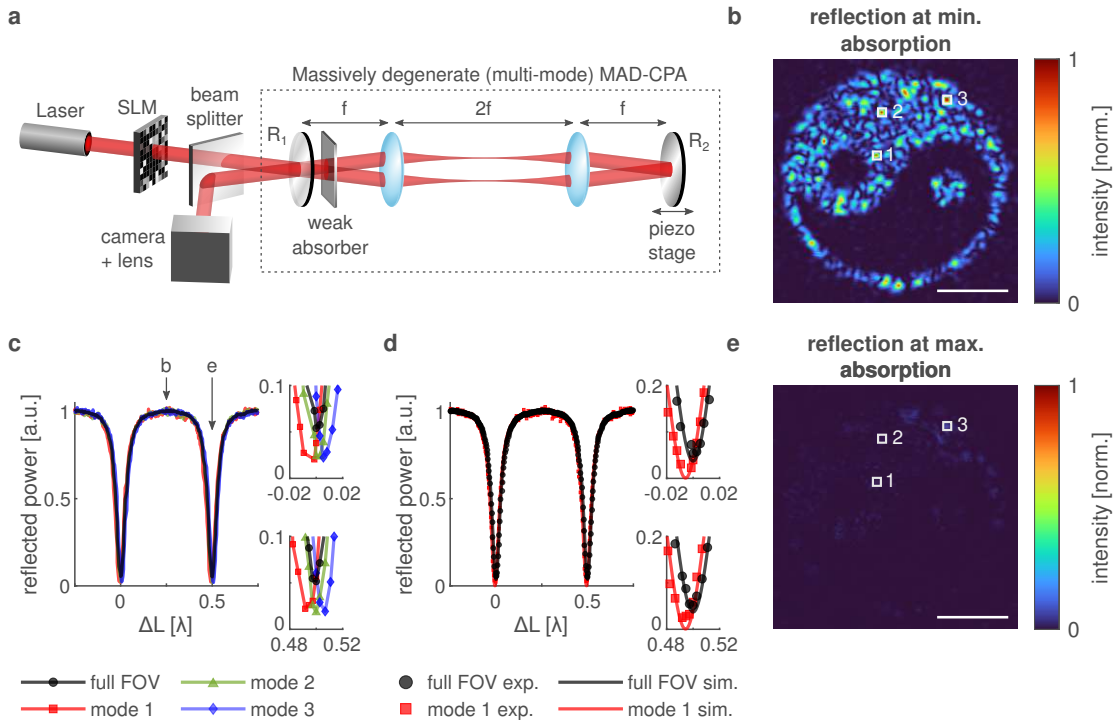


**Figure 6.5:** Experimental setup and results for a degenerate cavity anti-laser. (a) The signal from a wavelength-stabilized laser is controlled using a spatial light modulator (SLM) and injected into a degenerate cavity containing a critically coupled weak absorber. The spatial intensity profile of the reflected light is captured with a camera. (b) Reflected intensity distribution from an input field in the form of a speckled yin-yang symbol composed of more than 1000 modes, where the cavity length is tuned for minimal absorption. (c) Dependence of the reflected power on the cavity length  $L$  (in units of the wavelength  $\lambda$ ) measured for the full field of view (FOV) as well as for three individual localized modes (speckle grains) marked by white squares in (b) and (e). (d) Same experimental measurements as in (c) for the total reflected power and for a single mode, together with the numerical prediction for an input of 100 modes. (e) Measured reflected intensity distribution of the input signal from (b) when the cavity-length is tuned for maximum absorption. Scale bars represent a length of 1 mm.

be minimized when the resonance condition  $L = m\lambda/2$  is met, where  $L$  is the single-pass optical path length and  $m \in \mathbb{N}$ . At these resonant positions, close to perfect absorption is measured, which is shown in [fig. 6.5c](#) for three exemplary modes (i.e., speckle grains) as well as for the full field of view. In [fig. 6.5d](#), the measured reflected power is compared to numerical simulations for a 100-mode input, where an excellent agreement between the experimental data and the theoretical model can be observed. The intensity distribution for the cavity length being tuned to maximal absorption can be found in [fig. 6.5e](#).

Our numerical simulations, which are thoroughly explained in ref. [156], are based on scalar Fourier optics. Taking into account the optical elements in the system as well as the free propagation in the space between them, the transmission matrix  $T_{\text{st}}$  for a single round trip can be calculated. The total cavity reflection matrix  $R_{\text{cav}}$  is then given by the sum of the directly reflected portion of light plus the contributions from the infinite

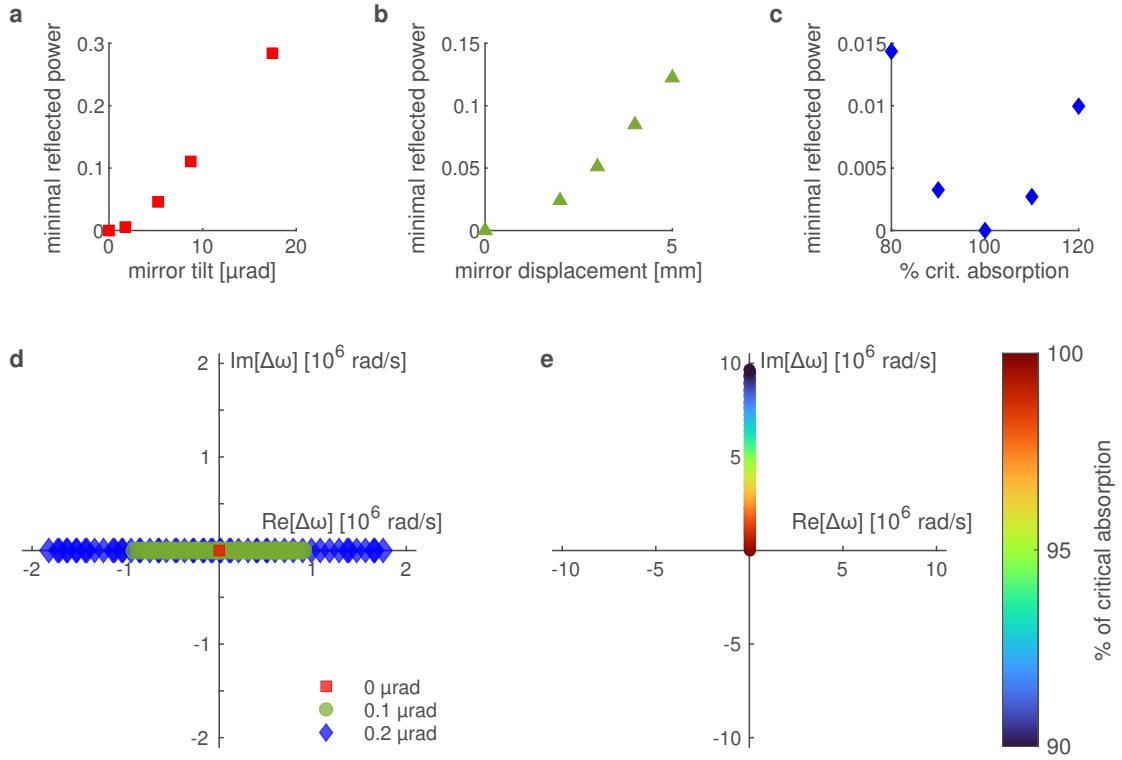


**Figure 6.6:** Numerical study of the sensitivity of the degenerate cavity anti-laser to adjustment errors. The top plots show the effect of deviations from the optimal configuration on the minimal reflected power when the rear cavity mirror is tilted (a) or shifted (b), or when the loss of the absorber is detuned from the critical value (c). The bottom plots illustrate the movement of the degenerate zeros of the CPA reflection matrix in the complex frequency plane when either the rear cavity mirror is slightly tilted (d), or when the absorption strength becomes sub-critical (e). Simulation parameters:  $f = 75$  mm,  $\lambda = 633$  nm,  $R_1 = 70\%$ ,  $R_2 = 100\%$ .

number of round trips inside the cavity, which can be written as

$$R_{\text{cav}} = r\mathbb{1} + t^2 T_{\text{srt}} \left( \mathbb{1} + rT_{\text{srt}} + r^2 T_{\text{srt}}^2 + \dots \right), \quad (6.2)$$

where  $r$  and  $t$  are the complex-valued reflection and transmission coefficients of the partially reflective front mirror. Generalizing the scalar geometric series formula to matrix calculations finally yields

$$R_{\text{cav}} = r\mathbb{1} + t^2 T_{\text{srt}} \sum_{i=0}^{\infty} (rT_{\text{srt}})^i = r\mathbb{1} + t^2 T_{\text{srt}} (\mathbb{1} - rT_{\text{srt}})^{-1}. \quad (6.3)$$

To point out the importance of a precise adjustment of the experimental setup, we perform numerical simulations in which one of the system parameters is detuned while all others stay at the optimal values as required for perfect absorption (see [fig. 6.6](#)). The results confirm that the absorption efficiency of the system is very sensitive to

deviations from optimal positions of the cavity mirrors or lenses, as well as from the critical absorption. Furthermore, it can be seen that tilting one of the cavity mirrors causes the zeros of the cavity reflection matrix to be spread out on the real axis, whereas reducing the amount of loss in the absorber lets them move upwards in the complex frequency plane. This sensitivity, in particular with respect to a mirror tilt, makes the alignment of all system components to achieve perfect absorption highly challenging. On the contrary, this property opens up interesting fields of applications, e.g., for sensing or high-precision measurements.

### 6.3 Scattering suppression from imperfect absorbers<sup>14</sup>

The effect of coherent perfect absorption relies on a precise tuning of the system and signal parameters. Even very small deviations from optimal parameter settings can result in a significant deterioration of the absorption efficiency. As soon as only one of the system or signal parameters is detuned from the CPA configuration, the  $S$ -matrix zero corresponding to the CPA state is no longer located at the real frequency axis but rather shifted upwards or downwards in the complex frequency plane. As we have shown in [chapter 5](#), however, the  $S$ -matrix zeros can also be directly engaged by implementing complex signal frequencies. This phenomenon can be used to transiently suppress the scattered signal from an under- or overdamped CPA.

To illustrate the principle of this technique, we apply it to the simple CPA depicted in [fig. 4.3b](#). In the first case, we decrease the attenuation in the absorber by 50% as compared to the critical value, which results in a non-vanishing outgoing signal. To take the subcritical loss into account for suppressing the outgoing signal, a corresponding imaginary part is added to the signal frequency, which then has a value of  $\omega = 8.384 + 0.116 i$  (arbitrary units). As can be seen in [fig. 6.7a](#), this leads to a completely vanishing outgoing signal again. Since the loss in the absorber is lower than the critical value of the CPA, only part of the incoming energy is absorbed while another part is temporarily stored inside the structure as already discussed in the context of coherent virtual absorption. Therefore, this process can be interpreted as a combination of the CPA and CVA principles.

Analogously to the case of subcritical loss, one can also suppress the outgoing signal for the case of supercritical loss. Increasing the absorption in the system by 50% as compared to the critical value, we find an optimal frequency of  $\omega = 8.384 - 0.116 i$  (arbitrary units) for vanishing output (see [fig. 6.7b](#)). In this situation, the corresponding  $S$ -matrix zero lies below the real axis in the lower half of the complex frequency plane, i.e., the imaginary part of the optimal frequency is negative. In contrast to an underdamped absorber, however, a system with supercritical loss actually absorbs the entire incoming energy if the process is maintained for a sufficiently long time. Due to the exponentially decreasing signal amplitude, the field inside the absorber approaches zero with increasing

<sup>14</sup> The theoretical framework for the content of this section is based on the Bachelor theses [152, 153] of Andrea Pupi c and Thomas Ranner, whose projects on this topic I supervised. Part of the numerical code for the simulations was provided by Matthias K hmayer.

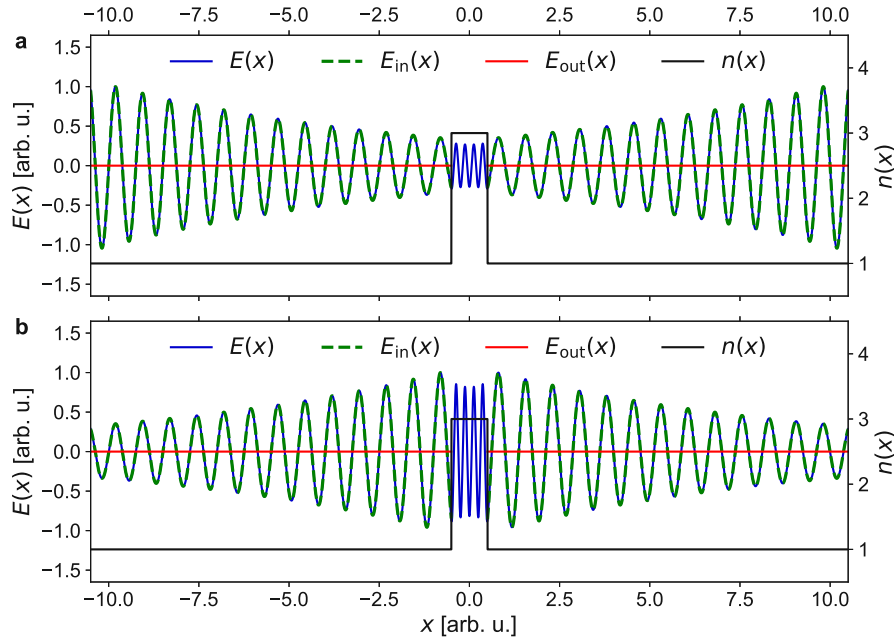


**Figure 6.7:** Suppression of the scattered signal from a detuned CPA by temporal modulation of the signal amplitude, (a) Electric field of a CPA state in a system with subcritical loss, which is compensated by increasing the signal amplitude exponentially in time. (b) Corresponding plot for a system with supercritical loss, where the scattering can be suppressed for a signal whose amplitude decreases exponentially in time.

time. A limiting restriction for an experimental realization is the initially large signal amplitude, which also means that in the beginning of such an experiment there would be a large outgoing field during the transient scattering of the first waves impinging on the absorber until a stationary state is reached.

The approach of suppressing the scattered waves from imperfect absorbers by using complex frequencies can be easily generalized to multi-dimensional systems. As an example, we consider again the random anti-laser system from [section 4.2](#) with the disordered medium consisting of 60 small scatterers. Similar as discussed for the simple one-dimensional system before, we decrease or increase the loss of the absorbing antenna by 25% from the critical value and optimize the signal frequency to minimize the outgoing power. In both cases, it is possible to achieve a vanishing minimal  $S$ -matrix eigenvalue, i.e.,  $|\lambda_{\min}| < 10^{-6}$ . The variation of the parameter values together with the resulting minimal  $S$ -matrix eigenvalue is documented in [table 6.1](#).

**Table 6.1:** Suppression of the scattered signal from a detuned CPA by temporal modulation of the signal amplitude. The table shows the absolute value of the minimal  $S$ -matrix eigenvalue  $|\lambda_{\min}|$  for different parameter configurations of the refractive index  $n_{\text{ant}}$  of the absorbing scatterer (representing the central antenna) and the signal frequency  $\omega$ .

configuration	$n_{\text{ant}}$	$\omega$ [arb. u.]	$ \lambda_{\min} $
CPA	$3.013 + 1.037 i$	148.612	$< 10^{-6}$
subcritical loss	$3.013 + 0.778 i$	148.612	0.190
suppressed scattering	$3.013 + 0.778 i$	$148.400 + 0.599 i$	$< 10^{-6}$
supercritical loss	$3.013 + 1.296 i$	148.612	0.145
suppressed scattering	$3.013 + 1.296 i$	$149.315 - 0.692 i$	$< 10^{-6}$

## 6.4 Perfect absorption of electromagnetic pulses<sup>15</sup>

Coherent perfect absorption and coherent virtual absorption are steady-state phenomena that work only for well-defined signal frequencies. The perfect absorption of an electromagnetic pulse, on the other hand, is a highly nontrivial process since the spectrum of a pulsed signal contains a large number of frequency components which would have to be perfectly absorbed simultaneously. Although several concepts of enhanced broadband absorption have been presented [112–114], the complete absorption of a pulsed signal remained out of reach so far. One possible strategy to optimize the absorption of a polychromatic input state could be to engineer the structure of a disordered medium, similar to the algorithm explained in section 6.1. However, with a growing number of injected frequency components, the optimization procedure would become increasingly complex. Here we propose a scheme to enhance the absorption of specifically constructed pulses based on a dynamical tuning of the loss in the system.

As a starting point, we recapitulate our findings from chapter 5, where we have seen that the scattering from a lossless system can be suppressed if the incoming signal features an exponentially increasing amplitude. Consequently, we demand that the leading edge of the pulse to be absorbed has an exponentially increasing envelope ( $\omega_1 = \omega_1^{(\text{CVA})} > 0$ ) for  $t < 0$ . To achieve a complete pulse, we then change the imaginary part of the signal frequency linearly over time from the CVA value  $\omega_1 = \omega_1^{(\text{CVA})}$  to the negative CVA value  $\omega_1 = -\omega_1^{(\text{CVA})}$  during the time interval  $0 \leq t \leq t_1$ . For  $t > t_1$ , the imaginary part of the frequency is kept constant at  $\omega_1 = -\omega_1^{(\text{CVA})}$  such that the trailing edge of the pulse decreases exponentially in time. To illustrate the effect of such a pulse, we inject it from both sides into the system from fig. 5.1b, i.e., into a plane layer of a dielectric material with refractive index  $n = 3$ . The incoming and outgoing fields for this configuration are depicted in fig. 6.8a. As soon as the signal form deviates from the exponentially increasing wave as required for a CVA (in the example here at  $t = 0$ ),

<sup>15</sup> The theoretical framework for the content of this section was developed together with Andrea Pupić, who treated this topic in the course of a project work [159] that I supervised.



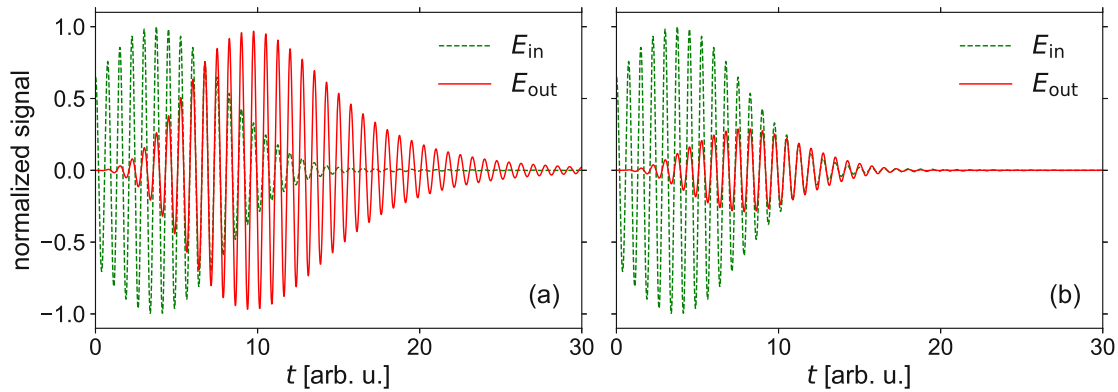


**Figure 6.8:** Absorption of an electromagnetic pulse. (a) Simulation of the incoming and outgoing field of an electromagnetic pulse impinging on a lossless structure (evaluated right in front of the edge of the system). For  $t < 0$ , the amplitude of the incoming signal increases exponentially in time such that the outgoing signal vanishes. (b) Corresponding simulation for an absorber in which the loss is gradually increased while the imaginary part of the signal frequency is decreased.

the stored energy is released from the structure and leaves the system in the form of an outgoing pulse. The total outgoing energy equals to the total injected energy as there is no loss in this system.

As demonstrated in [section 6.3](#), the scattering of an incoming signal can be suppressed if the imaginary part of the signal frequency is matched to the actual degree of dissipation in the system. In the next step, we therefore introduce loss into this system in such a way that the attenuation dynamically increases linearly in time to maintain the critical value of loss corresponding to the actual value of  $\omega_1(t)$  in the time frame  $0 \leq t \leq t_1$ . The simulation results for this simplified dynamical loss adjustment are presented in [fig. 6.8b](#). As compared to the case without loss, the amplitude of the outgoing pulse is strongly reduced as part of the signal is absorbed inside the structure. Since the pulse energy is proportional to the temporal integral of the squared field, it turns out that about 93% of the injected energy is absorbed by the system.

Although for each time the loss and the imaginary part of the signal frequency are aligned as required for a vanishing outgoing signal in steady-state operation, the pulse is not perfectly absorbed. The reason for this behavior is that the system would require a certain settling time after each parameter change to reach a stationary state again. To deal with this problem, one could perform the variation of the signal and system parameters (almost) adiabatically. However, this would heavily increase the pulse duration. Another possibility to improve the absorption efficiency for an electromagnetic pulse would be to optimize the exact form of the temporal modulation of the loss in the absorber to compensate the transient emission. Such an optimization procedure, however, shall be left as an open task for further studies.



# Chapter 7

## Conclusion and Outlook

In summary, we have discussed various effects associated with generalizations of the lasing principle to novel domains, such as phonon lasing and the time-reversal of lasing at threshold.

In the first part of this thesis, we have discussed that the principle of stimulated emission can be extended to quanta beyond photons, which led us to the concept of a phonon laser. We have explicitly discussed an experimental setup consisting of two whispering-gallery-mode microresonators, one of which also supports mechanical oscillations. By tuning the system parameters (specifically by introducing additional loss in one of the resonators), it was possible to induce an exceptional point (EP) in the two optical modes, which form the two-level system that underlies the stimulated phonon emission. With the help of this compound phonon laser system, we could clarify the long-debated issue of what happens to the linewidth of a laser when it is operated at an EP [24]. In accordance with early theoretical work on this subject, we found a significant broadening of the phonon laser linewidth in the vicinity of the EP. This broadening can be attributed to excess noise due to the maximized non-orthogonality of the two optical modes when they are steered to an EP, i.e., when they become parallel. Moreover, we observed a sudden drop of the phonon laser threshold as another signature of the EP in the optical part of the system. This is a result of the spatial distribution of the two optical modes over the resonators, whose characteristics change dramatically when the system is steered through the EP by increasing the additional loss in the purely optical resonator.

The remaining part of this dissertation was devoted to the perfect absorption of electromagnetic signals. By time-reversing the process of lasing at threshold, the concept of coherent perfect absorption was introduced. Based on a scattering matrix analysis, we managed to generalize this effect to disordered media and complex scattering systems. This was presented in the framework of a microwave experiment which represents the first implementation of a random anti-laser [91]. Since our approach solely relies on the accessibility of the scattering matrix, which can be conveniently measured in the far-field of the scattering system, no information about the exact system structure nor any near-field measurements are required. This property makes us confident that our method could be a basis for promising applications in various fields like, e.g., telecommunications or radiotherapy. Moreover, we have indicated that coherent perfect absorbers (CPAs) can also be a relevant tool for focusing beyond the diffraction limit. Although we could not directly visualize this effect in our random anti-laser experiment,

the sub-wavelength focusing feature of a CPA could lead to considerable advances in medical and industrial imaging techniques by significantly reducing the focal spot size. However, it must be noted that the currently available measuring technologies will also require further improvement in order to provide the necessary scattering information in real time, especially for applications in a dynamically changing environment.

Nevertheless, we have developed several methods to enhance the versatility of CPAs for technical applications. As a first improvement, we have demonstrated how a specific signal with predefined frequency or wavefront can be perfectly absorbed if the geometric structure of the system is optimized. While it turned out that in simple (quasi-one-dimensional) geometries the optimal system parameters can be straightforwardly calculated, we could also show that even in a disordered medium a customized signal can be perfectly absorbed if only a few scatterers are properly shifted. Moreover, the concept of a degenerate cavity anti-laser was introduced [157]. As demonstrated both theoretically and experimentally, such a device offers the possibility to perfectly absorb signals with arbitrary wavefront at a given frequency. With the help of the toolbox provided by the aforementioned methods, we are now in the position to design customized CPAs for arbitrary monochromatic input signals.

Besides coherent *perfect* absorption, we have also discussed the phenomenon of coherent *virtual* absorption. In this process, where one of the scattering matrix zeros is directly engaged in the complex frequency plane, the entire energy of the incident signal is temporarily stored inside the system while all backscattered signal components are canceled out by destructive interference. Therefore, this effect enables efficient and flexible energy storage over short periods of time, i.e., as long as the exponential growth of the incoming signal can be maintained. Similar as for CPAs, however, coherent virtual absorption has been investigated only in rather simple geometries in previous publications. In analogy to our random anti-laser, we have demonstrated in this work that coherent virtual absorption can also be achieved in disordered media. As we have further shown, the concepts of coherent perfect absorption and coherent virtual absorption can be combined in order to transiently suppress the scattered signal components from a detuned CPA. Finally, we have proposed a procedure for the perfect absorption of electromagnetic pulses by dynamically tuning the system's absorption strength.

Based on the methods and results presented in this thesis, we believe that we could contribute another interesting piece in the mosaic of the comprehensive field of non-Hermitian physics. Nobody knows what fascinating discoveries the future will reveal, but (exotic) lasers and anti-lasers may very well play an essential role in it.

# Appendix

## A Phonon laser analysis

### A.1 Quantum Langevin equations

In real experiments, a system is never completely isolated from its environment but is always at least weakly coupled to secondary degrees of freedom which are commonly referred to as a *heat bath* [128, 129]. For many problems in quantum optics, the bath can be modeled as a continuum of harmonic oscillators. Assuming that both the system and the bath evolve at a frequency scale of  $\omega_0$ , the Hamiltonian of the bath is given by

$$\hat{H}_{\text{bath}} = \int_{\omega_0 - \Delta\omega}^{\omega_0 + \Delta\omega} d\omega \hbar\omega \hat{b}_\omega^\dagger \hat{b}_\omega, \quad (\text{A.1})$$

where  $\Delta\omega$  is the bandwidth of the bath and the bosonic bath operators  $\hat{b}_\omega$  obey the commutation relation

$$[\hat{b}_\omega, \hat{b}_{\omega'}^\dagger] = \delta(\omega - \omega'). \quad (\text{A.2})$$

The interaction of the bath with an arbitrary system operator  $\hat{c}$  may be written as

$$\hat{H}_{\text{int}} = i\hbar \int_{\omega_0 - \Delta\omega}^{\omega_0 + \Delta\omega} d\omega g(\omega) (\hat{b}_\omega^\dagger \hat{c} - \hat{c}^\dagger \hat{b}_\omega), \quad (\text{A.3})$$

where  $g(\omega)$  is a frequency-dependent coupling parameter. An arbitrary system (with Hamiltonian  $\hat{H}_{\text{sys}}$ ) coupled to a heat bath is thus described by the full Hamiltonian

$$\hat{H} = \hat{H}_{\text{sys}} + \hat{H}_{\text{bath}} + \hat{H}_{\text{int}}. \quad (\text{A.4})$$

From eq. (A.4) we can now derive the Heisenberg equations of motion for the bath operators  $\hat{b}_\omega$  as well as for an arbitrary system operator  $\hat{a}$ :

$$\dot{\hat{b}}_\omega = \frac{i}{\hbar} [\hat{H}, \hat{b}_\omega] = -i\omega \hat{b}_\omega + g(\omega) \hat{c}, \quad (\text{A.5})$$

$$\dot{\hat{a}} = \frac{i}{\hbar} [\hat{H}, \hat{a}] = \frac{i}{\hbar} [\hat{H}_{\text{sys}}, \hat{a}] - \int_{\omega_0 - \Delta\omega}^{\omega_0 + \Delta\omega} d\omega g(\omega) (\hat{b}_\omega^\dagger [\hat{c}, \hat{a}] - [\hat{c}^\dagger, \hat{a}] \hat{b}_\omega). \quad (\text{A.6})$$

Formally integrating eq. (A.5) yields a solution for  $\hat{b}_\omega$ ,

$$\hat{b}_\omega(t) = \hat{b}_\omega(0) e^{-i\omega t} + g(\omega) \int_0^t ds \hat{c}(s) e^{-i\omega(t-s)}, \quad (\text{A.7})$$

which can be substituted into eq. (A.6) to obtain

$$\begin{aligned} \dot{\hat{a}} = & \frac{i}{\hbar} [\hat{H}_{\text{sys}}, \hat{a}] - \int_{\omega_0 - \Delta\omega}^{\omega_0 + \Delta\omega} d\omega g(\omega) \left( \hat{b}_\omega^\dagger(0) e^{i\omega t} [\hat{c}, \hat{a}] - [\hat{c}^\dagger, \hat{a}] \hat{b}_\omega(0) e^{-i\omega t} \right) \\ & - \int_{\omega_0 - \Delta\omega}^{\omega_0 + \Delta\omega} d\omega (g(\omega))^2 \int_0^t ds \left( \hat{c}^\dagger(s) e^{i\omega(t-s)} [\hat{c}, \hat{a}] - [\hat{c}^\dagger, \hat{a}] \hat{c}(s) e^{-i\omega(t-s)} \right). \end{aligned} \quad (\text{A.8})$$

While eq. (A.8) is still exact, we can further simplify it with the so-called *Markov approximation*. To this end, we assume that the system-bath coupling is independent of frequency within the bandwidth of the bath, i.e.,  $g(\omega) \equiv g(\omega_0)$ . Further we assume that the bath correlation time (i.e., the inverse bandwidth) is short enough such that  $c(s)$  contributes only for short times to the last integral in eq. (A.8) and we can replace the actual system evolution by the free evolution

$$c(s) \approx c(t) e^{i\omega_0(t-s)}, \quad (\text{A.9})$$

which yields integrals of the form

$$\begin{aligned} & - (g(\omega_0))^2 [\hat{c}^\dagger, \hat{a}] \hat{c}(t) \int_0^t ds \underbrace{\int_{\omega_0 - \Delta\omega}^{\omega_0 + \Delta\omega} d\omega e^{-i(\omega - \omega_0)(t-s)}}_{\approx 2\pi\delta(t-s)} \\ & = - 2\pi (g(\omega_0))^2 [\hat{c}^\dagger, \hat{a}] \hat{c}(t) \underbrace{\int_0^t ds \delta(t-s)}_{=1/2}. \end{aligned} \quad (\text{A.10})$$

By defining the operator decay rate  $\gamma := \pi (g(\omega_0))^2$  and the in-field

$$\hat{b}_{\text{in}}(t) := \frac{1}{\sqrt{2\pi}} \int_{\omega_0 - \Delta\omega}^{\omega_0 + \Delta\omega} d\omega \hat{b}_\omega(0) e^{-i\omega t}, \quad (\text{A.11})$$

which satisfies the commutator relation

$$[\hat{b}_{\text{in}}(t), \hat{b}_{\text{in}}^\dagger(t')] = \delta(t - t'), \quad (\text{A.12})$$

we can derive the quantum Langevin equations for any system operator

$$\dot{\hat{a}} = \frac{i}{\hbar} [\hat{H}_{\text{sys}}, \hat{a}] - [\hat{a}, \hat{c}^\dagger] (\gamma \hat{c} + \sqrt{2\gamma} \hat{b}_{\text{in}}(t)) - (\gamma \hat{c}^\dagger + \sqrt{2\gamma} \hat{b}_{\text{in}}^\dagger(t)) [\hat{c}, \hat{a}]. \quad (\text{A.13})$$

For the simple example of  $\hat{a}$  being a harmonic oscillator operator, we can identify  $\hat{c} \equiv \hat{a}$  in eq. (A.13) and obtain the quantum Langevin equation of a damped harmonic oscillator,

$$\dot{\hat{a}} = -i\omega_0\hat{a} - \gamma\hat{a} + \hat{\Gamma}, \quad (\text{A.14})$$

where we have defined the noise operator  $\hat{\Gamma} := -\sqrt{2\gamma}\hat{b}_{\text{in}}$ .

## A.2 Derivation of the phonon laser threshold

While the threshold pump power of our phonon laser system can be easily calculated numerically (see appendix A.3), we want to derive an analytical approximation in order to gain a better understanding of the relevant physics in the vicinity of the EP. The starting point for our analysis is the c-number version of the system equations [24, 117]

$$\dot{a}_1(t) = (i\Delta - \gamma_1)a_1(t) - ika_2(t) + igx_0a_1(t)(b(t) + b^*(t)) + \Omega + \Gamma_1(t), \quad (\text{A.15})$$

$$\dot{a}_2(t) = (i\Delta - \gamma_2)a_2(t) - ika_1(t) + \Gamma_2(t), \quad (\text{A.16})$$

$$\dot{b}(t) = (-i\omega_m - \gamma_m)b(t) + igx_0a_1^*(t)a_1(t) + \Gamma_b(t). \quad (\text{A.17})$$

As already derived in section 2.3.2, the optical inter-resonator coupling gives rise to the formation of two supermodes, which can be written as

$$a_{\pm}(t) = \frac{1}{N_{\pm}} [(i\gamma \pm \beta)a_1(t) + \kappa a_2(t)], \quad (\text{A.18})$$

where we have used the abbreviations  $\gamma := (\gamma_2 - \gamma_1)/2$  and  $\beta := \sqrt{\kappa^2 - \gamma^2}$ , as well as the normalization constants

$$N_{\pm} = \begin{cases} \sqrt{2}\kappa & \text{if } \kappa^2 \geq \gamma^2 \\ \sqrt{\kappa^2 + (\gamma \pm \sqrt{\gamma^2 - \kappa^2})^2} & \text{if } \kappa^2 < \gamma^2 \end{cases}. \quad (\text{A.19})$$

With the help of eq. (A.18), the cavity modes  $a_1$  and  $a_2$  can be expressed in terms of the supermodes  $a_+$  and  $a_-$  according to

$$a_1(t) = \frac{1}{2\beta} [N_+a_+(t) - N_-a_-(t)], \quad (\text{A.20})$$

$$a_2(t) = \frac{1}{2\beta\kappa} [(\beta - i\gamma)N_+a_+(t) + (\beta + i\gamma)N_-a_-(t)]. \quad (\text{A.21})$$

By inserting eqs. (A.20) and (A.21) into eq. (2.15), the system Hamiltonian can be expressed in the supermode basis, from which we can derive the dynamical equations for the supermodes, where we have to distinguish between the cases before and after the EP.

### Strong coupling regime

In the regime before the EP (strong coupling,  $\kappa^2 \geq \gamma^2$ ), the term  $\beta := \sqrt{\kappa^2 - \gamma^2}$  is real and the supermodes feature different frequencies  $\omega_{\pm} = \omega_c \pm \beta$  but equal decay rates  $\gamma_{\pm} = \chi := (\gamma_1 + \gamma_2)/2$ . The system equations in the supermode representation are derived as

$$\dot{a}_+ = [i(\Delta - \beta) - \chi] a_+ + \frac{gx_0(\gamma - i\beta)}{2\beta} a_- b + \frac{i\gamma + \beta}{\sqrt{2}\kappa} \Omega, \quad (\text{A.22})$$

$$\dot{a}_- = [i(\Delta + \beta) - \chi] a_- - \frac{gx_0(\gamma + i\beta)}{2\beta} a_+ b^* + \frac{i\gamma - \beta}{\sqrt{2}\kappa} \Omega, \quad (\text{A.23})$$

$$\dot{b} = (-i\omega_m - \gamma_m) b - \frac{igx_0\kappa^2}{2\beta^2} a_-^* a_+, \quad (\text{A.24})$$

where we have dropped the temporal dependence for better readability. For the derivation of eqs. (A.22) to (A.24), we have neglected the self-frequency-shift terms proportional to  $\hat{a}_+^\dagger \hat{a}_+ (\hat{b} + \hat{b}^\dagger)$  and  $\hat{a}_-^\dagger \hat{a}_- (\hat{b} + \hat{b}^\dagger)$  and also the non-resonant terms proportional to  $\hat{a}_-^\dagger \hat{a}_+ \hat{b}$  and  $\hat{a}_+^\dagger \hat{a}_- \hat{b}^\dagger$  in the system Hamiltonian, as well as the noise terms. One can already see from eqs. (A.22) to (A.24) that the effective optomechanical coupling is strongly enhanced in the vicinity of the EP where  $\beta \rightarrow 0$ . In fact, the unphysical divergence of the effective optomechanical coupling directly at the EP ( $\beta = 0$ ) indicates that more terms are required to describe this parameter regime correctly.

In analogy to the procedure in standard laser theory [9], we introduce the ladder operators  $\hat{J}_+ := \hat{a}_+^\dagger \hat{a}_-$  and  $\hat{J}_- := \hat{a}_-^\dagger \hat{a}_+$  as well as the population inversion operator  $\hat{J}_z := \hat{a}_+^\dagger \hat{a}_+ - \hat{a}_-^\dagger \hat{a}_-$ . The dynamical equations for these quantities follow directly from eqs. (A.22) to (A.24) and can be written as

$$\dot{J}_+ = -2(\chi - i\beta) J_+ - \frac{gx_0(\gamma + i\beta)}{2\beta} J_z b^*, \quad (\text{A.25})$$

$$\dot{J}_- = -2(\chi + i\beta) J_- - \frac{gx_0(\gamma - i\beta)}{2\beta} J_z b, \quad (\text{A.26})$$

$$\dot{J}_z = -2\chi J_z + \frac{gx_0(\gamma + i\beta)}{\beta} J_- b^* + \frac{gx_0(\gamma - i\beta)}{\beta} J_+ b + \Lambda, \quad (\text{A.27})$$

$$\dot{b} = (-i\omega_m - \gamma_m) b - \frac{igx_0\kappa^2}{2\beta^2} J_-, \quad (\text{A.28})$$

where  $\Lambda$  is the effective driving acting on the two-level system, which is given by

$$\Lambda = [(\beta + i\gamma)(\bar{a}_+^* + \bar{a}_-) + (\beta - i\gamma)(\bar{a}_+ + \bar{a}_-^*)] \frac{\Omega}{\sqrt{2}\kappa}, \quad (\text{A.29})$$

with the quantities  $\bar{a}_{\pm}$  denoting the stationary values of the supermodes  $a_{\pm}$ . Note that we have omitted the driving acting on the dynamics of  $J_+$  and  $J_-$  because we assume that the total population of the two energy levels  $\hat{n}_+ + \hat{n}_- = \hat{a}_+^\dagger \hat{a}_+ + \hat{a}_-^\dagger \hat{a}_-$  is conserved. After performing a rotating frame transformation by substituting  $b \rightarrow b \exp(-i\omega_m t)$ ,



$J_- \rightarrow J_- \exp(-i\omega_m)$ , and  $J_+ \rightarrow J_+ \exp(i\omega_m)$ , and using the fact that  $\gamma_m \ll \chi$ , one can adiabatically eliminate the degrees of freedom of the optical modes by setting  $\dot{J}_- = 0$ , which yields

$$J_- = \frac{gx_0(i\beta - \gamma)J_z}{2\beta[2\chi + i(2\beta - \omega_m)]}b. \quad (\text{A.30})$$

By inserting eq. (A.30) into eq. (A.28) we obtain the following equation for the phonon mode in the rotating frame,

$$\dot{b} = -\gamma_m b + \frac{i(gx_0)^2(\gamma - i\beta)\kappa^2 J_z}{4\beta^3[2\chi + i(2\beta - \omega_m)]}b, \quad (\text{A.31})$$

from which one can see that the optical modes induce an effective mechanical gain of

$$G = \text{Re} \left\{ \frac{i(gx_0)^2(\gamma - i\beta)\kappa^2 J_z}{4\beta^3[2\chi + i(2\beta - \omega_m)]} \right\} = \frac{(gx_0)^2[2\beta\chi + \gamma(2\beta - \omega_m)]\kappa^2 J_z}{4\beta^3[4\chi^2 + (2\beta - \omega_m)^2]}. \quad (\text{A.32})$$

For an effective pumping of the blue-detuned supermode  $a_+$  and under the assumption of complete inversion such that  $\hat{J}_z \approx \hat{a}_+^\dagger \hat{a}_+$ , the threshold pump power of the phonon laser is approximately given by  $P_{\text{thr}} \approx \chi \hbar \omega_+ a_+^* a_+ \approx \chi \hbar \omega_c J_z$ , where we have also considered that  $\omega_m, \beta \ll \omega_c$  and hence  $\omega_+ \approx \omega_c$ . With these approximations together with the threshold condition  $G = \gamma_m$ , the threshold pump power of the phonon laser in the regime before the EP can be calculated from eq. (A.32) and is given by

$$P_{\text{thr}} = \frac{4\chi \hbar \omega_c \gamma_m \beta^3 [4\chi^2 + (2\beta - \omega_m)^2]}{(gx_0)^2 \kappa^2 [2\beta\chi + \gamma(2\beta - \omega_m)]}. \quad (\text{A.33})$$

### Weak coupling regime

In the regime after the EP (weak coupling,  $\kappa^2 < \gamma^2$ ), the term  $\beta = i\tilde{\beta} := i\sqrt{\gamma^2 - \kappa^2}$  is purely imaginary and the supermodes feature equal frequencies  $\omega_\pm = \omega_c$  but different decay rates  $\gamma_\pm = \chi \mp \tilde{\beta}$ . The system equations in the supermode representation thus read

$$\dot{a}_+ = [i\Delta - (\chi - \tilde{\beta})]a_+ - \frac{igx_0 N_- (\gamma + \tilde{\beta})}{2N_+ \tilde{\beta}} a_- b + \frac{i(\gamma + \tilde{\beta})}{N_+} \Omega, \quad (\text{A.34})$$

$$\dot{a}_- = [i\Delta - (\chi + \tilde{\beta})]a_- + \frac{igx_0 N_+ (\gamma - \tilde{\beta})}{2N_- \tilde{\beta}} a_+ b^* + \frac{i(\gamma - \tilde{\beta})}{N_-} \Omega, \quad (\text{A.35})$$

$$\dot{b} = (-i\omega_m - \gamma_m)b - \frac{igx_0 N_+ N_-}{4\tilde{\beta}^2} a_-^* a_+. \quad (\text{A.36})$$

Similar as in the regime before the EP, we can derive the dynamical equations for the quantities  $J_+$ ,  $J_-$ , and  $J_z$ , introduce the rotating frame  $b \rightarrow b \exp(-i\omega_m)$ ,  $J_- \rightarrow J_- \exp(-i\omega_m)$ , and  $J_+ \rightarrow J_+ \exp(i\omega_m)$ , and adiabatically eliminate the optical degrees of

freedom, which leads to

$$J_- = \frac{igx_0N_+(\tilde{\beta} - \gamma)J_z}{2\tilde{\beta}N_-(2\chi - i\omega_m)}b \quad (\text{A.37})$$

and consequently to

$$\dot{b} = -\gamma_m b - \frac{(gx_0)^2\kappa^2\gamma J_z}{4\tilde{\beta}^3(2\chi - i\omega_m)}b. \quad (\text{A.38})$$

From eq. (A.38) we can again derive the mechanical gain due to the optomechanical interaction, which results in

$$G = \text{Re} \left\{ -\frac{(gx_0)^2\kappa^2\gamma J_z}{4\tilde{\beta}^3(2\chi - i\omega_m)} \right\} = -\frac{(gx_0)^2\kappa^2\gamma\chi J_z}{2\beta^3(4\chi^2 + \omega_m^2)}. \quad (\text{A.39})$$

However, the corresponding threshold pump power

$$P_{\text{thr}} = -\frac{2\hbar\omega_c\gamma_m\tilde{\beta}^3(4\chi^2 + \omega_m^2)}{(gx_0)^2\kappa^2\gamma} \quad (\text{A.40})$$

would then become negative in the parameter regime under consideration, which clearly indicates that the approximations made for the derivation of eq. (A.40) are not justified in this case. In fact, one of the most critical approximations is to neglect the allegedly non-resonant terms proportional to  $\hat{a}_-^\dagger\hat{a}_+\hat{b}$  and  $\hat{a}_+^\dagger\hat{a}_-\hat{b}^\dagger$  in the system Hamiltonian. In the vicinity of the EP and particularly in the regime after the EP, both supermodes feature the same frequency, which implies that more terms in the system Hamiltonian should be included in the analysis. Taking into account also the terms proportional to  $\hat{a}_-^\dagger\hat{a}_+\hat{b}$  and  $\hat{a}_+^\dagger\hat{a}_-\hat{b}^\dagger$  results in a situation where the denominator in eq. (A.39) vanishes since all terms are canceled out by each other, which corresponds to an infinitely high optomechanical coupling strength. Therefore, we find that the analytical approximation for the threshold pump power of the phonon laser in the regime after the EP is equal to zero,

$$P_{\text{thr}} \equiv 0. \quad (\text{A.41})$$

### A.3 Linear stability analysis

The occurrence of phonon lasing in our system does not only depend on the correct parameter settings but especially on the pump strength  $\Omega$ . A standard way to determine for a given pump power whether the system operates below or above threshold is given by a technique called *linear stability analysis* [160]. A particular solution of a nonlinear system is called *linearly stable* if the linearization of the equations at this solution is of the form

$$\frac{d}{dt}\mathbf{u}(t) = A\mathbf{u}(t), \quad (\text{A.42})$$

where the spectrum of the linear operator  $A$  contains only eigenvalues with negative real part. Otherwise—if one of the eigenvalues has a positive real part—the system is called *linearly unstable*. For our phonon laser, the transition between linear stability and

instability with increasing pump power corresponds to the laser threshold. In order to linearize the system equations, the fields  $a_1(t)$ ,  $a_2(t)$ , and  $b(t)$  are split into a constant steady-state value and a small time-dependent perturbation<sup>16</sup>, i.e.,

$$a_1(t) \rightarrow \bar{a}_1 + \delta a_1(t), \quad (\text{A.43})$$

$$a_2(t) \rightarrow \bar{a}_2 + \delta a_2(t), \quad (\text{A.44})$$

$$b(t) \rightarrow \bar{b} + \delta b(t). \quad (\text{A.45})$$

Inserting eqs. (A.43) to (A.45) into eqs. (A.15) to (A.17) yields the linearized equations

$$\begin{aligned} \frac{d}{dt} (\bar{a}_1 + \delta a_1(t)) &= (i\Delta - \gamma_1) (\bar{a}_1 + \delta a_1(t)) - i\kappa (\bar{a}_2 + \delta a_2(t)) + \Omega \\ &\quad + igx_0 \left[ \bar{a}_1 (\bar{b} + \bar{b}^*) + \bar{a}_1 (\delta b(t) + \delta b^*(t)) + \delta a_1(t) (\bar{b} + \bar{b}^*) \right], \end{aligned} \quad (\text{A.46})$$

$$\frac{d}{dt} (\bar{a}_2 + \delta a_2(t)) = (i\Delta - \gamma_2) (\bar{a}_2 + \delta a_2(t)) - i\kappa (\bar{a}_1 + \delta a_1(t)), \quad (\text{A.47})$$

$$\frac{d}{dt} (\bar{b} + \delta b(t)) = (-i\omega_m - \gamma_m) (\bar{b} + \delta b(t)) + igx_0 (\bar{a}_1^* \bar{a}_1 + \delta a_1^*(t) \bar{a}_1 + \bar{a}_1^* \delta a_1(t)), \quad (\text{A.48})$$

where we have neglected the noise forces and dropped the terms of higher than first order in the perturbations. With the aid of the relation

$$\dot{\bar{a}}_1 = \dot{\bar{a}}_2 = \dot{\bar{b}} = 0, \quad (\text{A.49})$$

the zero-order contribution of eqs. (A.46) to (A.48) can be written as

$$0 = (i\Delta - \gamma_1) \bar{a}_1 - i\kappa \bar{a}_2 + igx_0 \bar{a}_1 (\bar{b} + \bar{b}^*) + \Omega, \quad (\text{A.50})$$

$$0 = (i\Delta - \gamma_2) \bar{a}_2 - i\kappa \bar{a}_1, \quad (\text{A.51})$$

$$0 = (-i\omega_m - \gamma_m) \bar{b} + igx_0 \bar{a}_1^* \bar{a}_1. \quad (\text{A.52})$$

Equations (A.50) to (A.52) represent a closed set of nonlinear equations for the steady-state fields and can be easily solved numerically. The first order equations are then given by

$$\delta \dot{a}_1(t) = (i\Delta - \gamma_1) \delta a_1(t) - i\kappa \delta a_2(t) + \alpha (\delta b(t) + \delta b^*(t)) + \beta \delta a_1(t), \quad (\text{A.53})$$

$$\delta \dot{a}_2(t) = (i\Delta - \gamma_2) \delta a_2(t) - i\kappa \delta a_1(t), \quad (\text{A.54})$$

$$\delta \dot{b}(t) = (-i\omega_m - \gamma_m) \delta b(t) + \alpha^* \delta a_1(t) + \alpha \delta a_1^*(t), \quad (\text{A.55})$$

where we have introduced the abbreviations  $\alpha = igx_0 \bar{a}_1$  and  $\beta = igx_0 (\bar{b} + \bar{b}^*)$ . The values for the steady-state quantities  $\bar{a}_1$  and  $\bar{b}$  can be directly taken from the solution of eqs. (A.50) to (A.52).

<sup>16</sup> Note that this *ansatz* is valid only below threshold as it is demonstrated in ref. [117].

The next step is to define the solution vector

$$\mathbf{u}(t) := \left( \delta a_1(t) \quad \delta a_1^*(t) \quad \delta a_2(t) \quad \delta a_2^*(t) \quad \delta b(t) \quad \delta b^*(t) \right)^T, \quad (\text{A.56})$$

which satisfies eq. (A.42) with the matrix

$$A = \begin{pmatrix} i\Delta - \gamma_1 + \beta & 0 & -i\kappa & 0 & \alpha & \alpha \\ 0 & -i\Delta - \gamma_1 - \beta & 0 & i\kappa & \alpha^* & \alpha^* \\ -i\kappa & 0 & i\Delta - \gamma_2 & 0 & 0 & 0 \\ 0 & i\kappa & 0 & -i\Delta - \gamma_2 & 0 & 0 \\ -\alpha^* & \alpha & 0 & 0 & -i\omega_m - \gamma_m & 0 \\ \alpha^* & -\alpha & 0 & 0 & 0 & i\omega_m - \gamma_m \end{pmatrix}. \quad (\text{A.57})$$

By calculating the eigenvalues of the matrix  $A$ , it can be decided for any given input parameter set whether the system is below or above threshold. The exact value for the threshold pump power can be found by systematically varying the input power and simultaneously evaluating the eigenvalues of the matrix  $A$ .

## B Simulation of electromagnetic waves

### B.1 Wave equation

Electromagnetic fields are described by Maxwell's equations [147, 161], which can be written (in SI units) for an inhomogeneous, linear, and isotropic medium as

$$\nabla \cdot \mathbf{D}(\mathbf{r}, t) = \rho_f(\mathbf{r}, t), \quad (\text{B.1})$$

$$\nabla \cdot \mathbf{B}(\mathbf{r}, t) = 0, \quad (\text{B.2})$$

$$\nabla \times \mathbf{E}(\mathbf{r}, t) = -\frac{\partial}{\partial t} \mathbf{B}(\mathbf{r}, t), \quad (\text{B.3})$$

$$\nabla \times \mathbf{H}(\mathbf{r}, t) = \mathbf{j}_f(\mathbf{r}, t) + \frac{\partial}{\partial t} \mathbf{D}(\mathbf{r}, t), \quad (\text{B.4})$$

with the electric displacement field  $\mathbf{D}(\mathbf{r}, t)$ , the electric field strength  $\mathbf{E}(\mathbf{r}, t)$ , the magnetic flux density  $\mathbf{B}(\mathbf{r}, t)$ , the magnetic field strength  $\mathbf{H}(\mathbf{r}, t)$ , the position vector  $\mathbf{r} = (x, y, z)^\top$ , and the nabla operator denoting the three-dimensional gradient  $(\frac{\partial}{\partial x}, \frac{\partial}{\partial y}, \frac{\partial}{\partial z})^\top$ . The quantities  $\rho_f(\mathbf{r}, t)$  and  $\mathbf{j}_f(\mathbf{r}, t)$  represent the free charge density and the free current density, respectively. For isotropic linear materials, the electromagnetic fields are linked by the constitutive equations

$$\mathbf{D}(\mathbf{r}, t) = \varepsilon_0 \varepsilon_r(\mathbf{r}, t) \mathbf{E}(\mathbf{r}, t), \quad (\text{B.5})$$

$$\mathbf{B}(\mathbf{r}, t) = \mu_0 \mu_r(\mathbf{r}, t) \mathbf{H}(\mathbf{r}, t), \quad (\text{B.6})$$

in which  $\varepsilon_0$  and  $\varepsilon_r(\mathbf{r}, t)$  represent the (scalar<sup>17</sup>) vacuum and relative permittivity, whereas  $\mu_0$  and  $\mu_r(\mathbf{r}, t)$  are the vacuum and relative permeability, respectively. In the following, we consider only static and non-magnetic materials with  $\varepsilon_r(\mathbf{r}, t) = \varepsilon_r(\mathbf{r})$  and  $\mu_r(\mathbf{r}, t) \equiv 1$ . Further, we assume a charge-free medium such that  $\rho_f(\mathbf{r}, t) \equiv 0$ . Under these assumptions and with the help of eqs. (B.4) to (B.6), the application of the curl operator on eq. (B.3) yields the vector wave equation

$$\nabla \times \nabla \times \mathbf{E}(\mathbf{r}, t) + \frac{n^2(\mathbf{r})}{c^2} \frac{\partial^2}{\partial t^2} \mathbf{E}(\mathbf{r}, t) = -\mu_0 \frac{\partial}{\partial t} \mathbf{j}_i(\mathbf{r}, t), \quad (\text{B.7})$$

in which we have introduced the position-dependent refractive index  $n(\mathbf{r}) = \sqrt{\varepsilon_r(\mathbf{r})}$  and replaced the free current density  $\mathbf{j}_f(\mathbf{r}, t)$  by an impressed current density  $\mathbf{j}_i(\mathbf{r}, t)$  that acts as a source for the electric field. The parameter  $c = 1/\sqrt{\varepsilon_0 \mu_0}$  represents the speed of light in vacuum. Analogously to the derivation of the wave equation for the electric field strength  $\mathbf{E}(\mathbf{r}, t)$ , a similar equation can be derived for the magnetic flux density  $\mathbf{B}(\mathbf{r}, t)$ .

For one-dimensional problems, which applies to the time-dependent simulations presented in chapters 5 and 6, the wave equation eq. (B.7) reduces to

$$\frac{\partial^2}{\partial x^2} E(x, t) - \frac{n^2(x)}{c^2} \frac{\partial^2}{\partial t^2} E(x, t) = f(x, t) \quad (\text{B.8})$$

<sup>17</sup> Note that in general the relative permittivity and permeability are tensorial in nature.

for the scalar electric field  $E(x, t)$  with the source term  $f(x, t)$ .

In order to solve eq. (B.8) numerically [162], the spatial and temporal derivatives need to be discretized, which can be done in the following way:

$$\left. \frac{\partial^2 E}{\partial x^2} \right|_{(j \Delta x, n \Delta t)} = \frac{E_{j+1}^n - 2E_j^n + E_{j-1}^n}{\Delta x^2} + \mathcal{O}(\Delta x^2), \quad (\text{B.9})$$

$$\left. \frac{\partial^2 E}{\partial t^2} \right|_{(j \Delta x, n \Delta t)} = \frac{E_j^{n+1} - 2E_j^n + E_j^{n-1}}{\Delta t^2} + \mathcal{O}(\Delta t^2). \quad (\text{B.10})$$

For that purpose, we assume that both space and time are discretized on equidistant grids with step sizes  $\Delta x$  and  $\Delta t$ , respectively. The solution for each point in space and time is then given by  $E_j^n$ , where the subscript  $j$  denotes the spatial position and the superscript  $n$  represents the temporal coordinate, i.e.,  $E_j^n = E(x_j, t_n)$ . With the initial condition that the solution and its temporal derivative are given at time  $t_0$  or equivalently the solution is given at the first two time steps  $t_0$  and  $t_1$ , the solution for all future time steps can be calculated according to the following explicit difference scheme:

$$E_j^{n+1} = R_{j+1}^2 E_{j+1}^n + R_{j-1}^2 E_{j-1}^n + 2(1 - R_j^2) E_j^n - E_j^{n-1} + c^2 \Delta t^2 f_j^n. \quad (\text{B.11})$$

The quantity  $R$  in eq. (B.11) is known as the *Courant number*, which is defined by

$$R_j := \frac{c}{n(x_j)} \frac{\Delta t}{\Delta x}, \quad (\text{B.12})$$

and a necessary condition for the convergence of eq. (B.11) and hence for the stability of the solution is the *Courant-Friedrichs-Lewy criterion*,

$$R_j \leq 1. \quad (\text{B.13})$$

In our simulations we assume an infinitely extended system environment, which is emulated by the application of absorbing boundary conditions [163] according to

$$E_0^{n+1} = E_1^n + \frac{R_0 - 1}{R_0 + 1} (E_1^{n+1} - E_0^n), \quad (\text{B.14})$$

$$E_{N_x}^{n+1} = E_{N_x-1}^n + \frac{R_{N_x} - 1}{R_{N_x} + 1} (E_{N_x-1}^{n+1} - E_{N_x}^n). \quad (\text{B.15})$$

Without these boundary conditions, the numerical solution would feature unphysical reflections from the system boundaries. In order to calculate only the incoming field for a scattering problem, equivalent boundary conditions can be implemented at the edges of the scattering region to suppress the backscattering.

## B.2 Helmholtz equation

In many cases, we are not interested in a full time-dependent simulation but only in a stationary solution for a given system. For that purpose, we assume that the steady-state solution  $\mathbf{E}(\mathbf{r}, t)$  from eq. (B.7) can be separated in a spatially dependent function  $\mathbf{E}(\mathbf{r})$  and a harmonic time-dependence  $\phi(t) = \exp(-i\omega t)$  with frequency  $\omega$ , i.e.,

$$\mathbf{E}(\mathbf{r}, t) = \mathbf{E}(\mathbf{r}) \cdot \phi(t) = \mathbf{E}(\mathbf{r}) \cdot e^{-i\omega t}. \quad (\text{B.16})$$

Equivalently, we require that also the current density has a harmonic time-dependence,

$$\mathbf{j}_i(\mathbf{r}, t) = \mathbf{j}_i(\mathbf{r}) \cdot \phi(t) = \mathbf{j}_i(\mathbf{r}) \cdot e^{-i\omega t}. \quad (\text{B.17})$$

Inserting eqs. (B.16) and (B.17) into eq. (B.7) and canceling out the time-dependence yields the vector Helmholtz equation

$$\nabla \times \nabla \times \mathbf{E}(\mathbf{r}) - n^2(\mathbf{r})k^2\mathbf{E}(\mathbf{r}) = -\mathbf{f}(\mathbf{r}), \quad (\text{B.18})$$

with the wave number  $k = \omega/c$  and the source term

$$\mathbf{f}(\mathbf{r}) = -i\omega\mu_0 \frac{\partial}{\partial t} \mathbf{j}_i(\mathbf{r}). \quad (\text{B.19})$$

With the aid of the vector calculus identity

$$\nabla \times (\nabla \times \mathbf{A}) = \nabla (\nabla \cdot \mathbf{A}) - \nabla^2 \mathbf{A}, \quad (\text{B.20})$$

eq. (B.18) can be rewritten as

$$\Delta \mathbf{E}(\mathbf{r}) - \nabla [\nabla \cdot \mathbf{E}(\mathbf{r})] + n^2(\mathbf{r})k^2\mathbf{E}(\mathbf{r}) = \mathbf{f}(\mathbf{r}), \quad (\text{B.21})$$

where  $\Delta \equiv \nabla^2$  represents the vector Laplacian. Since we assume a charge-free medium ( $\rho_f \equiv 0$ ), we can derive the following relation from eqs. (B.1) and (B.5):

$$\begin{aligned} \nabla \cdot \mathbf{E}(\mathbf{r}) &= -\frac{1}{\varepsilon_r(\mathbf{r})} \nabla \varepsilon_r(\mathbf{r}) \cdot \mathbf{E}(\mathbf{r}) \\ &= -\nabla \ln(\varepsilon_r(\mathbf{r})) \cdot \mathbf{E}(\mathbf{r}). \end{aligned} \quad (\text{B.22})$$

Inserting eq. (B.22) into eq. (B.21) then leads to the three-dimensional Helmholtz equation for inhomogeneous media,

$$\Delta \mathbf{E}(\mathbf{r}) + \nabla [\nabla \ln(\varepsilon_r(\mathbf{r})) \cdot \mathbf{E}(\mathbf{r})] + n^2(\mathbf{r})k^2\mathbf{E}(\mathbf{r}) = \mathbf{f}(\mathbf{r}). \quad (\text{B.23})$$

In this thesis, we consider only one-dimensional and effectively two-dimensional media (waveguides with a low height), for which  $\varepsilon_r(\mathbf{r}) = \varepsilon_r(x, y)$ , i.e., the permittivity gradient lies in the  $xy$ -plane. Furthermore, it can be shown [147] that for rectangular waveguides with a very low height the propagating modes are  $z$ -polarized such that

$\mathbf{E}(\mathbf{r}) = (0, 0, \psi(x, y))^T$ . Therefore, we have  $\nabla \ln(\epsilon_r(\mathbf{r})) \cdot \mathbf{E}(\mathbf{r}) = 0$ , which directly leads to the scalar Helmholtz equation

$$\left[ \Delta + n^2(x, y)k^2 \right] \psi(x, y) = f(x, y) \quad (\text{B.24})$$

for the  $z$ -component of the electric field  $\psi(x, y) \equiv E_z(x, y)$  with the source term  $f(x, y) \equiv f_z(x, y)$ . For one-dimensional problems, where we consider a scalar electric field  $E(x)$ , we find an analogous scalar Helmholtz equation of the form

$$\left[ \frac{\partial^2}{\partial x^2} + n^2(x)k^2 \right] E(x) = f(x), \quad (\text{B.25})$$

which can also be derived by inserting the one-dimensional counterparts of eqs. (B.16) and (B.17) into eq. (B.8).

Similarly to the procedure in appendix B.1, we need to discretize the spatial variable (i.e.,  $x \rightarrow x_j$ ) in order to solve eq. (B.25) numerically, which leads to the approximation (cf. eq. (B.9))

$$\left. \frac{\partial^2 E}{\partial x^2} \right|_{(j\Delta x)} = \frac{E_{j+1} - 2E_j + E_{j-1}}{\Delta x^2} + \mathcal{O}(\Delta x^2) \quad (\text{B.26})$$

for the second derivative as well as to the discretized versions of the solution  $E_j \equiv E(x_j)$ , the source  $f_j \equiv f(x_j)$ , and the refractive index  $n_j \equiv n(x_j)$ . If the electric field and the source term for all grid points are encapsulated into the vectors  $\mathbf{E}$  and  $\mathbf{f}$ , eq. (B.25) can be compactly written as a matrix equation,

$$\mathbf{M} \cdot \mathbf{E} = \mathbf{f}, \quad (\text{B.27})$$

with the matrix

$$\mathbf{M} = \mathbf{M}_1 + \mathbf{M}_2 = \frac{1}{\Delta x^2} \begin{pmatrix} -2 & 1 & 0 & \cdots & 0 \\ 1 & -2 & 1 & \cdots & 0 \\ 0 & 1 & -2 & \cdots & 0 \\ \vdots & \vdots & \vdots & \ddots & \vdots \\ 0 & 0 & 0 & \cdots & -2 \end{pmatrix} + k^2 \begin{pmatrix} n_1^2 & 0 & 0 & \cdots & 0 \\ 0 & n_2^2 & 0 & \cdots & 0 \\ 0 & 0 & n_3^2 & \cdots & 0 \\ \vdots & \vdots & \vdots & \ddots & \vdots \\ 0 & 0 & 0 & \cdots & n_{N_x}^2 \end{pmatrix}. \quad (\text{B.28})$$

Transparent boundary conditions—to simulate an infinitely extended system—can be implemented by modifying the coupling for the first and last grid point. For that purpose, the term  $\exp(in(x)k\Delta x)/\Delta x^2$  is added to  $M_{11}$  and  $M_{N_x N_x}$ , i.e., the matrix  $M_1$  in eq. (B.28) is replaced according to

$$\mathbf{M}_1 \rightarrow \mathbf{M}'_1 = \frac{1}{\Delta x^2} \begin{pmatrix} -2 + e^{in_1 k \Delta x} & 1 & 0 & \cdots & 0 \\ 1 & -2 & 1 & \cdots & 0 \\ 0 & 1 & -2 & \cdots & 0 \\ \vdots & \vdots & \vdots & \ddots & \vdots \\ 0 & 0 & 0 & \cdots & -2 + e^{in_{N_x} k \Delta x} \end{pmatrix}. \quad (\text{B.29})$$



As already explained in [appendix B.1](#), the incoming field can be calculated by implementing equivalent boundary conditions at the edges of the scattering region.

Finally, a point source at position  $x_j = x_s$  that emits a plane wave with amplitude  $A$  can be realized by setting the corresponding component of the source vector equal to  $f_s = 2iAn_s k/\Delta x$ . The solution of the one-dimensional Helmholtz equation is then given by

$$\mathbf{E} = M^{-1} \cdot \mathbf{f}. \quad (\text{B.30})$$

Higher dimensional problems which are described by [eq. \(B.23\)](#) or [eq. \(B.24\)](#) can be solved with the finite element method. The two-dimensional simulations presented in this thesis were performed with a *Python* code developed by Matthias Kühmayer. This code is based on the open-source finite element software package *Netgen/NGSolve*<sup>18</sup> [164,165] and its functionality is described in detail within his dissertation [149].

### B.3 Time-averaged Poynting vector

The directional energy flux of an electromagnetic field is given by the Poynting vector [147, 166], which is defined as the cross product of the electric and the magnetic field strength vectors,

$$\mathbf{S}(\mathbf{r}, t) = \mathbf{E}(\mathbf{r}, t) \times \mathbf{H}(\mathbf{r}, t). \quad (\text{B.31})$$

For a stationary state, the fields are characterized by a harmonic time-dependence, i.e.,

$$\mathbf{E}(\mathbf{r}, t) = \mathbf{E}(\mathbf{r}) \cdot e^{-i\omega t}, \quad (\text{B.32})$$

$$\mathbf{H}(\mathbf{r}, t) = \mathbf{H}(\mathbf{r}) \cdot e^{-i\omega t}. \quad (\text{B.33})$$

Since the physical fields are described by the real parts of [eqs. \(B.32\)](#) and [\(B.33\)](#), the Poynting vector may be written as

$$\begin{aligned} \mathbf{S}(\mathbf{r}, t) &= \text{Re} [\mathbf{E}(\mathbf{r}) e^{-i\omega t}] \times \text{Re} [\mathbf{H}(\mathbf{r}) e^{-i\omega t}] \\ &= [\mathbf{E}_R(\mathbf{r}) \cos(\omega t) + \mathbf{E}_I(\mathbf{r}) \sin(\omega t)] \times [\mathbf{H}_R(\mathbf{r}) \cos(\omega t) + \mathbf{H}_I(\mathbf{r}) \sin(\omega t)] \\ &= \mathbf{E}_R(\mathbf{r}) \times \mathbf{H}_R(\mathbf{r}) \cos^2(\omega t) + \mathbf{E}_R(\mathbf{r}) \times \mathbf{H}_I(\mathbf{r}) \cos(\omega t) \sin(\omega t) \\ &\quad + \mathbf{E}_I(\mathbf{r}) \times \mathbf{H}_R(\mathbf{r}) \sin(\omega t) \cos(\omega t) + \mathbf{E}_I(\mathbf{r}) \times \mathbf{H}_I(\mathbf{r}) \sin^2(\omega t), \end{aligned} \quad (\text{B.34})$$

where the subscripts R and I denote the real and imaginary parts of the respective fields. Taking the average of [eq. \(B.34\)](#) over one oscillation period  $T = 2\pi/\omega$  yields the time-averaged Poynting vector

$$\begin{aligned} \mathbf{S}(\mathbf{r}) &= \frac{\omega}{2\pi} \int_0^{\frac{2\pi}{\omega}} dt \mathbf{S}(\mathbf{r}, t) \\ &= \frac{1}{2} [\mathbf{E}_R(\mathbf{r}) \times \mathbf{H}_R(\mathbf{r}) + \mathbf{E}_I(\mathbf{r}) \times \mathbf{H}_I(\mathbf{r})], \end{aligned} \quad (\text{B.35})$$

<sup>18</sup> <https://ngsolve.org/>

which can be expressed in terms of the total  $\mathbf{E}$ - and  $\mathbf{H}$ -fields by adding suitably constructed purely imaginary terms and then taking only the real part of the resulting expression:

$$\begin{aligned}
 \mathbf{S} &= \frac{1}{2} \text{Re} (\mathbf{E}_R \times \mathbf{H}_R + \mathbf{E}_I \times \mathbf{H}_I + i \mathbf{E}_I \times \mathbf{H}_R - i \mathbf{E}_R \times \mathbf{H}_I) \\
 &= \frac{1}{2} \text{Re} [(\mathbf{E}_R + i \mathbf{E}_I) \times (\mathbf{H}_R - i \mathbf{H}_I)] \\
 &= \frac{1}{2} \text{Re} (\mathbf{E} \times \mathbf{H}^*) .
 \end{aligned} \tag{B.36}$$

Note that we have dropped the spatial dependence for better readability. While eq. (B.36) could be used to calculate the energy flux in a full three-dimensional simulation, the expression for the time-averaged Poynting vector can be further simplified for the two-dimensional case described by eq. (B.24), which is treated in this thesis. Considering a  $z$ -polarized electric field  $\mathbf{E} = (0, 0, \psi)^\top$  with a harmonic time-dependence and  $\mu_r \equiv 1$ , the corresponding magnetic field follows from eqs. (B.3) and (B.6) and is given by  $\mathbf{H} = \frac{1}{\omega\mu_0} (-i\partial_y\psi, i\partial_x\psi, 0)^\top$ . Inserting everything into eq. (B.36) finally delivers

$$\begin{aligned}
 \mathbf{S} &= \frac{1}{2\omega\mu_0} \text{Re} [\psi(-i\nabla\psi)^*] \\
 &= \frac{1}{2\omega\mu_0} \text{Re} [\psi^*(-i\nabla\psi)] .
 \end{aligned} \tag{B.37}$$

# Acknowledgments

At this point, I would like to take the opportunity to express my special gratitude to all the people who have contributed to the success of my doctoral studies.

First and foremost, I want to thank my supervisor Stefan Rotter for his persistent support from the very first day when I joined his team. I am especially grateful for his valuable input in countless discussions, for his ongoing encouragement, and for enabling me to broaden my horizon in multiple foreign research stays and conferences. Besides that, I appreciate his considerate and polite personality, as well as the pleasant working environment in his group.

Furthermore, sincere thanks are due to the colleagues from our group for many stimulating discussions and very helpful support. In particular, I am indebted to Matthias Kühmayer, who kept providing me with numerous simulation results and numerical codes during all the years.

Moreover, I want to thank my Master student Helmut Hörner, as well as my Bachelor students Katharina Hauer, Felix Russo, Andrea Pupić, and Thomas Ranner, for the great job they did in their projects, which parts of this thesis are built on.

Special thanks are extended to Ulrich Kuhl, Şahin Özdemir, and Mikael Rechtsman for hosting me so nicely during my research stays in their labs and for the fruitful collaboration. In addition, I want to thank Franco Nori and A. Douglas Stone for inviting and hosting me to visit their groups.

Further, I would like to thank our collaborators from the Laboratory of Micro/Nano Photonics in the McKelvey School of Engineering at Washington University in Saint Louis, who have performed the phonon laser experiments presented in this thesis, as well as Ori Katz, Yevgeny Slobodkin, and Gil Weinberg for conducting the experiments related to the degenerate cavity anti-laser project. Additionally, I thank Joachim Krenn and Martin Belitsch for the experimental collaboration.

Warm thanks go to Heike Höller, Sylvia Riedler, and Ingrid Unger for their helpfulness and administrative assistance.

Finally, my sincere gratefulness is offered to my family for their continuous support throughout my entire life.



# List of Figures and Tables

Fig. 2.1	Fundamental light-matter interactions . . . . .	6
Fig. 2.2	Typical laser pumping schemes . . . . .	7
Fig. 2.3	Different types of optical feedback in lasers . . . . .	8
Fig. 2.4	Experimental setup of a phonon laser . . . . .	11
Fig. 3.1	Eigenvalues of a non-Hermitian matrix . . . . .	18
Fig. 3.2	Bifurcation of the optical supermodes in a phonon laser . . . . .	19
Tab. 3.1	Phonon laser system parameters . . . . .	20
Fig. 3.3	Measured phonon laser threshold behavior . . . . .	21
Fig. 3.4	Analytical approximation for the phonon laser threshold behavior . . . . .	22
Fig. 3.5	Simulated phonon laser threshold behavior . . . . .	23
Fig. 3.6	Intra-cavity field intensity in a phonon laser . . . . .	24
Fig. 3.7	Measured phonon laser linewidth behavior . . . . .	25
Fig. 3.8	Simplified linewidth model for two coupled optical modes . . . . .	27
Fig. 4.1	Basic realization of coherent perfect absorption . . . . .	30
Fig. 4.2	Poles and zeros of the scattering matrix . . . . .	31
Fig. 4.3	Simple coherent perfect absorber . . . . .	33
Fig. 4.4	Experimental setup of a random anti-laser . . . . .	35
Fig. 4.5	Injection accuracy analysis of specific states in a random anti-laser . . . . .	37
Fig. 4.6	Absorption analysis of a CPA state . . . . .	39
Fig. 4.7	Typical scattering matrices of a random anti-laser . . . . .	40
Fig. 4.8	Simulated field intensity and energy flux of a random anti-laser . . . . .	41
Fig. 4.9	Transmission of CPA states into an absorbing antenna . . . . .	42
Fig. 4.10	Field of CPA states with and without absorbing antenna . . . . .	43
Fig. 4.11	Simulated and measured field of a random anti-laser . . . . .	44
Fig. 4.12	Antenna coupling analysis in a random anti-laser . . . . .	45
Fig. 4.13	Time-reversal symmetry analysis of a CPA state . . . . .	46
Fig. 4.14	Comparison of localized and global absorption . . . . .	47
Fig. 4.15	CPA induced by global absorption . . . . .	48
Fig. 4.16	Sub-wavelength focusing of a CPA state . . . . .	50
Fig. 4.17	Evanescence modes at an antenna . . . . .	51
Fig. 4.18	Reflectionless scattering in a random anti-laser . . . . .	52
Fig. 5.1	Simple coherent virtual absorber . . . . .	55
Fig. 5.2	Temporal dependence of the field and stored energy in a CVA . . . . .	56
Fig. 5.3	Coherent virtual absorption in one-dimensional disordered media . . . . .	57
Fig. 5.4	Poles and zeros of the scattering matrix . . . . .	58
Fig. 5.5	One-dimensional reflectionless scattering modes . . . . .	59
Fig. 5.6	Coherent virtual absorption in two-dimensional disordered media . . . . .	60

Fig. 6.1	Customized one-dimensional coherent perfect absorber . . . . .	62
Fig. 6.2	Customized two-dimensional coherent perfect absorber for predefined frequency . . . . .	63
Fig. 6.3	Customized two-dimensional coherent perfect absorber for predefined frequency and wavefront . . . . .	64
Fig. 6.4	Degenerate cavity anti-laser . . . . .	65
Fig. 6.5	Experimental setup and results for a degenerate cavity CPA . . . . .	66
Fig. 6.6	Sensitivity of a degenerate cavity CPA to maladjustment . . . . .	67
Fig. 6.7	Scattering suppression from a detuned CPA . . . . .	69
Tab. 6.1	Scattering suppression from a detuned CPA . . . . .	70
Fig. 6.8	Absorption of an electromagnetic pulse . . . . .	71

# Bibliography

- [1] A. L. Schawlow and C. H. Townes. *Infrared and Optical Masers*. Physical Review **112**, 1940 (1958).
- [2] R. G. Gould. *The LASER, Light Amplification by Stimulated Emission of Radiation*. In P. A. Franken and R. H. Sands (editors), *The Ann Arbor Conference on Optical Pumping, the University of Michigan, June 15 through June 18, 1959*, p. 128 (1959).
- [3] A. Einstein. *Strahlungs-Emission und -Absorption nach der Quantentheorie*. Verhandlungen der Deutschen Physikalischen Gesellschaft **18**, 318 (1916).
- [4] A. Einstein. *Zur Quantentheorie der Strahlung*. Physikalische Zeitschrift **18**, 121 (1917).
- [5] J. P. Gordon, H. J. Zeiger, and C. H. Townes. *Molecular Microwave Oscillator and New Hyperfine Structure in the Microwave Spectrum of NH<sub>3</sub>*. Physical Review **95**, 282 (1954).
- [6] J. P. Gordon, H. J. Zeiger, and C. H. Townes. *The Maser—New Type of Microwave Amplifier, Frequency Standard, and Spectrometer*. Physical Review **99**, 1264 (1955).
- [7] H. J. Eichler, J. Eichler, and O. Lux. *Lasers: Basics, Advances and Applications*, vol. 220 of *Springer Series in Optical Sciences*. Springer, Cham (2018).
- [8] H. Haken. *Laser Theory*. Springer, Berlin (1984).
- [9] H. Haken. *Light: Volume II: Laser Light Dynamics*. North-Holland, Amsterdam (1985).
- [10] A. E. Siegman. *Lasers*. University Science Books, Mill Valley, CA (1986).
- [11] K. Thyagarajan and A. Ghatak. *Lasers: fundamentals and applications*. Springer Science & Business Media (2010).
- [12] C. E. Webb and J. D. C. Jones (editors). *Handbook of Laser Technology and Applications: Volume 3: Applications*. CRC Press (2020).
- [13] W. E. Bron and W. Grill. *Stimulated Phonon Emission*. Physical Review Letters **40**, 1459 (1978).

- [14] P. A. Fokker, J. I. Dijkhuis, and H. W. de Wijn. *Stimulated emission of phonons in an acoustical cavity*. *Physical Review B* **55**, 2925 (1997).
- [15] S. T. Zavtrak and I. V. Volkov. *Sound amplification by stimulated emission of radiation (Saser) with cylindrical resonator*. *Ultrasonics* **34**, 691 (1996).
- [16] I. V. Volkov, S. T. Zavtrak, and I. S. Kuten. *Theory of sound amplification by stimulated emission of radiation with consideration for coagulation*. *Physical Review E* **56**, 1097 (1997).
- [17] A. J. Kent, R. N. Kini, N. M. Stanton, M. Henini, B. A. Glavin, V. A. Kochelap, and T. L. Linnik. *Acoustic Phonon Emission from a Weakly Coupled Superlattice under Vertical Electron Transport: Observation of Phonon Resonance*. *Physical Review Letters* **96**, 215504 (2006).
- [18] K. Vahala, M. Herrmann, S. Knünz, V. Batteiger, G. Saathoff, T. W. Hänsch, and T. Udem. *A phonon laser*. *Nature Physics* **5**, 682 (2009).
- [19] I. S. Grudinin, H. Lee, O. Painter, and K. J. Vahala. *Phonon Laser Action in a Tunable Two-Level System*. *Physical Review Letters* **104**, 083901 (2010).
- [20] R. P. Beardsley, A. V. Akimov, M. Henini, and A. J. Kent. *Coherent Terahertz Sound Amplification and Spectral Line Narrowing in a Stark Ladder Superlattice*. *Physical Review Letters* **104**, 085501 (2010).
- [21] J. Kabuss, A. Carmele, T. Brandes, and A. Knorr. *Optically Driven Quantum Dots as Source of Coherent Cavity Phonons: A Proposal for a Phonon Laser Scheme*. *Physical Review Letters* **109**, 054301 (2012).
- [22] J. Kabuss, A. Carmele, and A. Knorr. *Threshold behavior and operating regimes of an optically driven phonon laser: Semiclassical theory*. *Physical Review B* **88**, 064305 (2013).
- [23] I. Mahboob, K. Nishiguchi, A. Fujiwara, and H. Yamaguchi. *Phonon Lasing in an Electromechanical Resonator*. *Physical Review Letters* **110**, 127202 (2013).
- [24] J. Zhang, B. Peng, Ş. K. Özdemir, K. Pichler, D. O. Krimer, G. Zhao, F. Nori, Y.-x. Liu, S. Rotter, and L. Yang. *A phonon laser operating at an exceptional point*. *Nature Photonics* **12**, 479 (2018).
- [25] Y. Jiang, S. Maayani, T. Carmon, F. Nori, and H. Jing. *Nonreciprocal Phonon Laser*. *Physical Review Applied* **10**, 064037 (2018).
- [26] R. M. Pettit, W. Ge, P. Kumar, D. R. Luntz-Martin, J. T. Schultz, L. P. Neukirch, M. Bhattacharya, and A. N. Vamivakas. *An optical tweezer phonon laser*. *Nature Photonics* **13**, 402 (2019).



- [27] R. Huang and H. Jing. *The nanosphere phonon laser*. Nature Photonics **13**, 372 (2019).
- [28] D. L. Chafatinos, A. S. Kuznetsov, S. Anguiano, A. E. Bruchhausen, A. A. Reynoso, K. Biermann, P. V. Santos, and A. Fainstein. *Polariton-driven phonon laser*. Nature Communications **11**, 4552 (2020).
- [29] D. J. Bergman and M. I. Stockman. *Surface Plasmon Amplification by Stimulated Emission of Radiation: Quantum Generation of Coherent Surface Plasmons in Nanosystems*. Physical Review Letters **90**, 027402 (2003).
- [30] M. A. Noginov, G. Zhu, A. M. Belgrave, R. Bakker, V. M. Shalaev, E. E. Narimanov, S. Stout, E. Herz, T. Suteewong, and U. Wiesner. *Demonstration of a spaser-based nanolaser*. Nature **460**, 1110 (2009).
- [31] R. F. Oulton, V. J. Sorger, T. Zentgraf, R.-M. Ma, C. Gladden, L. Dai, G. Bartal, and X. Zhang. *Plasmon lasers at deep subwavelength scale*. Nature **461**, 629 (2009).
- [32] R.-M. Ma, R. F. Oulton, V. J. Sorger, G. Bartal, and X. Zhang. *Room-temperature sub-diffraction-limited plasmon laser by total internal reflection*. Nature Materials **10**, 110 (2011).
- [33] R. F. Oulton. *Surface plasmon lasers: sources of nanoscopic light*. Materials Today **15**, 26 (2012).
- [34] A. İmamoğlu, R. J. Ram, S. Pau, and Y. Yamamoto. *Nonequilibrium condensates and lasers without inversion: Exciton-polariton lasers*. Phys. Rev. A **53**, 4250 (1996).
- [35] H. Deng, G. Weihs, D. Snoke, J. Bloch, and Y. Yamamoto. *Polariton lasing vs. photon lasing in a semiconductor microcavity*. Proceedings of the National Academy of Sciences **100**, 15318 (2003).
- [36] S. Christopoulos, G. B. H. von Högersthal, A. J. D. Grundy, P. G. Lagoudakis, A. V. Kavokin, J. J. Baumberg, G. Christmann, R. Butté, E. Feltin, J.-F. Carlin, and N. Grandjean. *Room-Temperature Polariton Lasing in Semiconductor Microcavities*. Physical Review Letters **98**, 126405 (2007).
- [37] L. V. Butov. *A polariton laser*. Nature **447**, 540 (2007).
- [38] P. Bhattacharya, B. Xiao, A. Das, S. Bhowmick, and J. Heo. *Solid State Electrically Injected Exciton-Polariton Laser*. Physical Review Letters **110**, 206403 (2013).
- [39] C. Schneider, A. Rahimi-Iman, N. Y. Kim, J. Fischer, I. G. Savenko, M. Amthor, M. Lermer, A. Wolf, L. Worschech, V. D. Kulakovskii *et al.* *An electrically pumped polariton laser*. Nature **497**, 348 (2013).

- [40] S. Kim, B. Zhang, Z. Wang, J. Fischer, S. Brodbeck, M. Kamp, C. Schneider, S. Höfling, and H. Deng. *Coherent Polariton Laser*. *Physical Review X* **6**, 011026 (2016).
- [41] M. Holland, K. Burnett, C. Gardiner, J. I. Cirac, and P. Zoller. *Theory of an atom laser*. *Physical Review A* **54**, R1757 (1996).
- [42] M.-O. Mewes, M. R. Andrews, D. M. Kurn, D. S. Durfee, C. G. Townsend, and W. Ketterle. *Output Coupler for Bose-Einstein Condensed Atoms*. *Physical Review Letters* **78**, 582 (1997).
- [43] I. Bloch, T. W. Hänsch, and T. Esslinger. *Atom Laser with a cw Output Coupler*. *Physical Review Letters* **82**, 3008 (1999).
- [44] S. Inouye, T. Pfau, S. Gupta, A. P. Chikkatur, A. Görlitz, D. E. Pritchard, and W. Ketterle. *Phase-coherent amplification of atomic matter waves*. *Nature* **402**, 641 (1999).
- [45] G. Cennini, G. Ritt, C. Geckeler, and M. Weitz. *All-Optical Realization of an Atom Laser*. *Physical Review Letters* **91**, 240408 (2003).
- [46] N. P. Robins, C. Figl, M. Jeppesen, G. R. Dennis, and J. D. Close. *A pumped atom laser*. *Nature Physics* **4**, 731 (2008).
- [47] V. Bolpasi, N. K. Efremidis, M. J. Morrissey, P. C. Condylis, D. Sahagun, M. Baker, and W. von Klitzing. *An ultra-bright atom laser*. *New Journal of Physics* **16**, 033036 (2014).
- [48] J. B. Khurgin. *Phonon lasers gain a sound foundation*. *Physics* **3**, 16 (2010).
- [49] S. I. Azzam, A. V. Kildishev, R.-M. Ma, C.-Z. Ning, R. Oulton, V. M. Shalaev, M. I. Stockman, J.-L. Xu, and X. Zhang. *Ten years of spasers and plasmonic nanolasers*. *Light: Science & Applications* **9**, 90 (2020).
- [50] M. D. Fraser, S. Höfling, and Y. Yamamoto. *Physics and applications of exciton-polariton lasers*. *Nature Materials* **15**, 1049 (2016).
- [51] T. Kato. *Perturbation Theory for Linear Operators*. Springer, Berlin (1966).
- [52] M. V. Berry. *Physics of nonhermitian degeneracies*. *Czechoslovak Journal of Physics* **54**, 1039 (2004).
- [53] W. D. Heiss. *Exceptional points of non-Hermitian operators*. *Journal of Physics A: Mathematical and General* **37**, 2455 (2004).
- [54] W. D. Heiss. *The physics of exceptional points*. *Journal of Physics A: Mathematical and Theoretical* **45**, 444016 (2012).

- [55] M.-A. Miri and A. Alù. *Exceptional points in optics and photonics*. Science **363**, eaar7709 (2019).
- [56] M. Liertzer, L. Ge, A. Cerjan, A. D. Stone, H. E. Türeci, and S. Rotter. *Pump-Induced Exceptional Points in Lasers*. Physical Review Letters **108**, 173901 (2012).
- [57] M. Brandstetter, M. Liertzer, C. Deutsch, P. Klang, J. Schöberl, H. E. Türeci, G. Strasser, K. Unterrainer, and S. Rotter. *Reversing the pump dependence of a laser at an exceptional point*. Nature Communications **5**, 4034 (2014).
- [58] B. Peng, Ş. K. Özdemir, S. Rotter, H. Yilmaz, M. Liertzer, F. Monifi, C. M. Bender, F. Nori, and L. Yang. *Loss-induced suppression and revival of lasing*. Science **346**, 328 (2014).
- [59] B. Peng, Ş. K. Özdemir, M. Liertzer, W. Chen, J. Kramer, H. Yilmaz, J. Wiersig, S. Rotter, and L. Yang. *Chiral modes and directional lasing at exceptional points*. Proceedings of the National Academy of Sciences **113**, 6845 (2016).
- [60] J. Doppler, A. A. Mailybaev, J. Böhm, U. Kuhl, A. Girschik, F. Libisch, T. J. Milburn, P. Rabl, N. Moiseyev, and S. Rotter. *Dynamically encircling an exceptional point for asymmetric mode switching*. Nature **537**, 76 (2016).
- [61] H. Wenzel, U. Bandelow, H.-J. Wunsche, and J. Rehberg. *Mechanisms of Fast Self Pulsations in Two-Section DFB Lasers*. IEEE Journal of Quantum Electronics **32**, 69 (1996).
- [62] M. V. Berry. *Mode degeneracies and the Petermann excess-noise factor for unstable lasers*. Journal of Modern Optics **50**, 63 (2003).
- [63] K. Petermann. *Calculated spontaneous emission factor for double-heterostructure injection lasers with gain-induced waveguiding*. IEEE Journal of Quantum Electronics **15**, 566 (1979).
- [64] A. E. Siegman. *Excess spontaneous emission in non-Hermitian optical systems. I. Laser amplifiers*. Physical Review A **39**, 1253 (1989).
- [65] A. E. Siegman. *Excess spontaneous emission in non-Hermitian optical systems. II. Laser oscillators*. Physical Review A **39**, 1264 (1989).
- [66] W. A. Hamel and J. P. Woerdman. *Observation of enhanced fundamental linewidth of a laser due to nonorthogonality of its longitudinal eigenmodes*. Physical Review Letters **64**, 1506 (1990).
- [67] Y.-J. Cheng, C. G. Fanning, and A. E. Siegman. *Experimental Observation of a Large Excess Quantum Noise Factor in the Linewidth of a Laser Oscillator Having Nonorthogonal Modes*. Physical Review Letters **77**, 627 (1996).

- [68] M. A. Van Eijkelenborg, Å. M. Lindberg, M. S. Thijssen, and J. P. Woerdman. *Resonance of quantum noise in an unstable cavity laser*. Physical Review Letters **77**, 4314 (1996).
- [69] S. Rotter and S. Gigan. *Light fields in complex media: Mesoscopic scattering meets wave control*. Reviews of Modern Physics **89**, 015005 (2017).
- [70] Y. D. Chong, L. Ge, H. Cao, and A. D. Stone. *Coherent Perfect Absorbers: Time-Reversed Lasers*. Physical Review Letters **105**, 053901 (2010).
- [71] W. Wan, Y. Chong, L. Ge, H. Noh, A. D. Stone, and H. Cao. *Time-Reversed Lasing and Interferometric Control of Absorption*. Science **331**, 889 (2011).
- [72] S. Longhi. *Backward lasing yields a perfect absorber*. Physics **3**, 61 (2010).
- [73] C. F. Gmachl. *Suckers for light*. Nature **467**, 37 (2010).
- [74] D. G. Baranov, A. Krasnok, T. Shegai, A. Alù, and Y. Chong. *Coherent perfect absorbers: linear control of light with light*. Nature Reviews Materials **2**, 17064 (2017).
- [75] S. Longhi. *Coherent perfect absorption in a homogeneously broadened two-level medium*. Physical Review A **83**, 055804 (2011).
- [76] H. Noh, Y. Chong, A. D. Stone, and H. Cao. *Perfect coupling of light to surface plasmons by coherent absorption*. Physical Review Letters **108**, 186805 (2012).
- [77] J. W. Yoon, G. M. Koh, S. H. Song, and R. Magnusson. *Measurement and Modeling of a Complete Optical Absorption and Scattering by Coherent Surface Plasmon-Polariton Excitation Using a Silver Thin-Film Grating*. Physical Review Letters **109**, 257402 (2012).
- [78] M. Kang, F. Liu, T.-F. Li, Q.-H. Guo, J. Li, and J. Chen. *Polarization-independent coherent perfect absorption by a dipole-like metasurface*. Optics Letters **38**, 3086 (2013).
- [79] J. Z. Song, P. Bai, Z. H. Hang, and Y. Lai. *Acoustic coherent perfect absorbers*. New Journal of Physics **16**, 033026 (2014).
- [80] P. Wei, C. Croënne, S. T. Chu, and J. Li. *Symmetrical and anti-symmetrical coherent perfect absorption for acoustic waves*. Applied Physics Letters **104**, 121902 (2014).
- [81] Y. Sun, W. Tan, H.-q. Li, J. Li, and H. Chen. *Experimental Demonstration of a Coherent Perfect Absorber with PT Phase Transition*. Physical Review Letters **112**, 143903 (2014).

- [82] J. Zhang, C. Guo, K. Liu, Z. Zhu, W. Ye, X. Yuan, and S. Qin. *Coherent perfect absorption and transparency in a nanostructured graphene film*. Optics Express **22**, 12524 (2014).
- [83] S. Li, J. Luo, S. Anwar, S. Li, W. Lu, Z. H. Hang, Y. Lai, B. Hou, M. Shen, and C. Wang. *An equivalent realization of coherent perfect absorption under single beam illumination*. Scientific Reports **4**, 7369 (2014).
- [84] Y. Ra'di, C. R. Simovski, and S. A. Tretyakov. *Thin Perfect Absorbers for Electromagnetic Waves: Theory, Design, and Realizations*. Physical Review Applied **3**, 037001 (2015).
- [85] T. Roger, S. Vezzoli, E. Bolduc, J. Valente, J. J. F. Heitz, J. Jeffers, C. Soci, J. Leach, C. Couteau, N. I. Zheludev, and D. Faccio. *Coherent perfect absorption in deeply subwavelength films in the single-photon regime*. Nature Communications **6**, 7031 (2015).
- [86] J.-H. Wu, M. Artoni, and G. C. La Rocca. *Coherent perfect absorption in one-sided reflectionless media*. Scientific Reports **6**, 35356 (2016).
- [87] C. Meng, X. Zhang, S. T. Tang, M. Yang, and Z. Yang. *Acoustic Coherent Perfect Absorbers as Sensitive Null Detectors*. Scientific Reports **7**, 43574 (2017).
- [88] Y.-h. Wei, W.-j. Gu, G. Yang, Y. Zhu, and G.-x. Li. *Coherent perfect absorption in a quantum nonlinear regime of cavity quantum electrodynamics*. Physical Review A **97**, 053825 (2018).
- [89] A. Müllers, B. Santra, C. Baals, J. Jiang, J. Benary, R. Labouvie, D. A. Zezyulin, V. V. Konotop, and H. Ott. *Coherent perfect absorption of nonlinear matter waves*. Science Advances **4**, eaat6539 (2018).
- [90] X. Feng, J. Zou, W. Xu, Z. Zhu, X. Yuan, J. Zhang, and S. Qin. *Coherent perfect absorption and asymmetric interferometric light-light control in graphene with resonant dielectric nanostructures*. Optics express **26**, 29183 (2018).
- [91] K. Pichler, M. Kühmayer, J. Böhm, A. Brandstötter, P. Ambichl, U. Kuhl, and S. Rotter. *Random anti-lasing through coherent perfect absorption in a disordered medium*. Nature **567**, 351 (2019).
- [92] L. Chen, T. Kottos, and S. M. Anlage. *Perfect absorption in complex scattering systems with or without hidden symmetries*. Nature Communications **11**, 5826 (2020).
- [93] S. Longhi.  *$\mathcal{PT}$ -symmetric laser absorber*. Physical Review A **82**, 031801 (2010).
- [94] Y. D. Chong, L. Ge, and A. D. Stone.  *$\mathcal{PT}$ -Symmetry Breaking and Laser-Absorber Modes in Optical Scattering Systems*. Physical Review Letters **106**, 093902 (2011).

- [95] Z. J. Wong, Y.-L. Xu, J. Kim, K. O'Brien, Y. Wang, L. Feng, and X. Zhang. *Lasing and anti-lasing in a single cavity*. Nature Photonics **10**, 796 (2016).
- [96] C. M. Bender and S. Boettcher. *Real Spectra in Non-Hermitian Hamiltonians Having  $\mathcal{PT}$  Symmetry*. Physical Review Letters **80**, 5243 (1998).
- [97] R. El-Ganainy, K. G. Makris, D. N. Christodoulides, and Z. H. Musslimani. *Theory of coupled optical  $\mathcal{PT}$ -symmetric structures*. Optics Letters **32**, 2632 (2007).
- [98] K. G. Makris, R. El-Ganainy, D. N. Christodoulides, and Z. H. Musslimani. *Beam Dynamics in  $\mathcal{PT}$  Symmetric Optical Lattices*. Physical Review Letters **100**, 103904 (2008).
- [99] C. E. Rüter, K. G. Makris, R. El-Ganainy, D. N. Christodoulides, M. Segev, and D. Kip. *Observation of parity–time symmetry in optics*. Nature Physics **6**, 192 (2010).
- [100] W. R. Sweeney, C. W. Hsu, S. Rotter, and A. D. Stone. *Perfectly Absorbing Exceptional Points and Chiral Absorbers*. Physical Review Letters **122**, 093901 (2019).
- [101] C. Wang, W. R. Sweeney, A. D. Stone, and L. Yang. *Coherent perfect absorption at an exceptional point*. Science **373**, 1261 (2021).
- [102] S. Soleymani, Q. Zhong, M. Mokim, S. Rotter, R. El-Ganainy, and Ş. K. Özdemir. *Chiral and degenerate perfect absorption on exceptional surfaces*. Nature Communications **13**, 599 (2022).
- [103] J. de Rosny and M. Fink. *Overcoming the Diffraction Limit in Wave Physics Using a Time-Reversal Mirror and a Novel Acoustic Sink*. Physical Review Letters **89**, 124301 (2002).
- [104] G. Lerosey, J. de Rosny, A. Tourin, and M. Fink. *Focusing Beyond the Diffraction Limit with Far-Field Time Reversal*. Science **315**, 1120 (2007).
- [105] G. Ma, X. Fan, F. Ma, J. de Rosny, P. Sheng, and M. Fink. *Towards anti-causal Green's function for three-dimensional sub-diffraction focusing*. Nature Physics **14**, 608 (2018).
- [106] D. G. Baranov, A. Krasnok, and A. Alù. *Coherent virtual absorption based on complex zero excitation for ideal light capturing*. Optica **4**, 1457 (2017).
- [107] S. Longhi. *Coherent virtual absorption for discretized light*. Optics Letters **43**, 2122 (2018).
- [108] G. Trainiti, Y. Ra'di, M. Ruzzene, and A. Alù. *Coherent virtual absorption of elastodynamic waves*. Science Advances **5**, eaaw3255 (2019).

- [109] Q. Zhong, L. Simonson, T. Kottos, and R. El-Ganainy. *Coherent virtual absorption of light in microring resonators*. *Physical Review Research* **2**, 013362 (2020).
- [110] H. Cao. *Lasing in random media*. *Waves in Random Media* **13**, R1 (2003).
- [111] D. S. Wiersma. *The physics and applications of random lasers*. *Nature Physics* **4**, 359 (2008).
- [112] M. Pu, Q. Feng, M. Wang, C. Hu, C. Huang, X. Ma, Z. Zhao, C. Wang, and X. Luo. *Ultrathin broadband nearly perfect absorber with symmetrical coherent illumination*. *Optics Express* **20**, 2246 (2012).
- [113] V. Romero-García, G. Theocharis, O. Richoux, A. Merkel, V. Tournat, and V. Pagneux. *Perfect and broadband acoustic absorption by critically coupled sub-wavelength resonators*. *Scientific Reports* **6**, 19519 (2016).
- [114] Y. Jin and K. Yu. *Broadband single-channel coherent perfect absorption with a perfect magnetic mirror*. *Optics Express* **28**, 35108 (2020).
- [115] P. del Hougne, K. B. Yeo, P. Besnier, and M. Davy. *On-Demand Coherent Perfect Absorption in Complex Scattering Systems: Time Delay Divergence and Enhanced Sensitivity to Perturbations*. *Laser & Photonics Reviews* **15**, 2000471 (2021).
- [116] H. Haken. *Light: Volume I: Waves, Photons, Atoms*. North-Holland, Amsterdam (1981).
- [117] K. Pichler. *Phonon laser linewidth near an exceptional point*. Diploma thesis, TU Wien, Vienna (2016).
- [118] M.-S. Ding, L. Zheng, and C. Li. *Phonon laser in a cavity magnomechanical system*. *Scientific Reports* **9**, 15723 (2019).
- [119] V. B. Braginsky, M. L. Gorodetsky, and V. S. Ilchenko. *Quality-factor and nonlinear properties of optical whispering-gallery modes*. *Physics Letters A* **137**, 393 (1989).
- [120] A. Schliesser and T. J. Kippenberg. *Cavity Optomechanics with Whispering-Gallery Mode Optical Micro-Resonators*. In P. Berman, E. Arimondo, and C. Lin (editors), *Advances in Atomic, Molecular, and Optical Physics*, vol. 58, pp. 207–323. Academic Press (2010).
- [121] M. Aspelmeyer, T. J. Kippenberg, and F. Marquardt. *Cavity optomechanics*. *Reviews of Modern Physics* **86**, 1391 (2014).
- [122] C. V. Raman and K. S. Krishnan. *A New Type of Secondary Radiation*. *Nature* **121**, 501 (1928).
- [123] G. Landsberg. *Eine neue Erscheinung bei der Lichtzerstreuung in Krystallen*. *Naturwissenschaften* **16**, 557 (1928).

- [124] Y.-C. Liu, Y.-W. Hu, C. W. Wong, and Y.-F. Xiao. *Review of cavity optomechanical cooling*. Chinese Physics B **22**, 114213 (2013).
- [125] G. Eckhardt, R. W. Hellwarth, F. J. McClung, S. E. Schwarz, D. Weiner, and E. J. Woodbury. *Stimulated Raman Scattering From Organic Liquids*. Physical Review Letters **9**, 455 (1962).
- [126] K. O. Hill, B. S. Kawasaki, and D. C. Johnson. *Low-threshold cw Raman laser*. Applied Physics Letters **29**, 181 (1976).
- [127] C. K. Law. *Interaction between a moving mirror and radiation pressure: A Hamiltonian formulation*. Physical Review A **51**, 2537 (1995).
- [128] C. W. Gardiner and M. J. Collett. *Input and output in damped quantum systems: Quantum stochastic differential equations and the master equation*. Physical Review A **31**, 3761 (1985).
- [129] C. W. Gardiner and P. Zoller. *Quantum Noise: A Handbook of Markovian and Non-Markovian Quantum Stochastic Methods with Applications to Quantum Optics*. Springer, Berlin (2004).
- [130] T. J. Milburn, J. Doppler, C. A. Holmes, S. Portolan, S. Rotter, and P. Rabl. *General description of quasiadiabatic dynamical phenomena near exceptional points*. Physical Review A **92**, 052124 (2015).
- [131] B. Peng, Ş. K. Özdemir, F. Lei, F. Monifi, M. Gianfreda, G. L. Long, S. Fan, F. Nori, C. M. Bender, and L. Yang. *Parity-time-symmetric whispering-gallery microcavities*. Nature Physics **10**, 394 (2014).
- [132] H. Jing, S. K. Özdemir, X.-Y. Lü, J. Zhang, L. Yang, and F. Nori.  *$\mathcal{PT}$ -Symmetric Phonon Laser*. Physical Review Letters **113**, 053604 (2014).
- [133] S. J. M. Kuppens, M. P. Van Exter, and J. P. Woerdman. *Quantum-Limited Linewidth of a Bad-Cavity Laser*. Physical Review Letters **72**, 3815 (1994).
- [134] S. J. M. Kuppens, M. A. Van Eijkelenborg, C. A. Schrama, M. P. Van Exter, and J. P. Woerdman. *Incomplete Inversion and Double-Valued Fundamental Linewidth of Infrared HeNe and HeXe Lasers*. IEEE Journal of Quantum Electronics **32**, 383 (1996).
- [135] C. Henry. *Theory of the Linewidth of Semiconductor Lasers*. IEEE Journal of Quantum Electronics **18**, 259 (1982).
- [136] G. H. C. New. *The origin of excess noise*. Journal of Modern Optics **42**, 799 (1995).
- [137] M. A. van Eijkelenborg, A. M. Lindberg, M. S. Thijssen, and J. P. Woerdman. *Resonance of Quantum Noise in an Unstable Cavity Laser*. Physical Review Letters **77**, 4314 (1996).



- [138] Y. D. Chong and A. D. Stone. *General linewidth formula for steady-state multimode lasing in arbitrary cavities*. Physical Review Letters **109**, 063902 (2012).
- [139] A. Pick, A. Cerjan, D. Liu, A. W. Rodriguez, A. D. Stone, Y. D. Chong, and S. G. Johnson. *Ab initio multimode linewidth theory for arbitrary inhomogeneous laser cavities*. Physical Review A **91**, 063806 (2015).
- [140] A. Cerjan, A. Pick, Y. D. Chong, S. G. Johnson, and A. D. Stone. *Quantitative test of general theories of the intrinsic laser linewidth*. Optics Express **23**, 28316 (2015).
- [141] H. E. Türeci, A. D. Stone, and B. Collier. *Self-consistent multimode lasing theory for complex or random lasing media*. Physical Review A **74**, 043822 (2006).
- [142] L. Ge, Y. D. Chong, and A. D. Stone. *Steady-state ab initio laser theory: Generalizations and analytic results*. Physical Review A **82**, 063824 (2010).
- [143] P. Grangier and J.-P. Poizat. *A simple quantum picture for the Petermann excess noise factor*. The European Physical Journal D - Atomic, Molecular, Optical and Plasma Physics **1**, 97 (1998).
- [144] A. P. Mosk, A. Lagendijk, G. Lerosey, and M. Fink. *Controlling waves in space and time for imaging and focusing in complex media*. Nature Photonics **6**, 283 (2012).
- [145] H. Cao, A. P. Mosk, and S. Rotter. *Shaping the propagation of light in complex media*. Nature Physics **18**, 994 (2022).
- [146] J. Böhm. *Microwave experiments on atypical transport phenomena induced by spatial and spectral wave shaping*. Ph.D. thesis, Université Côte d’Azur, Nice (2016).
- [147] J. D. Jackson. *Classical Electrodynamics*. John Wiley & Sons, New York (1999).
- [148] M. Horodyski, M. Kühmayer, A. Brandstötter, K. Pichler, Y. V. Fyodorov, U. Kuhl, and S. Rotter. *Optimal wave fields for micromanipulation in complex scattering environments*. Nature Photonics **14**, 149 (2020).
- [149] M. Kühmayer. *Optimal Wave Fields in Complex Scattering Environments*. Ph.D. thesis, TU Wien, Vienna (2022).
- [150] M. Born and E. Wolf. *Principles of optics: electromagnetic theory of propagation, interference and diffraction of light*. Cambridge University Press, Cambridge (1997).
- [151] W. R. Sweeney, C. W. Hsu, and A. D. Stone. *Theory of reflectionless scattering modes*. Physical Review A **102**, 063511 (2020).

- [152] A. Pupić. *Coherent virtual absorption*. Bachelor thesis, TU Wien, Vienna (2021).
- [153] T. Ranner. *Coherent virtual absorption in two-dimensional disordered media*. Bachelor thesis, TU Wien, Vienna (2021).
- [154] K. Hauer. *Examination of a one-dimensional coherent perfect absorber for predefined input states and frequency*. Bachelor thesis, TU Wien, Vienna (2019).
- [155] F. Russo. *Coherent perfect absorption in a disordered medium on demand*. Bachelor thesis, TU Wien, Vienna (2019).
- [156] H. Hörner. *Theory of a massively parallel coherent perfect absorber in a degenerate 4f-cavity*. Diploma thesis, TU Wien, Vienna (2021).
- [157] Y. Slobodkin, G. Weinberg, H. Hörner, K. Pichler, S. Rotter, and O. Katz. *Massively degenerate coherent perfect absorber for arbitrary wavefronts*. *Science* **377**, 995 (2022).
- [158] J. A. Arnaud. *Degenerate Optical Cavities*. *Applied Optics* **8**, 189 (1969).
- [159] A. Pupić. *Perfect absorption of electromagnetic pulses*. Project work, TU Wien, Vienna (2022).
- [160] P. Glendinning. *Stability, Instability and Chaos: An Introduction to the Theory of Nonlinear Differential Equations*. Cambridge University Press, Cambridge (1994).
- [161] J. C. Maxwell. *A Dynamical Theory of the Electromagnetic Field*. *Philosophical transactions of the Royal Society of London* **155**, 459 (1865).
- [162] S. Širca and M. Horvat. *Computational Methods in Physics*. Springer International Publishing, Cham (2018).
- [163] G. Mur. *Absorbing Boundary Conditions for the Finite-Difference Approximation of the Time-Domain Electromagnetic-Field Equations*. *IEEE Transactions on Electromagnetic Compatibility* **EMC-23**, 377 (1981).
- [164] J. Schöberl. *NETGEN An advancing front 2D/3D-mesh generator based on abstract rules*. *Computing and Visualization in Science* **1**, 41 (1997).
- [165] J. Schöberl. *C++11 Implementation of Finite Elements in NGSolve*. ASC Report, Institute for Analysis and Scientific Computing, TU Wien (2014).
- [166] J. H. Poynting. *On the Transfer of Energy in the Electromagnetic Field*. *Philosophical Transactions of the Royal Society of London* **175**, 343 (1884).

# Curriculum vitae

---

## PERSONAL DATA

Name: Dipl.-Ing. **Kevin Pichler**, BSc  
Address: Hainburger Str. 66/22, 1030 Wien  
Date of birth: 23/11/1990  
Place of birth: Wolfsberg, Austria  
Nationality: Austrian  
Phone: +43 1 58801 13644  
Email: kevin.pichler@tuwien.ac.at  
Internet: <https://rottergroup.itp.tuwien.ac.at>

---

## EDUCATION

- since 11/2016 **Doctoral program in Engineering Sciences: Technical Physics  
Vienna University of Technology (TU Wien), 1040 Wien**  
PhD thesis: *Generalized application and time-reversal of the lasing principle*
- 03/2014 – 10/2016 **Master program Technical Physics  
Vienna University of Technology (TU Wien), 1040 Wien**  
Graduation with distinction, merit scholarship 2014  
Diploma thesis: *Phonon laser linewidth near an exceptional point*
- 10/2010 – 03/2014 **Bachelor program Technical Physics  
Vienna University of Technology (TU Wien), 1040 Wien**  
Graduation with distinction, merit scholarships 2011, 2012, and 2013  
Bachelor thesis: *Ionization of hydrogen atoms by sculpted ultrashort laser pulses*
- 09/2009 – 08/2010 **Compulsory military service as a one-year volunteer (EF)**  
Branch: engineer  
Since then, advanced training during military exercises to become a company commander.
- 09/2001 – 06/2009 **High school, BG/BRG St. Veit/Glan, 9300 St. Veit/Glan**  
Emphasis on natural sciences  
“Matura” with distinction

---

## WORK EXPERIENCE

- since 03/2022 **Software engineer  
Siemens AG Österreich, 1210 Wien**  
Power grid optimization, load forecast, renewable energy sources forecast
- 01/2018 – 02/2022 **University assistant, Institute for Theoretical Physics (E136)  
Vienna University of Technology (TU Wien), 1040 Wien**  
Working group *Non-Hermitian physics and complex scattering*  
Lecturer in the exercise classes *Quantum Mechanics I & II*

- 11/2016 – 01/2018 **Project assistant, Institute for Theoretical Physics (E136)**  
**Vienna University of Technology (TU Wien), 1040 Wien**  
NextLite project *Nonlinear Phenomena in Complex Photonic Structures*
- 03/2015 – 07/2015 **Tutor, Institute of Solid State Physics (E138)**  
**Vienna University of Technology (TU Wien), 1040 Wien**  
Tutor in *Scientific computing* and *Numerical methods and simulation*

---

### AWARDS AND STIPENDS

- 2017 & 2019 **Christiana HÖRBIGER Prize**  
Prize for the funding of the international mobility of young scientists
- 2017 **Appreciation Award (Würdigungspreis) of the Austrian Federal Ministry of Science, Research and Economy**  
State award for the best diploma and master's degrees
- 2011 – 2014 **Merit scholarship of the TU Wien**  
Awarded for the years 2011, 2012, 2013, and 2014

---

### FIELDS OF RESEARCH

Quantum optics, non-Hermitian photonics, optomechanics, laser theory, exceptional points, complex wave scattering, coherent perfect absorption, etc.

---

### CONFERENCES, WORKSHOPS, AND SEMINARS

- Feb. 06, 2020 **Seminar** (invited talk)  
*Special Solid State & Optics Seminar* (Yale University), New Haven, CT, USA
- Nov. 25, 2019 **Seminar** (invited talk)  
*RIKEN Seminar*, Saitama, Japan
- Nov. 21, 2019 **Lecture series** (invited talk)  
*VHS Science Lecture*, Vienna, Austria
- Aug. 06 – 08, 2019 **Conference** (invited talk)  
*Foundations of Nonlinear Optics (FoNLO) 2019*, Dayton, OH, USA
- July 23 – 26, 2019 **Conference** (invited talk)  
*META 2019*, Lisbon, Portugal
- Jan. 08, 2019 **Seminar** (invited talk)  
*Vienna Theory Lunch Seminar*, Vienna, Austria
- June 23 – 24, 2016 **Workshop** (participation)  
*NextLite DoktorandInnen-Workshop*, Graz, Austria
- May 03 – 04, 2016 **Workshop** (contributed talk)  
*NextLite-Workshop*, Vienna, Austria
- Mar. 19, 2014 **Seminar** (contributed talk)  
*Seminar for theoretical physics* (TU Wien), Vienna, Austria

---

## PUBLICATIONS

- [1] M. Belitsch, D. N. Dirin, M. V. Kovalenko, K. Pichler, S. Rotter, A. Ghalgaoui, H. Ditlbacher, A. Hohenau, and J. R. Krenn. *Gain and lasing from CdSe/CdS nanoplatelet stripe waveguides*. *Micro and Nano Engineering* **17**, 100167 (2022). (Not covered in this thesis.)
- [2] Y. Slobodkin, G. Weinberg, H. Hörner, K. Pichler, S. Rotter, and O. Katz. *Massively degenerate coherent perfect absorber for arbitrary wavefronts*. *Science* **377**, 995 (2022). (Selected by Physics World as one of the top 10 Breakthroughs of the Year for 2022. Covered in Physics Today, APS Physics Magazine, New Scientist, Scientific American, etc.)
- [3] M. Horodyski, M. Kühmayer, A. Brandstötter, K. Pichler, Y. V. Fyodorov, U. Kuhl, and S. Rotter. *Optimal wave fields for micromanipulation in complex scattering environments*. *Nature Photonics* **14**, 149 (2020). (Not covered in this thesis.)
- [4] K. Pichler, M. Kühmayer, J. Böhm, A. Brandstötter, P. Ambichl, U. Kuhl, and S. Rotter. *Random anti-lasing through coherent perfect absorption in a disordered medium*. *Nature* **567**, 351 (2019).
- [5] J. Zhang, B. Peng, Ş. K. Özdemir, K. Pichler, D. O. Krimer, G. Zhao, F. Nori, Y.-x. Liu, S. Rotter, and L. Yang. *A phonon laser operating at an exceptional point*. *Nature Photonics* **12**, 479 (2018).